

# **Interferometry for a space-based gravitational wave observatory**

Reciprocity of an optical fiber

Von der Fakultät für Mathematik und Physik  
der Gottfried Wilhelm Leibniz Universität Hannover  
zur Erlangung des Grades

**Doktor der Naturwissenschaften**  
**Dr. rer. nat.**

genehmigte Dissertation

von  
Dipl. Phys. Roland Fleddermann

geboren am 17. März 1981 in Rahden  
(2012)

---

Referent: Karsten Danzmann  
Korreferent: Guido Mueller  
Tag der Promotion: 24. Januar 2012

“Equipped with his five senses, man explores the universe around him and calls the adventure Science.”

- Edwin Powell Hubble, [1]

“Wissenschaft wird von Menschen gemacht.”

- Werner Heisenberg, [2]

“We are stardust”

- Joni Mitchell





---

## Kurzzusammenfassung

---

Diese Arbeit untersucht single-mode, polarisationserhaltende Glasfasern hinsichtlich ihrer Eignung für zukünftige, satellitengestützte Gravitationswellenobservatorien. Hierbei besteht die Sorge, dass solche Fasern nicht-reziprokes Rauschen einfügen könnten.

Der für weltraumgestützte Gravitationswellendetektoren interessante Frequenzbereich liegt zwischen 0,1 mHz und 1 Hz. Das Ziel ist es, nicht-reziproke Weglängenunterschiede mit einem Rauschen von  $1 \text{ pm}/\sqrt{\text{Hz}}$  zu messen. Die besonderen Auslegungsbedingungen dieser Detektoren werden dabei berücksichtigt.

Zunächst werden mögliche nicht-reziproke Effekte diskutiert. Wo vorhanden, werden bereits veröffentlichte Daten verwendet, um die Größe des Einflusses dieser Effekte abzuschätzen. Der Faraday- und der Sagnac-Effekt werden zusammen mit der Dispersion des optischen Mediums behandelt, welche *augenscheinliche* nicht-reziproke Effekte hervorruft.

Darauf folgend wird ein Messaufbau vorgestellt, der geeignet ist, nicht-reziprokes Rauschen mit dieser anspruchsvollen Anforderung zu messen und der repräsentativ für eine geplante optische Bank für einen Gravitationswellendetektor ist. Der interferometrische Aufbau wurde mit Hilfe der Technik des *hydroxycatalysed bondings* hergestellt, welche zu einem quasi-monolithischen Aufbau mit hoher mechanischer Stabilität und geringem thermischen Ausdehnungskoeffizienten führt. Dieser Aufbau wird hinsichtlich seines nicht-reziproken Rauschens charakterisiert und mehrere Rauschreduzierungs- und Rauschsubtraktionstechniken werden vorgestellt, die zusammen die Messung von nicht-reziprokem Rauschen mit Pikometer Genauigkeit ermöglichen. Untersuchungen mit diesem Aufbau führten zur Bestätigung des nicht-reziproken Rauschens einer optischen Faser auf dem  $1 \text{ pm}/\sqrt{\text{Hz}}$  Niveau.

Reflektiertes Licht von der Faser wurde als eine der größten Quellen von Messungenauigkeiten identifiziert. Deswegen wurde ein gesonderter Messaufbau zur Identifikation der Quelle der Reflektion und ihrer Größe ausgearbeitet. Weiterhin wurde *digitally enhanced heterodyne interferometry* angewendet, um die Trennung von reflektiertem Signal und Mess-Signal zu ermöglichen.

Schließlich werden die Auswirkungen der in dieser Arbeit vorgestellten Ergebnisse auf den Entwurf einer optischen Bank für ein Gravitationswellenobservatorium vorgestellt. Verschiedene Alternativen werden vorgestellt und ihre Vor- und Nachteile werden erläutert.

---

**Schlagwörter: Reziprozität, Glasfasern, Gravitationswellen**

---

## Abstract

---

This work investigates the applicability of single-mode, polarization-maintaining fibers on board a future space-based gravitational wave observatory. The main concern here is that such fibers could potentially introduce non-reciprocal noise. The frequency range of interest for space-based gravitational wave detectors is 0.1 mHz to 1 Hz, and the aim is to measure non-reciprocal path length differences of  $1 \text{ pm}/\sqrt{\text{Hz}}$ . The special design constraints set by these detectors are also taken into account.

First, possible non-reciprocal effects are discussed. Published data on these effects is used to calculate estimates of their magnitude, where such data is available. The Faraday-effect and the Sagnac-effect are treated along with the dispersion of the optical medium, which introduces *apparent* non-reciprocal signals.

Following this, a measurement setup capable of measuring non-reciprocal noise at this challenging level and representative of a planned optical bench for a gravitational wave detector is presented. This interferometric setup was built using hydroxide-catalysis bonding, yielding a quasi-monolithic setup with high mechanical stability and low coefficient of thermal expansion. This setup is characterized in terms of its non-reciprocal noise and several noise reduction and subtraction techniques are introduced, which collectively enable the measurement of non-reciprocal noise at the pm level. Investigations using this setup led to the verification of non-reciprocal noise of an optical fiber at the  $1 \text{ pm}/\sqrt{\text{Hz}}$  level.

Reflected light from the fiber has been found to be the a major source of measurement error. Therefore, a special setup has been devised to measure the amplitude and identify the source of the reflection. Digitally enhanced heterodyne interferometry has also been implemented to enable the separation of the reflected signal and the measurement signal.

Finally, the implications of the findings presented in this work on the design of an optical bench for a gravitational wave observatory are discussed. Several design alternatives are presented along with their individual advantages and disadvantages.

**Keywords:** Reciprocity, optical fibers, gravitational waves



---

## Contents

---

<b>1. Introduction</b>	<b>1</b>
<b>2. Expected non-reciprocal effects</b>	<b>5</b>
2.1. Sagnac-effect . . . . .	5
2.2. Faraday effect . . . . .	7
2.3. Dispersion in fiber . . . . .	10
<b>3. Measurement of non-reciprocal noise</b>	<b>13</b>
3.1. Sagnac interferometric measurements . . . . .	13
3.2. Laser Interferometer Space Antenna (LISA)-like setup . . . . .	14
3.2.1. Aluminum base-plate . . . . .	18
3.2.2. Zerodur™ base-plate . . . . .	21
3.3. Phase measurement noise . . . . .	31
3.3.1. Software phase meter measurement noise . . . . .	33
3.3.2. FPGA based phase meter measurement noise . . . . .	34
3.3.3. Comparison of both phase meter options . . . . .	35
3.4. Differential photo diode noise . . . . .	35
3.4.1. Effect of removing photo diode windows . . . . .	38
3.4.2. Photo diode substrate material . . . . .	39
3.4.3. Vacuum feed-throughs . . . . .	40
3.4.4. Polarizers in front of photo diodes . . . . .	42
3.5. Reduction of external influences . . . . .	42
3.5.1. Fluctuations in the refractive index of air . . . . .	43
3.5.2. Optical path length difference OPD stabilization . . . . .	44
3.5.3. Laser intensity stabilization . . . . .	45
3.5.4. Amplitude stabilization at the heterodyne frequency . . . . .	47
3.5.5. Reduction of thermal fluctuations . . . . .	49
3.5.6. Vibration reduction . . . . .	51

3.5.7.	Laser frequency noise . . . . .	53
3.5.8.	Polarization control . . . . .	55
3.5.9.	Fiber length stabilization . . . . .	58
3.6.	Noise subtraction in data post-processing . . . . .	60
3.6.1.	Spurious beams from fiber couplers . . . . .	62
3.6.2.	Beam pointing fluctuations . . . . .	65
3.6.3.	Temperature noise subtraction . . . . .	73
3.7.	Results . . . . .	76
3.7.1.	Setup noise . . . . .	76
3.7.2.	Fiber non-reciprocity . . . . .	78
<b>4.</b>	<b>Direct reflection measurements</b>	<b>83</b>
4.1.	Initial setup . . . . .	84
4.2.	Improved setup . . . . .	86
4.3.	AR coated fibers . . . . .	86
4.4.	Identification of the origin of the reflection . . . . .	87
4.5.	Results . . . . .	88
4.6.	Conclusion . . . . .	88
<b>5.</b>	<b>Digitally enhanced heterodyne interferometry</b>	<b>91</b>
5.1.	Potential benefits of digital heterodyne interferometry . . . . .	91
5.2.	Required setup changes . . . . .	92
5.2.1.	Modulation bench for MHz range offset frequencies . . . . .	94
5.2.2.	Optical laser offset locking for MHz range beat notes . . . . .	95
5.2.3.	Phase measurement system . . . . .	96
5.3.	Characterization of the phase measurement system . . . . .	97
5.4.	First results . . . . .	99
5.5.	Noise hunting . . . . .	100
5.5.1.	Laser parameters . . . . .	101
5.5.2.	Differential photo diode noise . . . . .	102
5.5.3.	Beam centering considerations . . . . .	103
5.5.4.	Cladding modes and pointing stability . . . . .	105
5.6.	Conclusion . . . . .	106
<b>6.</b>	<b>Consequences for the design of the LISA optical bench</b>	<b>109</b>
6.1.	Attenuation of stray light . . . . .	109
6.2.	Balanced detection . . . . .	111
6.3.	Direct stray light subtraction . . . . .	112
6.4.	Measurement of the reflection signal . . . . .	114
6.5.	Digitally enhanced heterodyne interferometry . . . . .	114
6.6.	Discussion of the possible alternatives . . . . .	115
<b>7.</b>	<b>Other potential applications</b>	<b>117</b>
7.1.	Rotation calibration using the Sagnac-effect . . . . .	117

7.2. Heterodyne Sagnac interferometry . . . . .	119
<b>8. Conclusions</b>	<b>123</b>
<b>A. POV-Ray output extension for IFOCAD</b>	<b>125</b>
<b>B. Matlab code to calculate bending of a Zerodur™ base plate</b>	<b>133</b>
<b>C. Proper treatment of optical fibers</b>	<b>135</b>
C.1. Polarization issues . . . . .	135
C.2. Contamination and damage of the fiber interfaces . . . . .	137
<b>Bibliography</b>	<b>141</b>
<b>Publications</b>	<b>153</b>





---

## List of Figures

---

2.1. Comparison of Sagnac-effect induced noise and requirement . . . . .	7
2.2. Magnetic field noise induced polarization rotation . . . . .	9
3.1. Schematic of a Sagnac Interferometer . . . . .	14
3.2. Best results achieved using the Sagnac setup. . . . .	15
3.3. LISA Pathfinder style modulation bench . . . . .	16
3.4. Schematic of the non-reciprocity experiment . . . . .	16
3.5. Phase relations in REF, MEAS1 and MEAS2 interferometer. . . . .	17
3.6. Non-reciprocity interferometer on aluminum plate . . . . .	18
3.7. Schematic of setup on aluminum . . . . .	19
3.8. Illustration of the down-mixing scheme . . . . .	20
3.9. Comparison of fiber non-reciprocity and null measurement . . . . .	21
3.10. Drawing for the specification of mirrors for bonding. . . . .	22
3.11. Illustration of the angle introduced through bending of base plate .	23
3.12. Deformation analysis of a 10 mm Zerodur™ base plate . . . . .	24
3.13. Simulation of maximum deformation/angle of base plate . . . . .	25
3.14. Simulated bending of a 10 mm thickness Zerodur™ base plate . . .	26
3.15. Comparison between bending using finite elements and plate theory	27
3.16. POV-Ray rendering of Zerodur™ base plate with optics . . . . .	28
3.17. Actual Zerodur™ base plate . . . . .	28
3.18. Ghost beam analysis on Optocad model of the Zerodur™ optical bench . . . . .	30
3.19. OptoCad design of Zerodur™ base-plate interferometer layout . . .	31
3.20. CAD model of the alignment template . . . . .	32
3.21. Test setup for measuring phase measurement noise of the phase meter	33
3.22. Test of phase meter noise using electrical signals with added white noise. . . . .	34
3.23. Phase measurement noise using different input signal levels . . . . .	35

3.24. Phase measurement noise dependence on input signal level. . . . .	36
3.25. Direct comparison between differential noise observed using PM2 and PM3 . . . . .	36
3.26. Setup for the measurement of differential photo diode noise. . . . .	37
3.27. Initial differential photo diode and phase meter noise . . . . .	38
3.28. Photo diode windows and their influence on spurious signals. . . . .	39
3.29. Effect of removing windows on differential photo diode noise . . . . .	40
3.30. Differential photo diode noise using InGaAs and silicon photo diodes	41
3.31. Differential photo diode noise using vacuum feed-throughs . . . . .	41
3.32. Influence of polarization filters on differential photo diode noise . . .	43
3.33. Non-reciprocal noise observed with/without active optical path length difference (OPD) stabilization . . . . .	44
3.34. Full schematic of the actual modulation bench. . . . .	45
3.35. Non-reciprocity observed with/without active laser amplitude sta- bilization . . . . .	47
3.36. Measured closed loop transfer function of the amplitude stabilization circuit . . . . .	48
3.37. Placement of additional photo detectors for spurious signals . . . . .	49
3.38. Direct stray light subtraction by using an amplitude stabilization circuit . . . . .	50
3.39. Schematic of thermal shield . . . . .	51
3.40. Transfer function of the thermal shield . . . . .	52
3.41. Photo of passive, vacuum compatible vibration damper . . . . .	53
3.42. Laser frequency noise coupling factor (fiber length measurement) .	54
3.43. Laser frequency noise coupling factor (non-reciprocity) . . . . .	55
3.44. Photograph of photo diode mount with polarization filter . . . . .	56
3.45. Schematic of setup showing positions of all polarizers in use . . . . .	56
3.46. Schematic of single-mode, polarization-maintaining fiber . . . . .	57
3.47. Method to align input polarization to fiber axis . . . . .	58
3.48. Periodic error observed when scanning the length of the fiber under test using a piezo. . . . .	59
3.49. Coupling coefficients for periodic error observed when scanning the fiber length . . . . .	59
3.50. Fiber length noise with/without active length stabilization . . . . .	61
3.51. Non-reciprocal noise observed with/without fiber length stabilization	61
3.52. Illustration of the principle of stray light subtraction through bal- anced detection . . . . .	62
3.53. Non-reciprocal noise after application of balanced detection . . . . .	63
3.54. High pass and amplification electronics . . . . .	65
3.55. Measured and simulated transfer function of high pass . . . . .	66
3.56. Directly observed stray light and signal recovered from balanced detection . . . . .	66
3.57. OWIS TRANS 40-D25-MS mount . . . . .	68
3.58. differential wave front sensing (DWS) signal calibration . . . . .	69

3.59. Photo of picometer experiment with fiber couplers . . . . .	70
3.60. Fiber couplers in the non-reciprocity experiment . . . . .	70
3.61. Comparison of raw (unscaled) DWS signals . . . . .	71
3.62. Differential wave front signal subtraction . . . . .	72
3.63. Zerodur™ base plate temperature and non-reciprocal phase . . . . .	73
3.64. Temperature coefficient of non-reciprocity . . . . .	74
3.65. Photo of vacuum chamber with external thermal shield . . . . .	75
3.66. Temperature noise base plate with/without additional shield . . . . .	75
3.67. Comparison of setup noise observed after subtracting stray light and differential wave front sensing (DWS) noise and after additionally subtracting temperature noise. . . . .	77
3.68. Setup noise with all corrections applied . . . . .	78
3.69. Photograph of the fiber under test wound onto a ring made from piezo-electric ceramic, as used in the experiment. . . . .	79
3.70. Observed non-reciprocity . . . . .	80
4.1. Modification of non-reciprocity experiment for measurement of re- flections . . . . .	84
4.2. Schematic of the first direct reflection setup . . . . .	85
4.3. Direct stray light measurement setup in use with FIOS . . . . .	86
4.4. Schematic of the improved reflection measurement setup . . . . .	87
4.5. Reflections from different parts of the fiber under test . . . . .	88
5.1. Current design of the LISA optical bench . . . . .	93
5.2. Schematic of the modulation bench with offset locking . . . . .	96
5.3. Phase meter noise for different configurations of phase meter . . . . .	98
5.4. Electrical noise of the phase meter . . . . .	99
5.5. Non-reciprocity with DI . . . . .	100
5.6. Setup for identification of mode-hop free regions of the Innolight Mephisto laser . . . . .	101
5.7. Mode-hop free regions of the Innolight Mephisto laser . . . . .	102
5.8. First measurement of the differential phase noise of two photo de- tectors sensing an identical signal. . . . .	103
5.9. Simulation of beam diameters behind lenses of different focal length. . . . .	105
5.10. Differential photo diode noise before/after removal of cladding modes . . . . .	106
5.11. Non-reciprocal noise observed using the digitally enhanced interfer- ometry . . . . .	108
6.1. Use of an attenuator to reduce spurious reflected beat notes . . . . .	110
6.2. Impossibility of spurious signal reduction by attenuators in LISA . . . . .	111
6.3. Current design of LISA optical bench . . . . .	113
7.1. Mechanism used to rotate the fiber back and forth. . . . .	118
7.2. Sagnac phase shift versus rotation frequency of the fiber . . . . .	119
7.3. Non-reciprocal signal during back and forth rotation of fiber . . . . .	120

7.4. Projected rotation rate noise floor (75 m <sup>2</sup> area) . . . . .	121
A.1. IFOPov rendering of <i>polifo</i> interferometer . . . . .	131
A.2. Photograph of <i>polifo</i> interferometer . . . . .	131
C.1. Polarization measurements of optical fibers. . . . .	136
C.2. Magnified view of a fiber interface . . . . .	137
C.3. Magnified view of a damaged fiber interface. . . . .	139

---

List of Tables

---

4.1. Reflectivities of selected fibers. . . . . 89



---

## List of Abbreviations

---

<b>ADC</b>	analog-to-digital converter
<b>AEI</b>	Albert-Einstein-Institute
<b>ANU</b>	Australian National University
<b>AOM</b>	acousto-optic modulator
<b>AR</b>	anti-reflective
<b>COTS</b>	commercial off-the-shelf
<b>CTE</b>	coefficient of thermal expansion
<b>DC</b>	direct current
<b>DFT</b>	discrete Fourier transform
<b>DWS</b>	differential wave front sensing
<b>DI</b>	Digitally enhanced Interferometry
<b>EBB</b>	elegant breadboard
<b>EOM</b>	electro-optical phase modulator
<b>ESA</b>	European Space Agency
<b>FIOS</b>	fiber injector optical sub-assembly
<b>FPGA</b>	field-programmable gate array
<b>IIR</b>	infinite impulse response

<b>InGaAs</b>	indium gallium arsenide
<b>LISA</b>	Laser Interferometer Space Antenna
<b>LTP</b>	LISA Technology Package
<b>OPD</b>	optical path length difference
<b>PAAM</b>	point-ahead angle mechanism
<b>PANDA</b>	polarization-maintaining and absorption-reducing
<b>PC</b>	personal computer
<b>PD</b>	photo detector
<b>PER</b>	polarization extinction ratio
<b>PLL</b>	phase-locked loop
<b>PM</b>	phase meter
<b>ppm</b>	parts per million
<b>PRN</b>	pseudorandom noise
<b>RF</b>	radio frequency
<b>SBDFT</b>	single-bin discrete Fourier-transform
<b>UGL</b>	University of Glasgow



## CHAPTER 1

## Introduction

The main question to be answered in this thesis is whether optical path lengths in an optical fiber are reciprocal to such a precision that the requirements on these fibers for the use in space based gravitational wave detectors can be fulfilled.

To answer this question, one first needs to know what “reciprocal” means. In this case, we want to know if it takes exactly the same amount of time for light to travel through an optical fiber in one direction as it takes to the opposite direction.

This is a very basic question on the nature of light and the medium it passes through, and of course people have pondered it before. Strictly speaking, in the case of light traveling through vacuum one can use Maxwell’s equations and deduce that they remain unchanged under the reversal of time, thus allowing for the exact same solutions (c.f. [3]). However, this work is not concerned with light traveling through vacuum exclusively, but with the situation when light travels through a medium, in this case fused silica, of which modern optical fibers are made. Inside optical media, non-reversible processes are possible, especially when light is scattered or absorbed.

This work aims to verify the applicability of optical fibers in space based gravitational wave detectors like e.g. the Laser interferometer Space Antenna (LISA,[4]) mission or one of its currently discussed modifications (e.g. NGO,[5]).

These missions rely on the availability of optical fibers with a non-reciprocal noise contribution of less than 1 picometer/ $\sqrt{\text{Hz}}$  in the frequency range used in their observations, namely between 0.1 mHz and 1 Hz, (relaxing as  $1/f^2$  below 2.8 mHz), in order to be able to reach their design path length measurement sensitivities.

Gravitational wave detection missions use heliocentric orbits to reduce the influence of residual accelerations from other solar system bodies on the test masses on board their satellites. Fibers are foreseen in the current LISA baseline design, since a flexible optical connection within the interferometric path is desired. The angle

between the satellites deviates periodically during one year from its nominal value of  $60^\circ$  by up to  $1.5^\circ$  while the constellation moves around the Sun [6, 7]. Therefore, the direction of the light beams sent out from the spacecraft has to be changed. This is to be accomplished by changing the angle between two individual optical benches inside each satellite.

An optical link between these two optical benches is required to offset lock the lasers on each optical bench. Optical paths between the two optical benches on one satellite are traversed in opposite directions at the same time, and the relative phases of the transmitted light are measured at both ends. These two measurements allow the identification of two unknown variables: the two lasers' frequency difference and the delay introduced by the fiber. If the delay introduced by the fiber differs between opposite directions, then this would require an independent third measurement of fiber length in each direction, which is not possible as there is no second path available between the two optical benches which does not involve the fiber. It is therefore required that these non-reciprocal length changes be low enough to not interfere with the very sensitive interferometric length measurements.

The intended laser light source for these missions is a Nd-YAG laser operating at a wavelength of 1064 nm with a high coherence length and low spectral bandwidth to enable interferometric length measurements. Measurements of the reciprocity of the optical fiber will therefore have to be conducted using a comparable light source at the same wavelength in order to be applicable. The optical fiber to be tested must also be single-mode to ensure high spatial optical quality of the emerging beams as well as polarization-maintaining to enable heterodyne interferometry without loss of contrast due to changes in polarization state of the interfering beams.

In the past, people have been concerned with the measurement of non-reciprocal noise of fibers in the context of rotation sensing applications. Here, the *Sagnac-effect* is used to measure rotation, for example in navigation, replacing complicated mechanical gyroscopes by robust optical fibers with no moving parts [8].

Many measurements of the non-reciprocal noise of optical fibers have been made in this context, but often they either do not cover the frequency range of interest in this work (applications in navigation are typically concerned with even lower frequencies) or, results are not given in terms of spectral densities but in terms of peak to peak noise using a specific integration time, which can not be converted into spectral densities because the information on the spectral distribution of noise is lost in the averaging process. One such example can be found in [9]. Ultimately, these measurements are also not applicable to the question of fiber non-reciprocity in the context of space-based gravitational wave detection, because they were made using different laser wavelengths and/or using techniques that are not applicable in the context of this work, such as using low coherence length light sources to avoid stray light problems [10].

The thesis is organized as follows: possible sources of non-reciprocal noise and their potential influence on the measurement are discussed in the next chapter. This is followed by a chapter presenting the measurement setup used in the course of this work and the resulting non-reciprocal noise levels observed using this setup.

Chapter 4 deals with the direct measurement of reflected light from fibers. During the measurements of the fiber non-reciprocity, reflections turned out to be the limiting noise source, which made a detailed investigation of their origin seem worthwhile. A highly sensitive setup optimized for the measurement of reflected light harmful in these measurements is presented, along with results of observed levels of reflected light using available optical fibers.

The subsequent Chapter 5 is concerned with a special technique called Digitally enhanced Interferometry (DI), which can be used to reduce the impact of stray light and ghost beams on interferometric measurements. A modified setup to incorporate this technique was designed and implemented. Results obtained using this setup and noise investigations are also addressed.

The potential impact on the design of an optical bench for a gravitational wave detection mission in space is discussed in Chapter 6. Several approaches for the mitigation of noise sources are presented and their respective advantages and disadvantages are discussed.

This is followed by a chapter dealing with other potential applications of the techniques presented in this thesis. A calibration measurement performed on the non-reciprocal noise measurement setup is presented and the potential application of the setup in rotation sensing is discussed.

Finally, Chapter 8 wraps up the results and findings presented in this thesis.



---

## Expected non-reciprocal effects

---

This chapter deals with some well-known non-reciprocal effects and their potential influence on the outcome of measurements of the non-reciprocity of optical fibers. Among these are the Sagnac-effect, detailed in Section 2.1 and the Faraday effect, which is discussed in Section 2.2.

Furthermore, there are effects which are not genuinely non-reciprocal in nature but which still influence the measurement in a way that phases are changed in a non-reciprocal way (i.e. phases on both ends of the link are changed independently). This can happen if dispersion is present in the fiber, as is explained and discussed in Section 2.3.

In order to be able to assess the possible influence of these effects, some effort has been made to make estimates, as is detailed in the following sections.

### 2.1. Sagnac-effect

The *Sagnac-effect* was discovered in 1913 by the French scientist Georges Sagnac [11, 12]. It occurs in a special type of interferometer, nowadays named after its inventor, the Sagnac interferometer. In such an interferometer, light is split by a beam splitter into two beams traveling in opposite directions through identical paths, before recombining at the same beam splitter. Sagnac made the observation that while normally all light is expected to be directed back toward the light source in a perfectly reciprocal setup, a non-reciprocal phase shift did occur when the whole setup was put on a rotating platform, changing the interference of the two beams.

He found that the magnitude of the observed phase shift is proportional to the angular velocity of the rotation, as well as the area that is enclosed by the light

beams. The exact equation for the non-reciprocal phase shift due to Earth's rotation,  $\Delta_{\text{Sagnac},\oplus}$ , is [13] :

$$\Delta_{\text{Sagnac},\oplus} = \frac{8\pi A \Omega_{\oplus} \cos \theta}{\lambda_0 c}$$

Here,  $A$  is the area enclosed by the light path,  $\Omega_{\oplus}$  denotes Earth's angular rotation rate and  $\theta$  is the angle enclosed by the rotation vector and the surface normal vector of the area enclosed by the fiber. Finally,  $\lambda_0$  is the vacuum wavelength of the light used in the experiment.

This effect leads to a genuinely non-reciprocal phase shift, which is of course also measured in the non-reciprocity experiment. Therefore, it can be considered a noise source in case a rotation of changing angular velocity is present. The most obvious source of rotation is the Earth's rotation. Depending on the latitude where the experiment is performed, the phase shift due to the Earth's rotation can be calculated.

Using the area covered by this experiment ( $\approx 0.126 \text{ m}^2$ ), the latitude of our laboratory in the Albert-Einstein-Institute (AEI) Hanover of 52.39 degree north and Earth's rotation rate of  $2\pi \text{ rad} / (24 \text{ h} \times 60 \text{ min} / \text{h} \times 60 \text{ s} / \text{min}) \approx 73 \text{ } \mu\text{rad} / \text{s}$ , this results in a static phase shift of  $0.57 \text{ } \mu\text{rad}$  which is small compared to the envisaged noise level of  $\approx 6 \times 10^{-6} \text{ radians} / \sqrt{\text{Hz}}$ .

Furthermore, only variations of this phase shift in the frequency range between 0.1 mHz and 1 Hz are of interest for the noise performance of the experiment. As Earth's rotation rate is fairly stable (it has, in fact, been used as a clock reference for a long time and sometimes is still today [14]), it is safe to assume that the noise of this phase shift,  $\tilde{\Delta}_{\text{Sagnac},\oplus}$  is much smaller than the actual phase shift  $\Delta_{\text{Sagnac},\oplus}$ . Measurements taken using a ring-laser, using the Sagnac-effect specifically for the purpose of monitoring the changes in Earth's rotation rate, have shown that its relative changes are typically below one part per million [15].

Figure 2.1 shows data taken from [15], converted to a noise spectral density. Due to the low sampling rate employed in the experiments described in [15] – one measurement every 30 minutes  $\approx 0.56 \text{ mHz}$  – the spectrum of the Sagnac-effect induced non-reciprocal length changes only extends up to about 0.25 mHz. Still, the graph clearly illustrates that the Sagnac-effect induced errors are far below the 1 pm requirement.<sup>1</sup>

---

<sup>1</sup>A quick “back of the envelope” calculation reveals that the energy necessary for even a  $10^{-3}$  relative change in Earth's rotation rate on timescales of less than 30 s by far exceeds the energy a meteor strike with exact opposite spin with respect to the Earth would release. In such a situation we would probably have other things to worry about than non-reciprocal noise in a fiber...

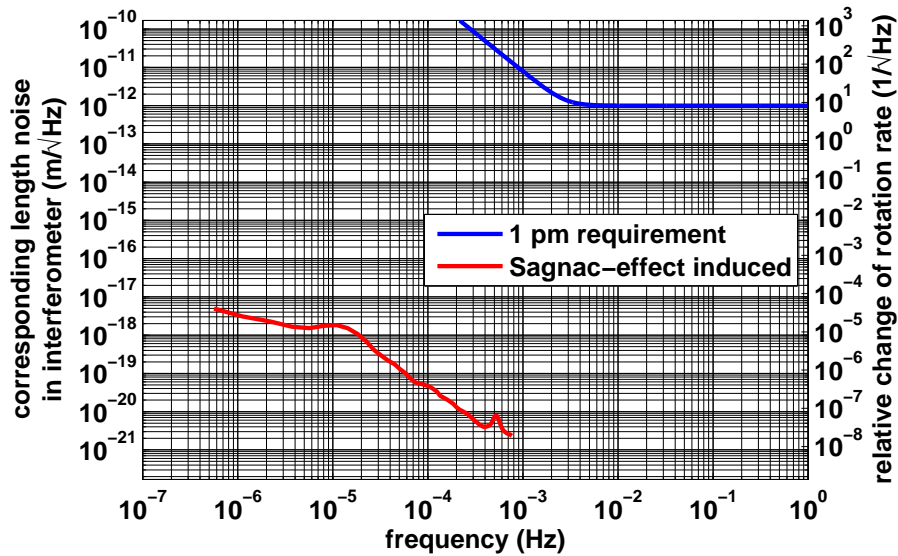


Figure 2.1.: Comparison of Sagnac-effect induced non-reciprocal length changes and the 1 pm requirement. Data from [15] was used and converted to a spectral density.

## 2.2. Faraday effect

It is widely known that the Faraday effect in optical fibers rotates the polarization, which can be used in sensing applications [16, 17]. In our case, the polarization state of light should be constant to ensure optimum contrast in the interferometers and to suppress unwanted beat signals.

To calculate the effect of magnetic field variations on the polarization state of the light the *Verdet constant* of fused-silica is required. The Verdet constant is the constant of proportionality between the magnetic field and the degree of polarization rotation per unit length of medium passed.

The Verdet constant  $V$  of a fused silica ( $\text{SiO}_2$ ) fiber is wavelength dependent. However, it was found that it is proportional to the inverse of the light field's oscillation frequency squared,  $1/\nu^2$ . With this in mind, an *effective* Verdet constant can be defined. The effective Verdet constant of single-mode polarization-maintaining fused silica fibers was found to be  $2.0 \times 10^{-35} \text{ rad} \times \text{s}^2 / \text{A}$  [18]. At a wavelength of  $1.064 \mu\text{m}$  this computes to a Verdet constant of about 1.59 microradians per ampere. Using a fiber of length  $d=7 \text{ m}$ , as in the experiments described here, and a typical value for the magnetic field of the Earth of  $70 \mu\text{T}$  (the average value observed in the measurements described below) and the magnetic constant  $\mu_0$  the rotation of the polarization angle can be computed as follows [19]:

$$\beta = V \cdot d \cdot B / \mu_0 \quad (2.1)$$

$$= 1.59 \cdot 10^{-6} \left[ \frac{\text{rad}}{\text{A}} \right] \cdot 7 \text{ m} \cdot 70 \cdot 10^{-6} \text{ T} \cdot \frac{1}{4\pi \cdot 10^{-7}} \frac{\text{A}}{\text{Tm}} \quad (2.2)$$

$$= 0.7 \text{ mrad} = 0.04^\circ \quad (2.3)$$

The magnetic field  $B$  affecting the fiber should be as constant as possible to avoid a change in the polarization state. In our laboratory the Earth's magnetic field is the main varying magnetic source. Since no source of magnetic field variation spectral density data was found, measurements were made using the integrated sensors of a conventional smartphone. Data was taken using a special "app" ("Data recording", available in the Android market). It was then loaded into the computer and a spectral density was computed using MATLAB©. Two different devices using different magnetic field sensors were used to allow comparison of the results.

The results are presented in Figure 2.2. The spectrum represented by the red, solid trace stemming from a measurement performed using the AK8973 sensor [20] integrated into the Sony Ericsson X10 mini pro is flat for frequencies between about 1 mHz and 0.1 Hz. At higher frequencies a low pass filter behavior is observed, most likely due to an integrated anti-aliasing filter in the device. Towards very low frequencies (i.e. below 1 mHz) a roughly  $1/f$  increase in magnetic field noise and corresponding polarization rotation noise is observed. The level of magnetic field noise is at about  $1 \mu\text{T}/\sqrt{\text{Hz}}$  in the mid-frequency range, leading to a polarization rotation noise of about  $10 \mu\text{rad}/\sqrt{\text{Hz}}$ .

The blue, dashed trace, representing a measurement performed the MPU3050 sensor integrated into the Acer Iconia Tab (data kindly provided by Christian Diekmann) has a similar shape, but the overall noise is about a factor of two below the red trace. Data could also be read at a higher rate with this sensor, therefore the spectrum extends to higher frequencies and low pass behavior is only observed for frequencies above 20 Hz. In the frequency range between 1 Hz and 20 Hz noise levels drop from approximately  $1 \mu\text{T}/\sqrt{\text{Hz}}$  to  $0.2 \mu\text{T}/\sqrt{\text{Hz}}$ .

The corresponding level of polarization rotation is far lower than the observed change in polarization state due to thermal effects in the fiber and can thus be neglected safely. Furthermore, it is very likely that the measured magnetic field fluctuations are sensor limited. The flat noise shape in the mid frequency range seems to suggest this, and also the fact that no variation was observed between measurements taken at different places. The magnetic field sensors in smartphones are usually low cost devices and their sensitivity is designed to be sufficient for navigational purposes, i.e. to locate the magnetic north pole, with little or no emphasis on noise reduction measures. Therefore, it is likely that the actual Faraday-effect induced polarization rotation noise is even lower than that indicated in Figure 2.2. Due to the fact that this level is already far too low to be observed in the experiment, no further action was taken to reduce the sensor noise of the magnetic



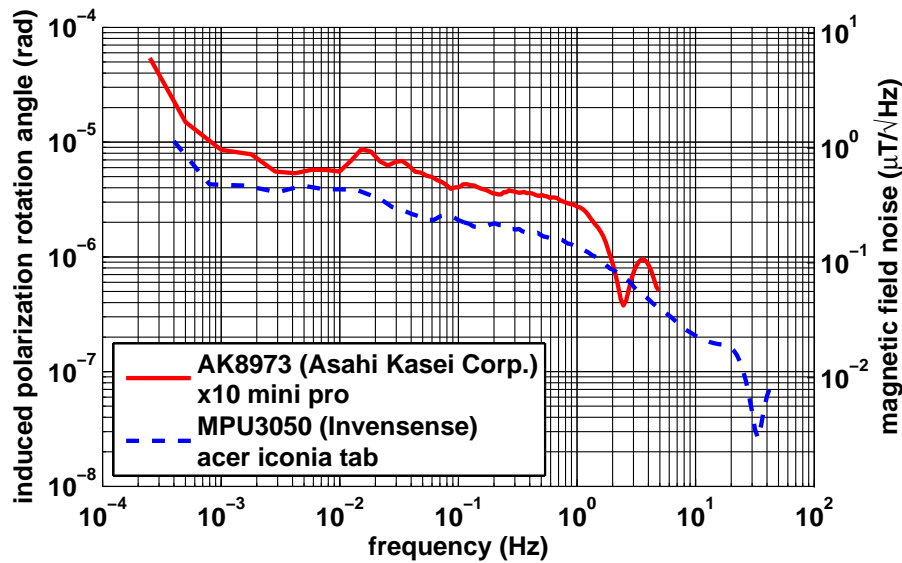


Figure 2.2.: Magnetic field noise induced polarization rotation in a single-mode, polarization-maintaining fiber.

field sensor. There is, however, indication that the actual magnetic field fluctuation may be up to three orders of magnitude lower [21].

The Verdet constant is also temperature dependent, which leads to another source of polarization noise. However, the temperature coefficient of the Verdet constant is  $(0.7 \cdot 10^{-4}/\text{K})$  [22], which means that changes in the Verdet constant due to temperature and the resulting polarization changes are about 4 orders of magnitude smaller, assuming even a relatively large temperature fluctuation of 1 K.

Not only are the effects of polarization rotation minute, but great care was also taken to minimize the influence of polarization state fluctuation on the experiment. Such changes in polarization state can occur in fibers due to imperfect matching of their polarization axis to the incoming polarization and resulting temperature dependence of the output polarization. Polarization filters were introduced at appropriate places in the experiment to mitigate these effects, as described in detail in Section 3.5.8.

In conclusion, it was found that genuine non-reciprocal effects due to the Faraday-effect in the fiber and changes in Earth's magnetic field amplitude are minute and can generally be neglected at the noise levels required in the experiment and with the unavoidable imperfection of optical fibers. Still, provisions have been made to deal with polarization fluctuations, mostly to reduce polarization fluctuation due to imperfect coupling to the fibers. These polarization filters will also further reduce the influence of the Faraday effect.

The Faraday effect will have an even smaller influence on the non-reciprocal noise of the setup itself (i.e. excluding the fiber, to characterize the achievable noise levels), as here the distances of light traveling through a medium are limited to

the beam splitters. They also consist of fused silica, but their thickness is typically only a few millimeters, adding up to maybe a few centimeters after several beam splitters, so the dispersion induced non-reciprocal noise is reduced by another two to three orders of magnitude compared to the 7 meters of fiber.

### 2.3. Dispersion in fiber

The effect that in a medium the index of refraction depends on the wavelength is called dispersion. This effect occurs in all transparent optical media at different magnitudes. Dispersion in itself is not non-reciprocal, but it can lead to non-reciprocal effects if the two counter-propagating beams in the medium do not have the same wavelength, as is the case in the LISA mission, where they will be separated by up to 20 MHz.

In this case, the phase shift in the two counter-propagating beams will be different, due to the different index of refraction  $n$ . This is in itself still not causing non-reciprocal noise, as it would simply imply a static offset in the measurement of the non-reciprocal phase. However, if either the frequency difference between the two counter-propagating beams changes or the center laser wavelength changes, this can lead to different optical path length in the opposite directions.

A change in the frequency difference of the two counter-propagating beams would lead to apparent non-reciprocal length noise if the index of refraction is not constant for all wavelengths, i.e. if its first derivative is non-zero. However, the frequency difference between the two counter propagating beams is held constant by the use of offset-locking, hence this is of no concern.

However, the center laser wavelength changes due to its inherent frequency noise. Now, if the second derivative of the refractive index with respect to the wavelength does not vanish, then the corresponding *change* in refractive index (and thus in optical path length) experienced by the two counter propagating beams will be different and thus non-reciprocal phase noise will be observed.

The dispersion  $D$  in optical fibers is about 20 ps/(nm km) [23]. These quite unusual units stem from the fact that a great interest has been taken in the dispersion of fibers due to its effect on signals transmitted through them in telecommunication applications. Here, fibers are typically many kilometers long and spectral line widths of the signals transmitted through them are in the nanometer range. The dispersion is defined as

$$D = \frac{\lambda}{c} \frac{d^2 n}{d\lambda^2}.$$

Here,  $\lambda$  denotes the laser wavelength,  $n$  is the refractive index of the material and  $c$  is the speed of light.

The value of  $\frac{d^2 n}{d\lambda^2}$  can easily be computed from this relation for the wavelength used in LISA, namely 1064 nm. Furthermore, the frequency separation of the two counter propagating frequencies in the fiber is at most 20 MHz corresponding to

a difference in wavelength of about 75 fm at 1064 nm. Multiplying the second derivative of  $n$  with this number gives the difference in change of refractive index per wavelength for two close wavelengths.

If now the frequency of the laser changes by the amount specified in [24, <R010-050>], i.e. about 400 Hz (corresponding to a change of laser wavelength of about 2 attometer), then this leads to a change in the difference of refractive indices of the two counter propagating waves of  $2 \cdot 10^{-22}$ . This small change in refractive indices results in a non-reciprocal length change of about  $9.5 \cdot 10^{-22}$  m for even 10 m length of fiber. So, although in principle the dispersion in the fiber ultimately limits the reciprocity, this limit is far below the requirements for LISA and will not cause noise above the picometer/ $\sqrt{\text{Hz}}$  level.

Of course, one can also turn the question around and ask which maximum frequency noise would be allowed in order to assure that the dispersion induced non-reciprocity be below a certain level. For a non-reciprocal noise level of  $10^{-14}$  m (i.e. 2 orders of magnitude below the 1 pm requirement) this calculation yields a maximum allowed frequency deviation of 300 MHz, a value which is even far above the frequency noise of a not frequency stabilized Nd:YAG-laser, not to mention a pre-stabilized laser which is to be used in LISA. The dispersion induced non-reciprocal path length noise will be even smaller when looking at the non-reciprocal noise of the setup itself, as the distances of light traveling through a medium are limited to the beam splitters, leading to the same reduction of induced noise of two to three orders of magnitude as discussed in the previous section.



---

## Measurement of non-reciprocal noise

---

This chapter describes the measurement principle used to measure the non-reciprocal noise of the fiber under test. Two different principles are discussed, a measurement using the Sagnac-effect as described in Section 3.1 and a different principle where the relevant part of the currently foreseen LISA optical bench is replicated, described thereafter in Section 3.2.

The remaining sections of this chapter deal with the refinement and noise hunting of the experiments using the LISA-like setup. First, the phase measurement noise is evaluated, as described in Section 3.3. The subsequent section deals with the noise that is added to the measurement process by the photo detectors and their electronics. This is followed by Section 3.5, in which the influence of external disturbances on the measurement is discussed in detail. Section 3.6 deals with the subtraction of the remaining noise in data post processing, while the final section of this chapter, Section 3.7 contains the results on the non-reciprocal noise of the fiber under test as well as the measurement noise of the setup.

### 3.1. Sagnac interferometric measurements

Two alternative optical setups have been evaluated for the measurement of the non-reciprocal phase noise.

The first alternative uses a Sagnac interferometer. A Sagnac interferometer is, to first order, exclusively sensitive to non-reciprocal phase changes [25, 26]. This setup has the advantage of being relatively simple as can be seen from the schematic shown in Figure 3.1. A minimal setup consists of only a light source, a phase modulator, a beam splitter, a photo diode and the fiber under test. Furthermore, due to the reciprocity of the setup, coupling of path length fluctuations and laser frequency noise to the phase are largely eliminated. The main disadvantage of

the setup is that a heterodyne phase readout is not possible and hence additional components are needed to improve the sensitivity.

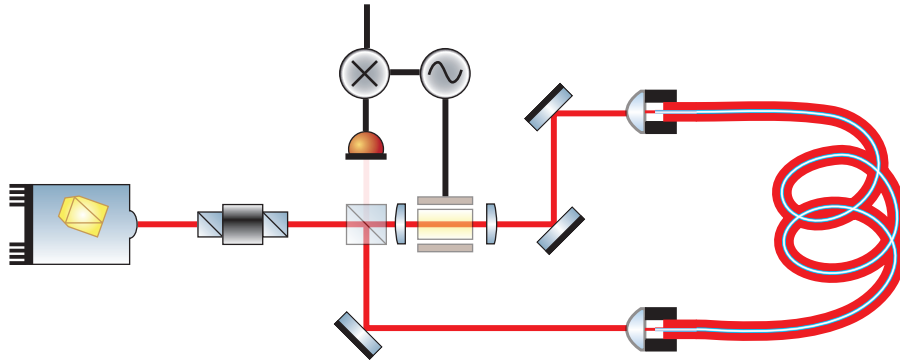


Figure 3.1.: Schematic of a possible setup for the measurement of the non-reciprocal noise of a fiber: A Sagnac interferometer.

Unfortunately it turned out that the sensitivity of this setup was limited to about  $0.5 \text{ nm}/\sqrt{\text{Hz}}$  to  $1 \text{ nm}/\sqrt{\text{Hz}}$  in the frequency range between 1 mHz and 100 mHz (c.f. Figure 3.2, which shows these results in comparison to the  $1 \text{ pm}/\sqrt{\text{Hz}}$  requirement) and that this noise level could not be improved although much noise hunting was undertaken [27]. Hence, the Sagnac setup is not described here further and the following discussions focus on the LISA-like setup.

## 3.2. LISA-like setup

The second alternative for the measurement of non-reciprocal noise in a fiber is a setup resembling the situation on-board a LISA spacecraft. This setup was used for the experiments described in this work. The advantage is that the interferometer layout offers the opportunity to characterize not only the fiber, but also other important aspects that are due to the LISA OB interferometer design. One of these aspects is e.g. that a heterodyne measurement can be performed. As a result the disadvantages are on the one hand that the setup is much more complex than a simple Sagnac setup and on the other hand that path length and laser frequency changes couple into the observed non-reciprocal length.

The LISA-like setup is shown in Figures 3.3 and 3.4. The heterodyne measurement scheme, based on the modulation bench of LISA Pathfinder [28, 29], is detailed

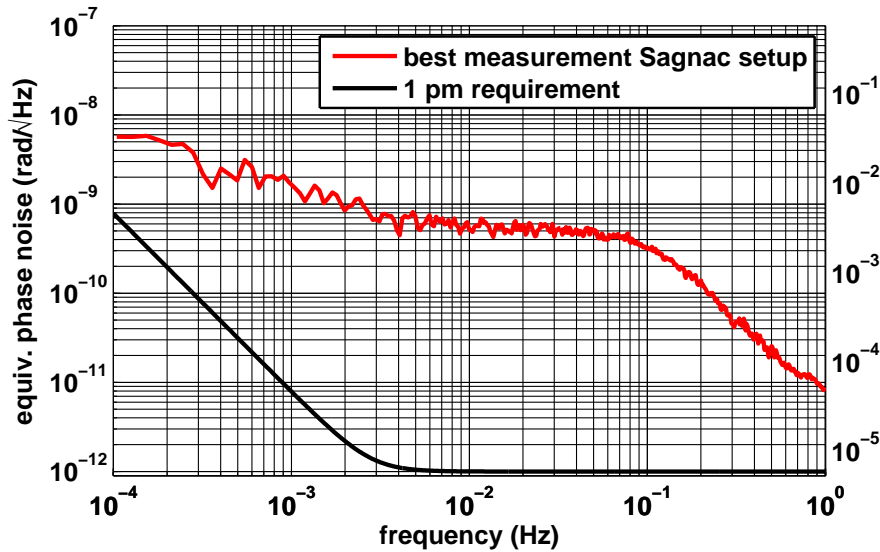


Figure 3.2.: Best results achieved using the Sagnac setup.

in Figure 3.3. Here, the light of one Nd:YAG laser is split into two beams by a power beam splitter. Both fractions are then sent through acousto-optic modulators (AOMs) working at slightly different frequencies, namely  $80 \text{ MHz} + 811.69 \text{ Hz}$  and  $80 \text{ MHz} - 811.69 \text{ Hz}$ , resulting in a frequency difference between the two output beams of  $1.623 \text{ kHz}$ . These beams are launched into the optical bench containing the interferometers, which are used in a heterodyne scheme [30].

The optical bench itself is shown in Figure 3.4. It consists of three individual interferometers which are used in combination to measure the non-reciprocal phase changes in the fiber under test.

In the reference interferometer (REF), illustrated in Figure 3.5a, both beams are directly routed to the interference beam splitter without passing through the fiber. The measured phase of this interferometer is used for subtraction of the path length changes on the modulation bench which are common-mode in all interferometers. In the first measurement interferometer (MEAS1) the first beam travels directly to the interference beam splitter, while the second beam passes through the fiber on its way to this point. The situation in the second measurement interferometer (MEAS2) is exactly the opposite. Here, the second beam travels directly to the beam splitter, while the first beam passes through the fiber.

Thus the reciprocal phase changes are measured in the two measurement interferometers (MEAS1 and MEAS2) in opposite directions. The non-reciprocity can now be found by adding the phase changes measured in both interferometers.

The phase  $\varphi_1$  in interferometer MEAS1 is given by  $\varphi_A + \varphi_{\uparrow} - \varphi_B$  and in interferometer MEAS2  $\varphi_2$  is given by  $\varphi_A - \varphi_B - \varphi_{\downarrow}$ . Here,  $\varphi_{\uparrow}$  and  $\varphi_{\downarrow}$  denote the phase shift from traveling through the fiber from bottom to top and from top to bottom, respectively,  $\varphi_A$  represents the phase accumulated along the path from

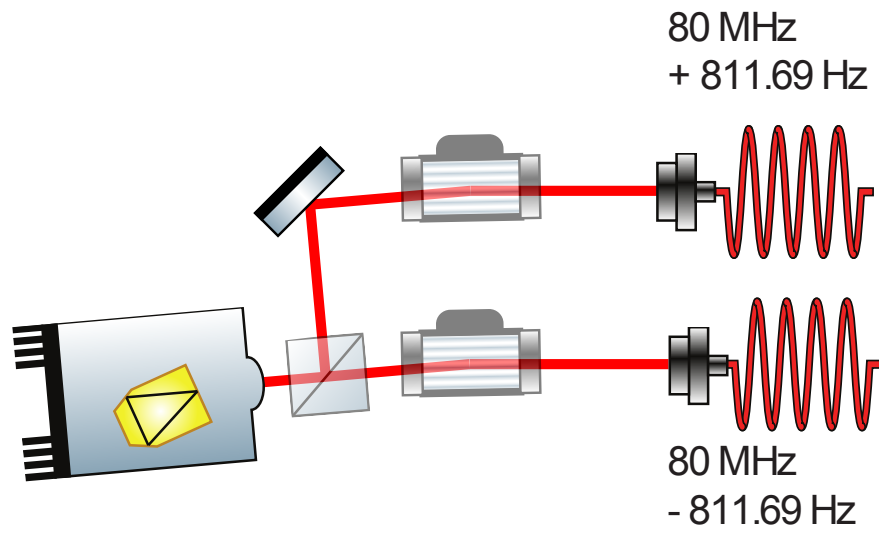


Figure 3.3.: LISA Pathfinder style modulation bench used in the experiments.

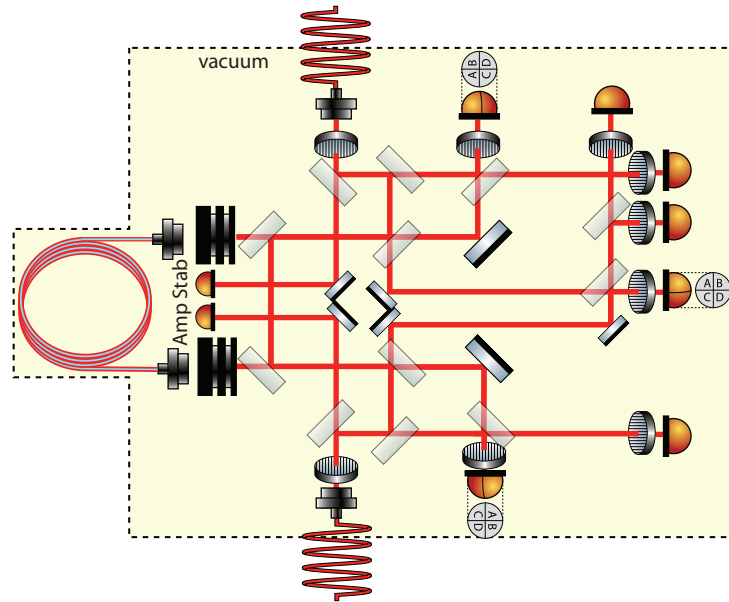
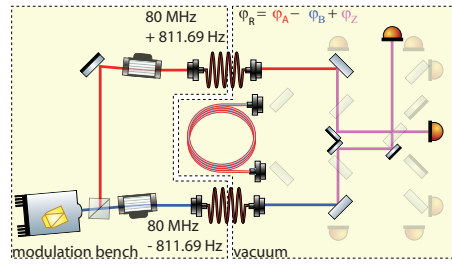
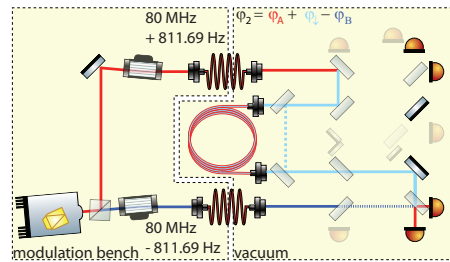
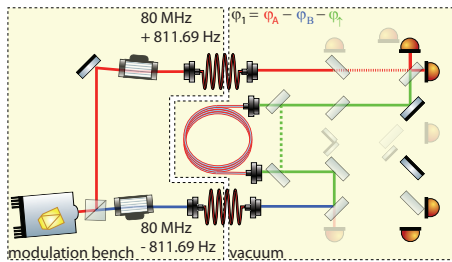


Figure 3.4.: Schematic of the non-reciprocity experiment





(a) Reference interferometer (REF)



(b) Measurement interferometer 1 (MEAS1) (c) Measurement interferometer 2 (MEAS2)

Figure 3.5.: Phase relations in REF, MEAS1 and MEAS2 interferometer.

the first beam splitter on the modulation bench to the first beam splitter on the non-reciprocity experiment through the upper fiber, and  $\varphi_B$  stands for the phase accumulated between the first beam splitter on the modulation bench and the first beam splitter on the non-reciprocity experiment through the lower fiber (c.f. Figure 3.5b and 3.5c). Adding these two relations and subtracting the twice reference phase,  $\varphi_r$  yields:

$$\varphi_1 + \varphi_2 - 2\varphi_r = \varphi_\uparrow - \varphi_\downarrow + 2\varphi_z \equiv \text{non-reciprocal phase } \Delta + 2\varphi_z$$

Here,  $\varphi_z$  denotes the phase change from the remaining paths on the optical bench that are not followed by the two beams in the same way. As these paths on the Zerodur™ optical bench are very stable, so is  $\varphi_z$  and thus the sum in equation 3.2 contains mainly the non-reciprocal path length noise.

Photo diodes at the corresponding beam splitters sense the beat signals at the heterodyne frequency of 1.623 kHz. Their phases are measured either with a software phase meter implemented on a personal computer (PC) like the one described in [31, 32] or a hardware phase meter, implemented using field-programmable gate arrays (FPGAs) [33].

It is also possible to measure the non-reciprocal noise of the setup itself, without using a fiber under test. This is accomplished by the two extra beam splitters in front of the interface to the fiber under test. One can either block the path between them on the optical bench and measure the non-reciprocity of the fiber, or one can block the interface to the fiber under test and use the *null measurement* path instead, where beams travel exclusively on the optical bench, and thus measure the non-reciprocal noise of the setup itself. The latter was done in the noise investigations

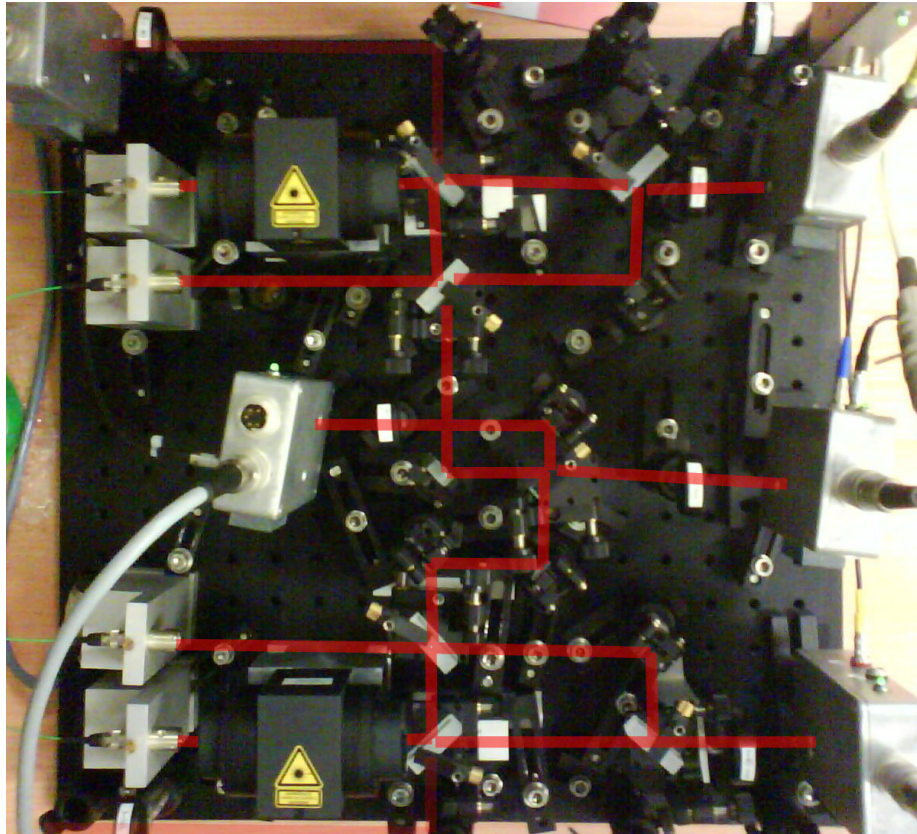


Figure 3.6.: Non-reciprocity interferometer setup on an aluminum base plate. C.f. [34]

presented here, and only after the setup noise was found to be in compliance with the requirement was the non-reciprocity of an actual fiber measured.

### 3.2.1. Aluminum base-plate

Initially, the experiment was set up on an aluminum base plate to gain experience with the relatively complex optical layout and to verify the general measurement principle before implementing it on an ultra-stable optical bench (in fact, such a complex layout had not been set up on an ultra-stable optical bench at the AEI before). This also helped in the development and assessment process of the phase measurement equipment, including the phase-meter and the photo detectors.

Figure 3.6 shows a photograph of this setup with the normally invisible beams indicated in red. It was built on a 45 x 45 cm size aluminum bread board. This allowed the transportation of the setup, and consequently the use with different lasers as input and also installation in a vacuum chamber. This led to a relatively densely populated optical setup.

To get a better overview over the measurement setup, a schematic of this setup is presented in Figure 3.7. The light from the master laser is brought onto this

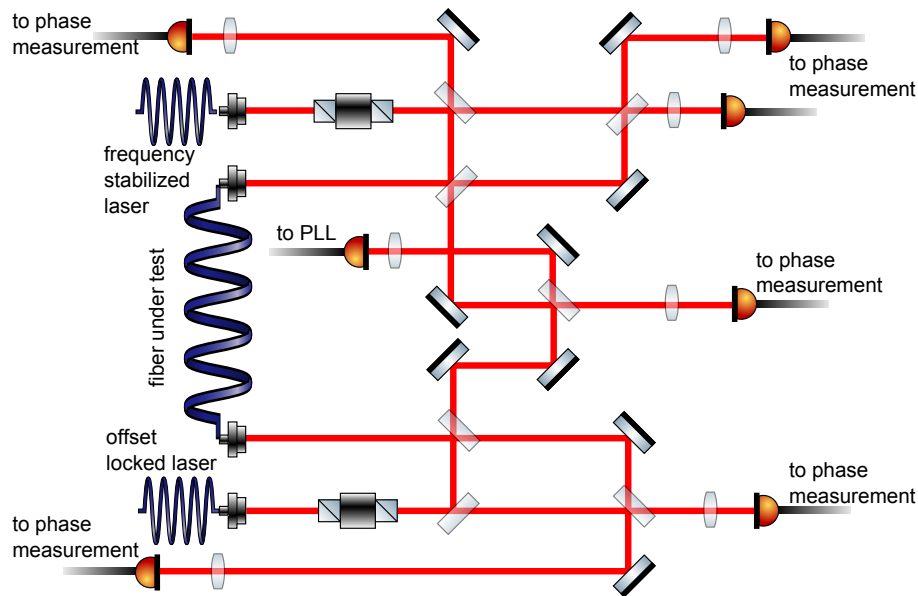


Figure 3.7.: Schematic of the setup on an aluminum base plate.

base plate through a fiber connected to the fiber coupler in the upper left hand side of the picture. The second laser, which is to be offset-locked to the first one is connected via a fiber to the fiber coupler in the lower left hand side of the picture. The measurement principle remains almost unchanged from the design presented in the previous section, with the notable difference that one output port of the REF interferometer, located in the center of the picture, is used in a phase-locked loop (PLL) to stabilize the frequency difference between the two lasers. The MEAS1 and MEAS2 interferometers can be found in the upper right and lower right of the picture, respectively.

However, it was never expected that an aluminum base plate would provide the necessary long-term path length and short-term beam pointing stability required to achieve pm length noise levels. The coefficient of thermal expansion (CTE) of aluminum of about  $24 \times 10^{-6}$  [35] yields to thermal expansions of about  $10 \mu\text{m}/\text{K}$  on a typical 45 cm square base plate.

Frequency stabilization was accomplished by using a master laser that was frequency stabilized to a reference cavity [36, 37] and offset locking the second laser to it. Such a phase lock is not easily possible using offset frequencies of less than a MHz, due to the high inherent laser power noise in this frequency range. Therefore, an offset lock at 20 MHz was implemented.

To measure the phase using the software phase meter available at that time, the measurement frequency had to be reduced from 20 MHz to the kHz operational range of the phase meter. This electronic down-mixing scheme is illustrated in Figure 3.8. One photo diode was used to detect the beat signal between the local laser and the frequency stabilized laser. This signal was used in an analog PLL to

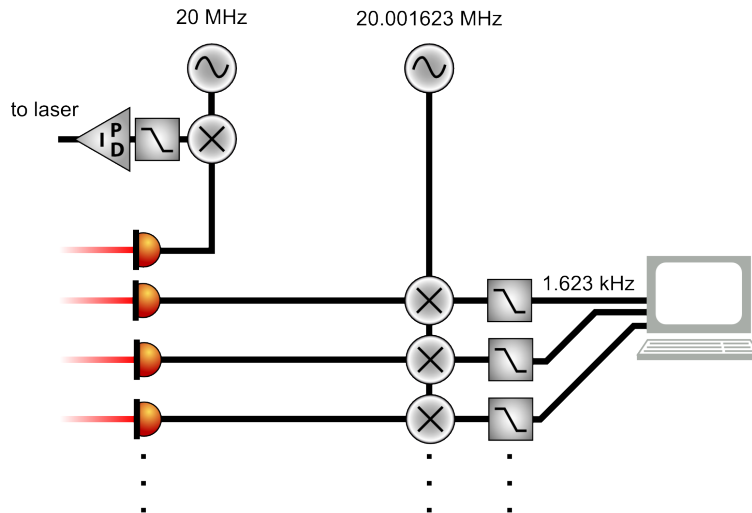


Figure 3.8.: Illustration of the down-mixing scheme used to measure 20 MHz signals using a phase meter operating in the kHz range.

offset lock the local laser's frequency to the frequency stabilized laser, thereby both supplying a stable heterodyne frequency and frequency stabilized light.

All other photo detectors in the setup will then detect beat notes at the offset locking frequency, in this case at 20 MHz. The phase of this signal contains length change information that is required in the experiment. Each beat note signal was fed into a mixer and mixed with a 20.001623 MHz signal from a signal generator electronically phase locked to the signal generator providing the 20 MHz reference signal for the offset lock. The output of the mixer was low-pass filtered, thus eliminating the second harmonic near 40 MHz that was also generated in the mixing process and yielding a 1.623 kHz beat note appropriate for measurement in the phase meter.

Using this setup it was possible to detect the phase of all optical signals and calculate the non-reciprocal noise. The noise levels observed here are shown in Figure 3.9. However, it can also be seen in the same figure that the measurement noise, obtained replacing the fiber under test with two mirrors that guide the light to the MEAS1 and MEAS2 interferometers, is at a similar level, leading to the conclusion that the non-reciprocal noise stems from the setup itself and is not generated inside the fiber (at least not at this level).

Despite much effort to improve the setup and the phase measurement system, noise levels could not be reduced further. Therefore, it was decided to move on to an improved setup, implemented on a Zerodur™ base plate using hydroxide catalysis bonding.

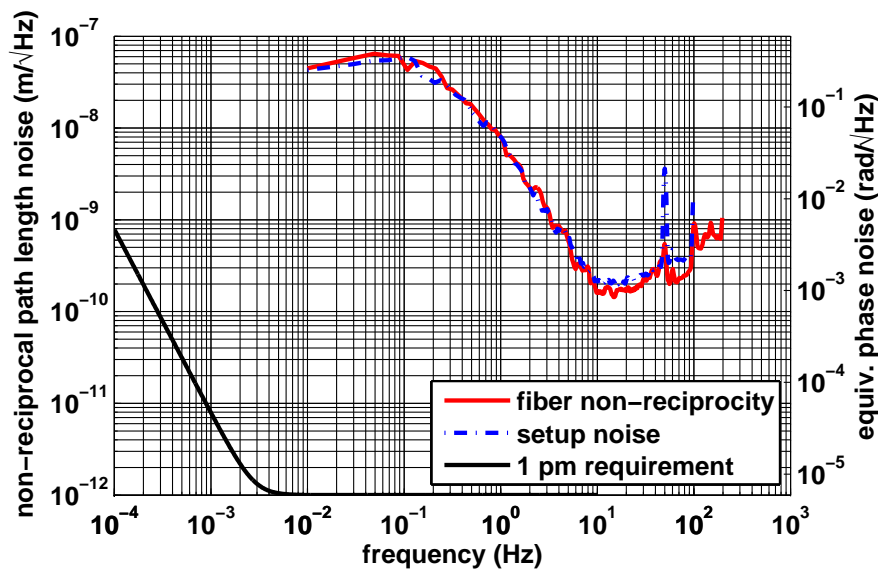


Figure 3.9.: Comparison of fiber non-reciprocity and null measurement performed on an aluminum base plate in air.

### 3.2.2. Zerodur™ base-plate

As detailed in the previous sections, a number of reasons led to the adoption of Zerodur™ as a base plate material for further experiments. It has the inherent advantage of a low coefficient of thermal expansion and – combined with the technique of hydroxide-catalysis bonding – very stable, quasi-monolithic interferometers can be built [38].

However, the advantage of a quasi-monolithic interferometer brings with it the disadvantage that no more alignment is possible after the interferometer is built. Therefore, very careful planning is required before the build process can be started. This is described in the following subsections.

#### Mechanical stability analysis

Some attention to the mechanical stability of the Zerodur™ optical bench is required to ensure correct functionality of the interferometer to be set up on it. The most stringent constraint on the mechanical stability of the base plate arises from the application of interferometry to the optical signals. For this technique to work it is mandatory that the interfering beams be co-aligned to a precision of much better than a few hundred micro radians [39] ( $\approx$  tens of arc seconds).

The ultimate limit of co-alignment is given by the tolerances of the optics to be used for bonding. As there is no possibility to align them during or after bonding them to the optical bench in the direction perpendicular to the base plate, it is

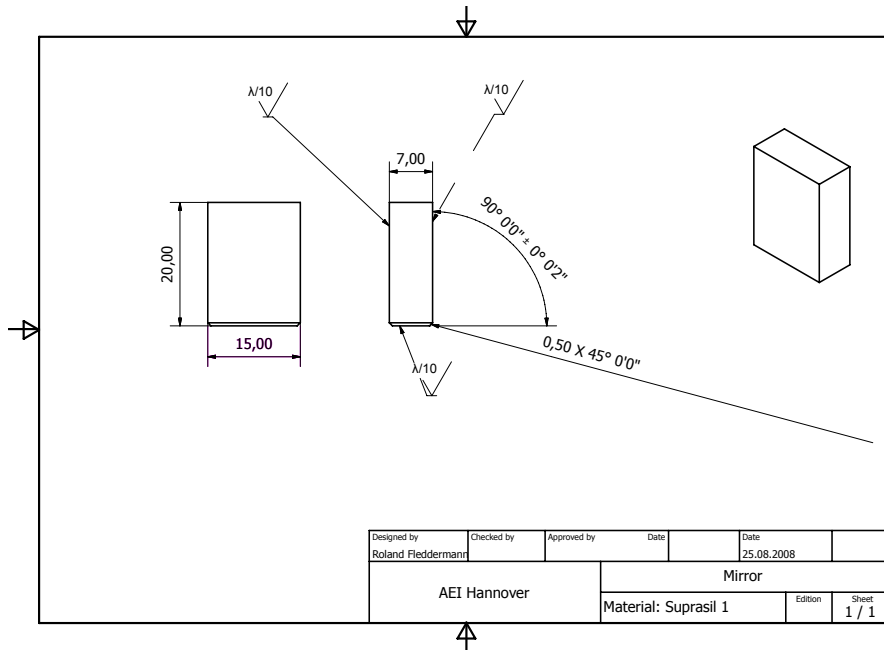


Figure 3.10.: Technical drawing for the specification of the mirrors used for bonding. All dimensions are given in mm.

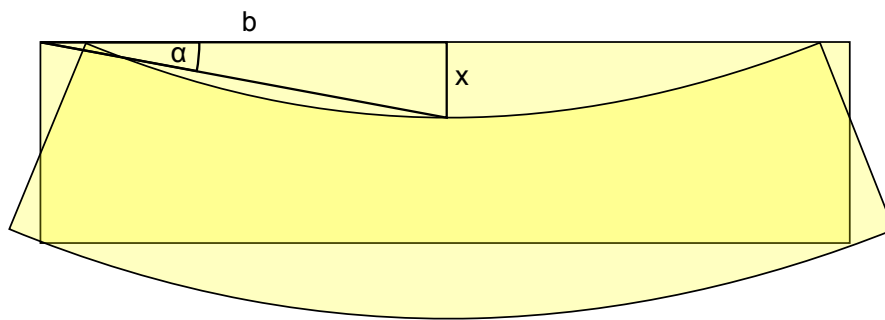
necessary for them to be made such that the angle between the surface contacting the optical bench and the optically active surface be as close as possible to  $90^\circ$ .

Manufacturing tolerances allow the construction of components with an angle which only deviates from the ideal  $90^\circ$  by  $\pm 2$  arc seconds. This is reflected in the technical drawing shown in Figure 3.10 of a mirror to be used for bonding.

In order to not waste the effort to which the manufacturer is put in order to meet these tight requirements, it is advisable to choose the base plate thickness such that it does not deform under gravitational load in a way that leads to a greater angular deviation after the components have been put in place. This would be the case if the base plate sags in the middle due to gravity. This effect is unavoidable but has to be kept below a certain threshold. A reasonable choice for this threshold is to require that the surface angle introduced from the sag of the base plate is to be kept below one tenth of the angular tolerances of the components, such that only after ten reflections from the components the accumulated change in direction of the beams is of the same magnitude as the angular error due to the manufacturing tolerances.

To model the sag, a worst case scenario is assumed, where the base plate is only held at its edges and can deform freely under its own weight. This will lead to a symmetrical sag such that the center of the base plate is slightly deeper than the corners. The corresponding change in angle of the surface was found by dividing the height difference in the center by half the side length (a square shape of  $200 \times 200$  mm was assumed). This gives the tangent of the angle, which for





$$\tan(\alpha) \approx x/b$$

Figure 3.11.: Illustration of the angle introduced through bending of the base plate under gravitational load.

such small angles is a very good approximation of the actual angle (in radians), as illustrated in Figure 3.11.

A first analysis was performed using Autodesk Inventor 2009 and its integrated Ansys© finite element simulation mode. A “fixed” constraint was put onto two opposite sides of the plate and a gravitational load in the minus z direction (i.e. perpendicular to the largest surface) was applied. The simulation was performed for base plates of varying thickness between 10 mm and 50 mm in 10 mm steps.

Figure 3.12 shows the deformation found for a base plate of 10 mm thickness. The color represents the magnitude of the deviation from the shape without gravitational load. Two opposite edges are shown to be in the same position as without load. This is because these edges were fixed for the simulation to model holding the base plate at its edges. In between, the base plate bends with a U-shape. The maximum deformation is found in the middle, as expected. The amount of sag in the middle was taken from the reports that were generated by the program and collected in a text file for analysis.

Closer examination of the text file showed a roughly inverse thickness squared correlation between the maximum sag and the thickness of the base plate. This is shown in Figure 3.13. The red crosses represent the data points from the simulation and a  $a/x^2 + b$  curve fit is shown in green. The parameters of the plot are shown in the legend. While the left y-axis of the plot shows the deformation of the base plate, the right hand y-axis shows the resulting angular deviation of the surface in arc seconds using the approximation mentioned above. The components’ tolerance of 2 arc seconds and one tenth of the components tolerance are also shown for reference. From the intersection point of the fit and the 0.2 arc seconds line it can

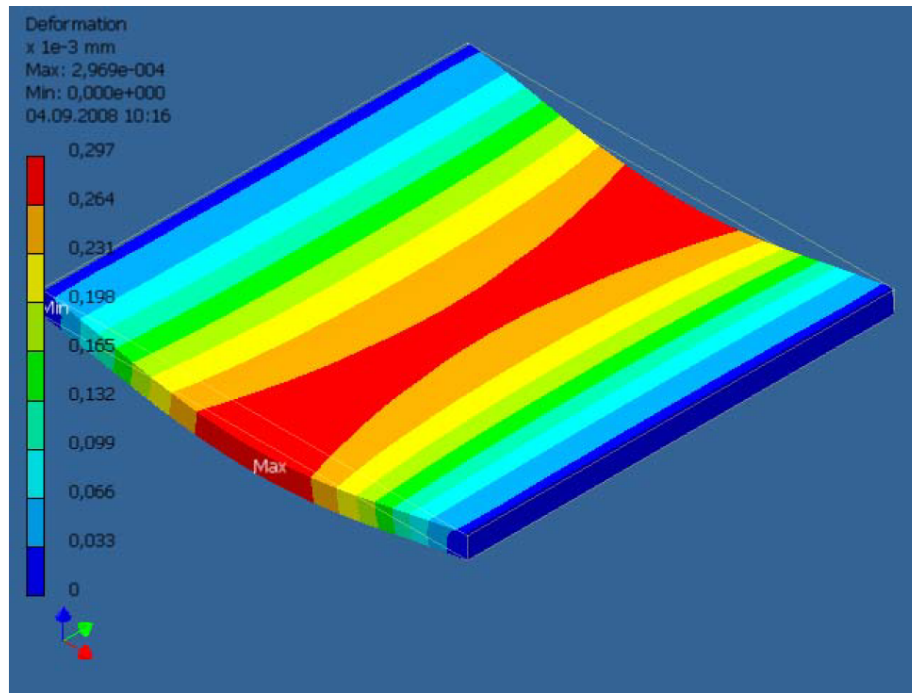


Figure 3.12.: Deformation analysis of a 10 mm thickness Zerodur™ base plate performed using Autodesk Inventor®.

be seen that a base plate thickness of at least approximately 18 mm is required to keep the angular deviation due to deformation of the base plate well below the components tolerance. As mentioned above, a factor of one tenth has been chosen to account for the combined error that can potentially occur due to the reflection from multiple components that are all leaning in the same direction; with typically 20 components on a base plate, 10 reflections can easily occur in a beam path.

This numerical approach has the inherent disadvantage that it is hard to verify the validity of the values obtained. To gain more confidence in the simulation results, the simulations were followed by calculations using a (semi-) analytical approach using plate theory as described in [40]. In this book a formula is derived to mathematically model the effect of a static, uniform load on a rectangular plate of width  $a$ , length  $b$  and height or thickness  $h$ . It consists of several equations and is a bit long, so it is not copied here for brevity. The interested reader can find it in Appendix B in the MATLAB® source code used for the numerical computations.

The parameters used in the calculations are as follows: The width and length of the plate are both 200 mm. The static, uniform load per unit area was calculated from the thickness, which was varied between 5 and 100 mm, and width and length of 200 mm each. Using the density of Zerodur™ of  $2.53 \text{ g / cm}^3$ , this yields the weight. The weight was then multiplied with the gravitational acceleration at sea level of  $9.81 \text{ m/s}^2$  and divided by the area of the base plate of  $0.04 \text{ m}^2$ , yielding the stress.

Other parameters needed for the calculation include Young's modulus, which is



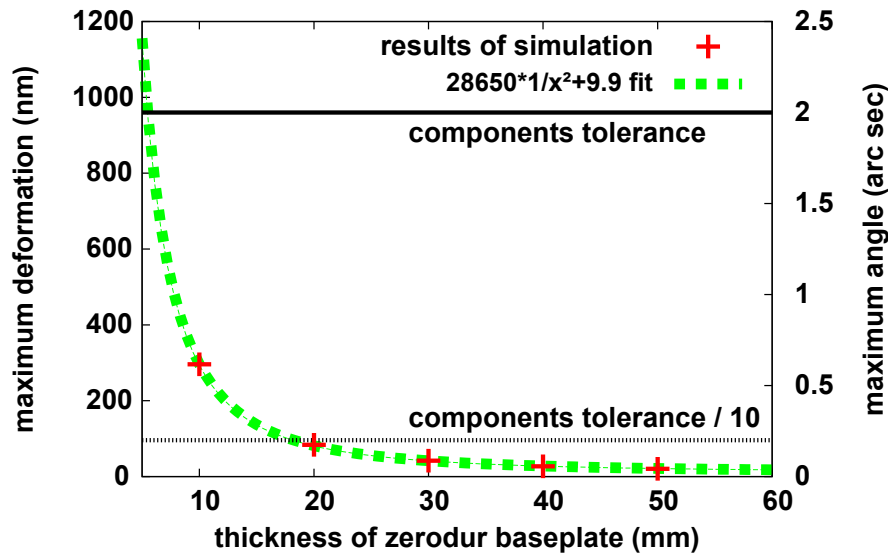


Figure 3.13.: Simulation of maximum deformation/angle of a 200 mm x 200 mm Zerodur™ base plate of varying thickness.

90.3 GPa for Zerodur™ and its Poisson's ratio, which was found in the literature [41] to be 0.243.

Unfortunately, the approach outlined in [40] involves the computation of many Fourier components and dividing the plate into several blocks for which individual computations are necessary, so it was still necessary to perform the computations numerically. MATLAB© was chosen for the implementation. The corresponding MATLAB© code can be found in Appendix B.

Figure 3.14 shows the results of one such simulation for a 10 mm thick base plate. A 3D plot is shown where for each position on the plate its deviation from the original position without gravitational load is represented by color and position. As expected, the point in the middle of the base plate sags away most and the bending is symmetrical. The magnitude of the deformation is about 75 nm.

In order to compare these results to those obtained using Autodesk Inventor© the Inventor simulations had to be repeated with all four sides constrained. This was implemented in the simulation and the computations were repeated for values of the base plate thickness of 5, 10, 20, 30, 40, 50, 75 and 100 mm, respectively. Again, the resulting maximum deformation was put into a text file to be able to compare it to the results obtained using the plate theory approach.

The results of these computations are compared with the finite element approach in Figure 3.15. One can see that the results are very similar for thicknesses around 50 mm. At lower thickness, the finite element simulation gives slightly higher deformations and corresponding angular deviations than this analytical approach, while for relatively high thickness the situation is reversed. The plate theory approach seems to give a too low estimate of the deformation, probably owing to

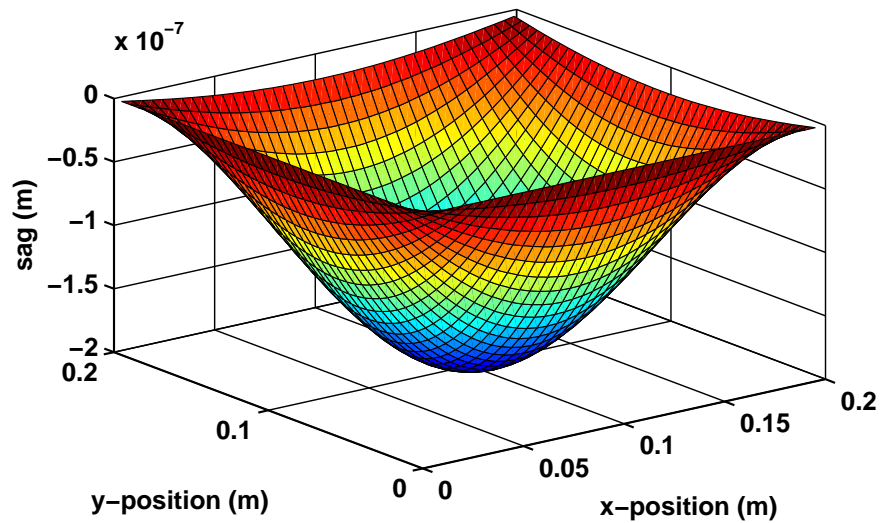


Figure 3.14.: Simulated bending of a 10 mm thickness Zerodur™ base plate under gravitational load.

the fact that it is meant to be used for plates, where one dimension is significantly smaller than the other two. This is no longer the case when the thickness approaches 0.1 m when the two other sides are 0.2 m long.

However, the different approaches agree at least to better than within one order of magnitude. For the base plate thickness of 50 mm that was adopted, the agreement is excellent and the worst case angular deviation is still well below the components angular tolerance.

### Fiber mounts

While on the real LISA optical bench quasi-monolithic, bonded fiber coupler assemblies (fiber injector optical sub-assemblies, FIOS, [42]) will deliver the light from the laser to the optical bench, such devices were not available to us at the build time of the interferometer. Development was finished only recently in the frame of the LISA optical bench contract by colleagues from the University of Glasgow, after the experiments described in this work were conducted.

Such fiber injector optical sub-assembly (FIOS) present very intricate alignment challenges, especially in the case of the reciprocity interferometer, where light has to be coupled from the optical bench into the interferometer while at the same time light from the FIOS has to be adjusted for interference in the measurement interferometers. Both are challenging alignment tasks on their own, but in this case they would have to be done simultaneously under the time pressure set by the nature of the bonding process which allows for maybe 60 seconds before the bond cures and the component to be aligned can no longer be moved.

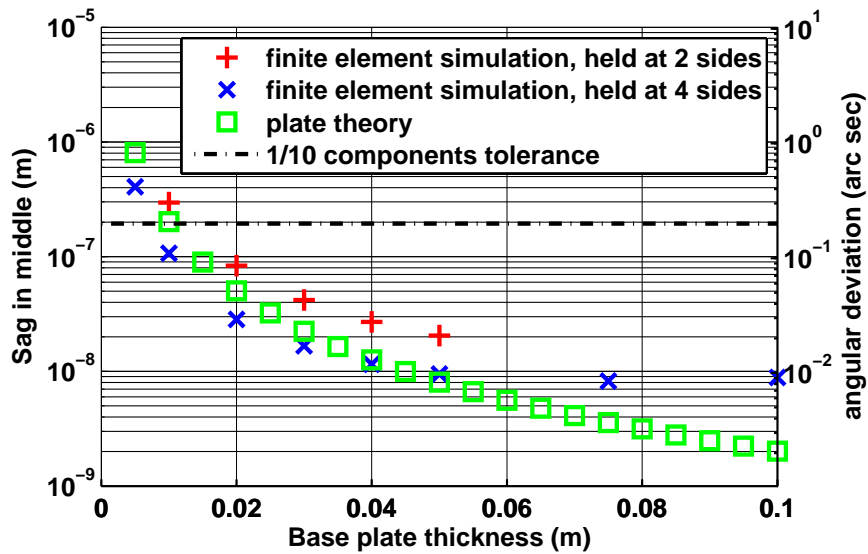


Figure 3.15.: Comparison between the bending found using finite element simulations and plate theory calculations.

As the non-reciprocity interferometer was at that time the most complicated interferometer to ever have been built at the AEI (using 16 optically active beam splitters and mirrors in total, plus four components used for alignment (not shown in the rendering in Figure 3.16), which is only slightly less than the 21 components of the LISA Pathfinder engineering model optical bench) it was decided to avoid the additional challenges involved in using quasi-monolithic fiber injectors but to use commercial off-the-shelf (COTS) adjustable fiber couplers instead. It was clear that this would compromise the pointing stability of the beams on the optical bench, but this was deemed tolerable in the light of the greatly reduced complexity of the interferometer setup process.

To at least achieve the maximum possible stability using these COTS components, great care was taken to choose mounts with solid state hinges and micrometer adjustment screws. These features promise the highest possible stability while maintaining sufficient alignment clearance.

Using the optical layout simulated with IFOCAD [43] / OptoCad [44] and some extensions to IFOCAD it was possible to generate a POV-Ray [45] input script that allows one to render a photo-realistic image of the base plate before it is actually built as shown in Figure 3.16. This allows the identification of potential problems early on in the design process, before one goes ahead and builds the bench, which cannot be taken apart without destroying it.

Figure 3.17 shows a photograph of the *actual* base plate after it has been built, with the beams also indicated in red. By comparing these two figures, one can see that the simulation gives a very accurate indication of the finished interferometer.

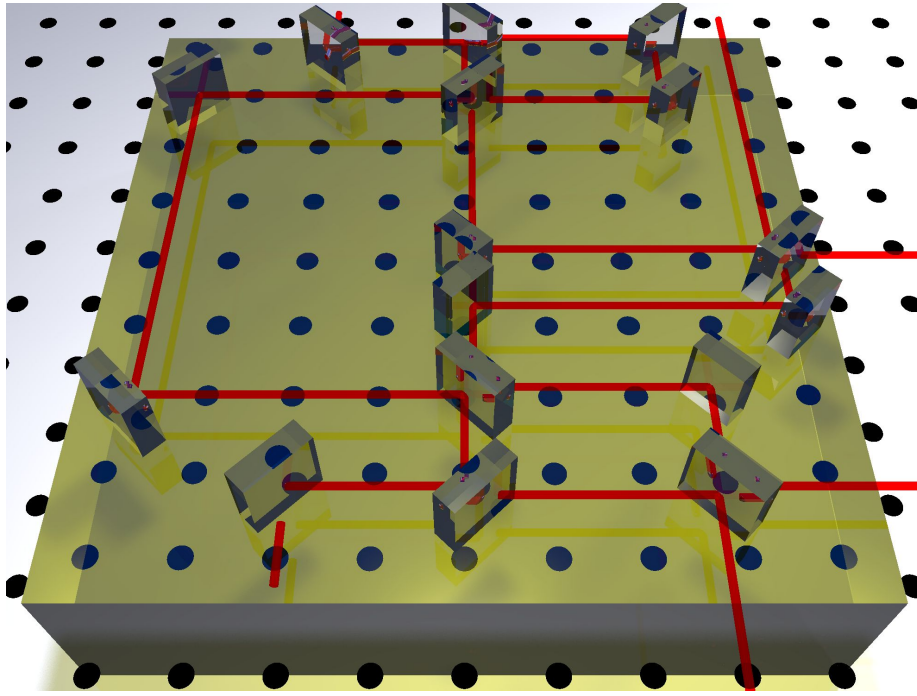


Figure 3.16.: POV-Ray rendering of the Zerodur™ optical base plate with all optical components installed and laser beams indicated in red.

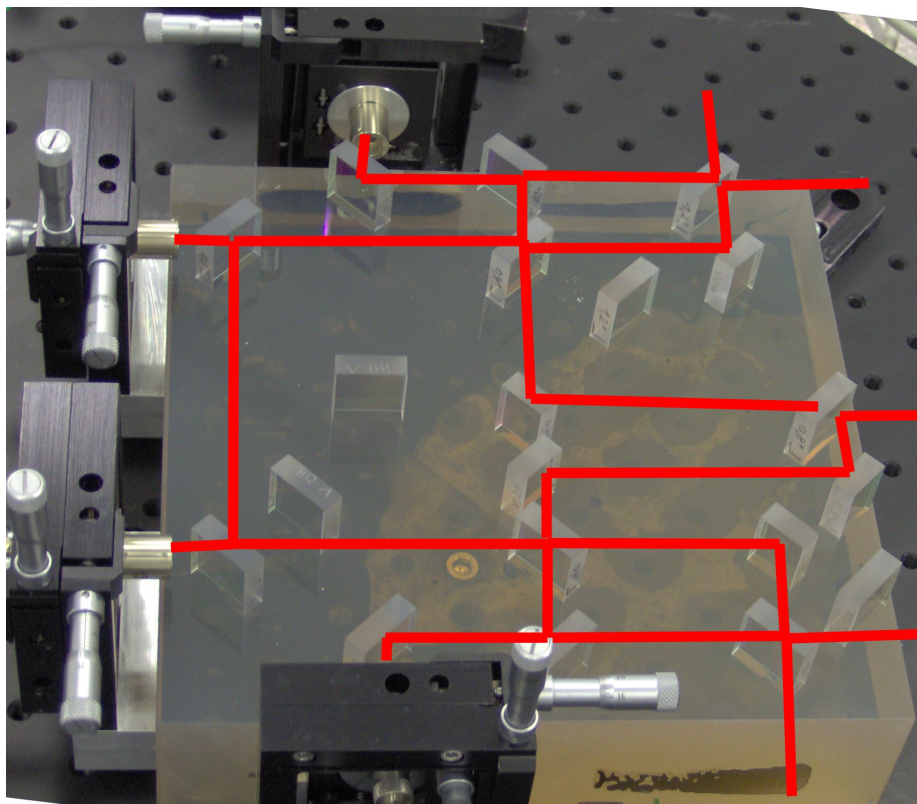


Figure 3.17.: Actual Zerodur™ base plate with laser beams indicated in red.

## Ghost beam analysis

After the optical setup was adopted for the Zerodur™ base plate, a thorough ghost beam analysis was made to identify potential sources of residual reflections coupling into the main measurement path. Special attention was paid to the beam splitters, as parallel beam splitter surfaces in unfavorable configurations can lead to round trip paths for the reflected light that recombine the ghost beam with the nominal beam, making the spurious ghost beam and the nominal beam generally indistinguishable.

The ghost beam analysis was performed using OptoCad, using the original layout but also including reflections from the anti-reflective (AR) coated secondary surfaces of the optics in use. While the AR coatings usually suppress residual reflections down to about 0.1 %, they still remain present and can lead to significant disturbances in interferometry, especially since 0.1 % of the power corresponds to 1/30 of the interfering amplitude.

Figure 3.18 shows the output of the OptoCad simulation. As can be seen, many ghost beams are present; some of which take the unfavorable path where they recombine with the nominal beam, as can be seen when one examines the path highlighted in green. Light coming from the direction indicated by the black arrow is partially reflected by the AR coatings on the secondary surfaces of beam splitters BS5 and BS6 in front of the interface to the fiber under test and afterwards it takes the same path as the light reflected on the primary surfaces as intended.

The customary way to avoid such a situation is to use wedged optics. While generally a good design principle, this could not be achieved here due to two reasons. Firstly, wedged beam splitters were not available at the time the interferometer was built; secondly, wedged beam splitters can not be used in a setup where one expects angular jitter, as the jitter will couple to length fluctuations in this case.

Additionally, due to the tight requirements on the perpendicularity of the main surface with respect to the base, these components have long lead times. It was therefore decided to go ahead with the original design .

## Interferometer build process

After considering all the inherent design challenges resulting from the decision to use a quasi-monolithic interferometer built using hydroxide catalysis bonding on a Zerodur™ base plate, the build process could finally begin. It is not described here in detail for the sake of brevity, but the reader is kindly referred to references [46, 34], which deal with the build process in detail.

The final design of the interferometer is shown in Figure 3.19. Light is brought in from the bottom and top, from the positions labeled “Beam 1” and “Beam 2” through fiber couplers not shown in this schematic. The two measurement interferometers and the reference interferometer can be found on the right hand side while the fiber under test is shown on the left hand side.

This optical layout was used to generate a template to assist in the placement of

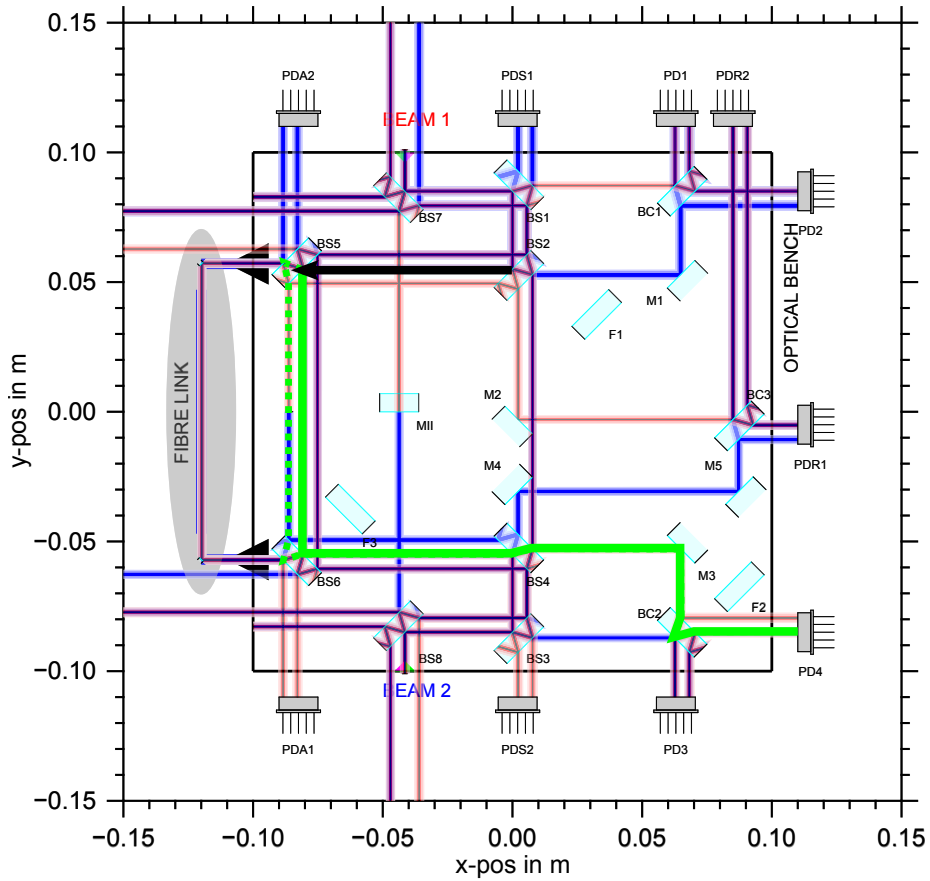


Figure 3.18.: Ghost beam analysis on Optocad model of the Zerodur™ optical bench

the non-critical components on the optical bench. Figure 3.20 shows a CAD model of this template, generated using Autodesk Inventor©. It has pockets for each component with holes at two sides that can hold metal spheres of 4 mm diameter in such a way that they stick out one millimeter into the opening. This arrangement assures that a component that is put into one of the pockets will be supported at exactly three points, allowing to precisely position it.

The template was manufactured by the mechanical workshop of the AEI, which allowed for a precision of about 0.1 mm for all measures. This is enough for all beam steering optics to assure that beams are guided to the intended design interference points. However, in order to achieve good interferometric contrast, an even better angular alignment is required, which demanded a special tool, as is described in [34].



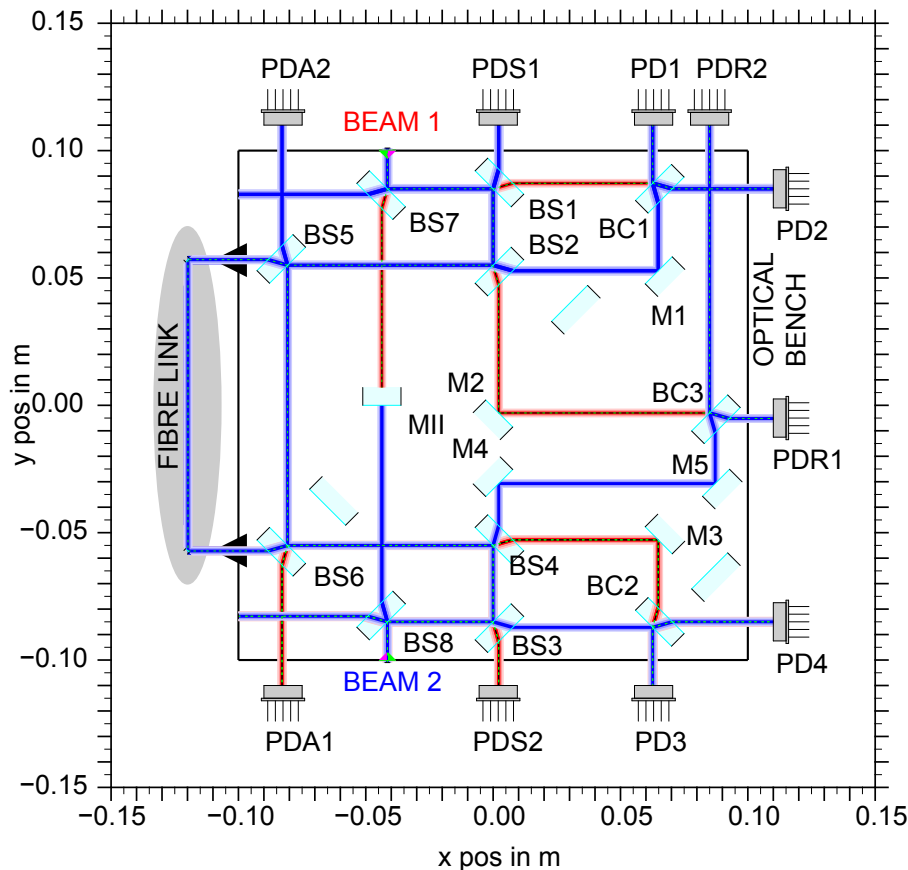


Figure 3.19.: OptoCad design of the interferometer optical layout on Zerodur™ base-plate, c.f. [34]

### 3.3. Phase measurement noise

Before measurements of the non-reciprocal noise of the fiber under test were made, testing of the phase measurement system was performed. As measurement noise is ultimately limited by the ability of the phase meter to measure the phase of heterodyne beat notes, this provides the basis for all further measurements.

At the time the measurements were conducted, two phase meter options were available. The first one consisted of a PC with an analog-to-digital converter (ADC) card installed. This card featured an ADC with 16 bit resolution and a sampling rate of up to 200 kHz. To allow for the measurement of several channels simultaneously, multiplexing was employed. Using this technique it was possible to sample analog data at a sampling frequency of up to 20 kHz using 10 channels. Data was then processed in the computer. A discrete Fourier transform (DFT) was performed in software and the resulting phase at the (configurable) heterodyne frequency was extracted and saved to disk for later data analysis.

The second phase measurement option was using a breadboard of the LISA



Figure 3.20.: CAD model of the template used to align the optical components on the Zerodur™ base plate

Technology Package (LTP) phase meter, developed at the AEI [47]. It uses one dedicated ADC for each phase meter channel. One FPGA chip based electronics board was used per channel to read the ADC data with a sampling rate of 800 kHz and a resolution of 18 bit and to perform the single-bin discrete Fourier-transform (SBDFT). Then one more FPGA read out the greatly reduced amount of resulting data from up to 20 of these boards and prepared data to be read out by a host PC via the parallel port. The use of FPGAs to read out and pre-process the ADCs became necessary due to the large amount of data generated by all these ADCs, exceeding available data transfer rates to PCs. The host computer finally performed the inverse tangent operation required to compute the phase from the raw SBDFT data supplied by the FPGA (these operations are difficult to implement in FPGA hardware and take up a lot of the available gates). Again, phase data was computed and stored in a disk file for later analysis.

A number of measurements using electrical input signals were performed to verify the correct operation of these phase measurement devices and to characterize their phase measurement noise, which ultimately limits the ability to detect phase changes in the experiments.

The general measurement setup is shown in Figure 3.21. A signal generator was connected to a power splitter and the two resulting output signals were then fed into two independent channels of the phase meter. Data was recorded and the difference between the phases measured for both nominally identical signals was calculated.



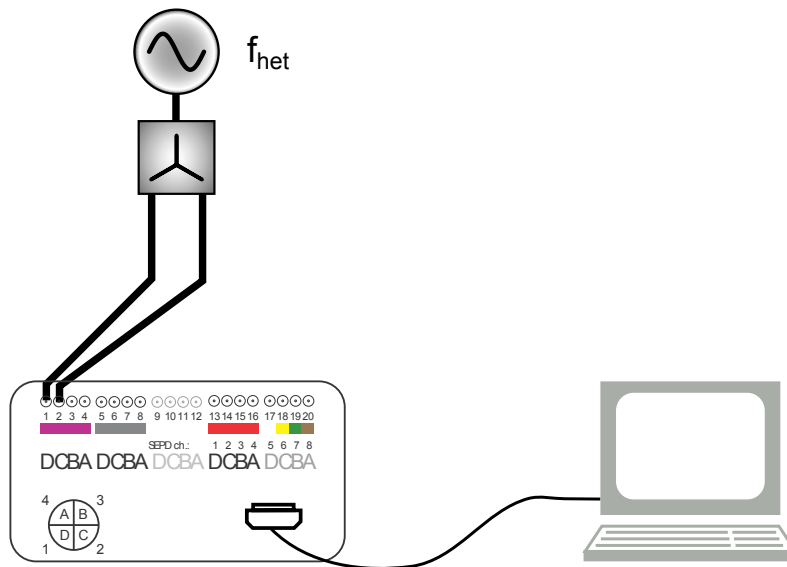


Figure 3.21.: Test setup used to measure the phase measurement noise of the phase meter using electrical signals.

Results using this setup to test the software phase meter are presented in Section 3.3.1. The phase measurement noise of the FPGA-based phase meter can be found in Section 3.3.2.

### 3.3.1. Software phase meter measurement noise

The phase noise of the software-based phase measurement system was measured first, using the technique described above, i.e. by feeding nominally identical electrical sinusoidal signals into two independent channels of the phase meter and computing the difference. Ideally, the difference should be exactly zero, but due to measurement imperfections some noise will always be present. To further investigate the effect of imperfect, i.e. noisy input signals, the same was also done with white noise of different amplitudes added to the originally very low noise signals of the signal generator. The white noise was added before the signal was split to the two phase meter channels. Figure 3.22 shows the results of these measurements. All noise spectral densities show a flat spectrum. Furthermore, as is expected, the phase noise increases with the addition of white noise to the input signals. The lowest noise of about  $1 \text{ pm}/\sqrt{\text{Hz}}$  is observed with ideal signals, shown in cyan. All other traces lie above the requirement, which is shown in black. This figure also shows that phase noise performance of the software phase meter is marginal and even the addition of minute disturbances increases phase noise above the requirement.

Therefore, it was decided to change to the FPGA-based phase meter. Phase

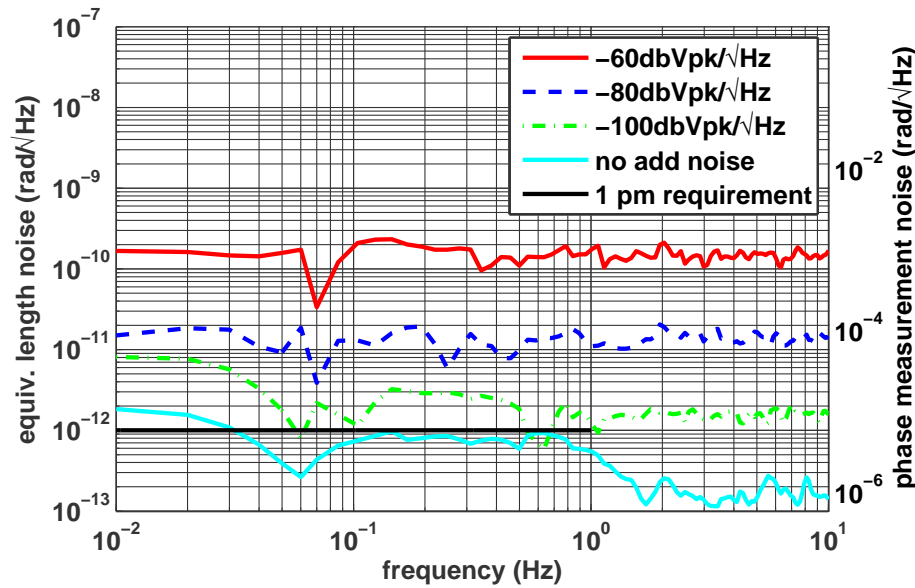


Figure 3.22.: Test of phase meter noise using electrical signals with added white noise.

noise measurements of the FPGA-based phase meter are discussed in the following subsection.

### 3.3.2. FPGA based phase meter measurement noise

To measure the electrical noise of the phase meter, electrical sinusoidal signals generated by a signal generator were connected to two of its input channels. This gives a lower limit on phase meter noise, because it characterizes the ability of the phase meter to measure an ideal sinusoidal signal without (much) phase and amplitude noise.

To evaluate the influence of the input signal's amplitude on the measurement noise, the measurement was repeated with various input signal amplitude settings, ranging from  $20 \text{ mV}_{p-p}$  (the lowest possible setting of the signal generator) to  $2.55 \text{ V}_{p-p}$  (the highest allowable input signal of the phase meter). As one can see in Figure 3.23, the phase measurement noise increases with decreasing signal amplitude. This can be explained by the higher amount of digitization noise introduced using lower signal levels and therefore a lower number of effective bits.

The dependence of the noise amplitude on signal amplitude can be seen more clearly in Figure 3.24. Here, the amplitude of the noise at 10 Hz is plotted against the input amplitude. The data points all fall nicely onto a  $1/\text{amplitude}$  line which is also shown in the figure in red. From this it can be inferred that a minimum signal amplitude of about  $40 \text{ mV}_{p-p}$  must be maintained in order to get a phase meter noise compatible with the  $1 \text{ pm}$  requirement. However, this can only be regarded as a lower limit on the minimum amplitude as actual photo diode signals

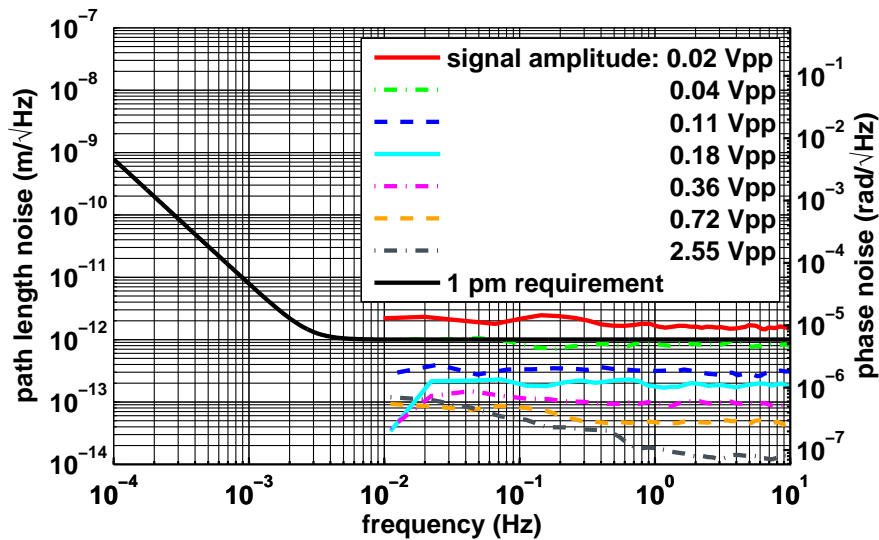


Figure 3.23.: Phase measurement noise using different input signal levels from a signal generator.

are likely to be more noisy and thus to show a higher phase measurement noise. This is discussed in more detail in Section 3.4.

In actual non-reciprocity experiments signal levels were kept as high as possible. For later measurements an additional photo diode was installed to measure this noise source, as presented in the following Section 3.4.

### 3.3.3. Comparison of both phase meter options

For comparison, the measurement of the lower phase noise limit was also made using an older software phase meter (PM2). For this measurement, the same setup was used as before, but this time the old phase meter was connected to the outputs of the trans-impedance amplifiers integrated into PM3 for monitoring purposes.

The spectrum of the difference of these signals can be found in Figure 3.25. It can be seen that the lower noise limit of the FPGA-based phase meter (PM3) is significantly below the noise of the software phase meter (PM2). It is below the requirements in the whole spectral range, which is a requirement for the measurement of non-reciprocity down to this noise level.

## 3.4. Differential photo diode noise

In Section 3.3 the measurement of phase meter noise using electrical input signals was described. This constitutes only a lower limit of the phase meter noise. In the real experimental setup the signals are not perfect sine waves with a constant

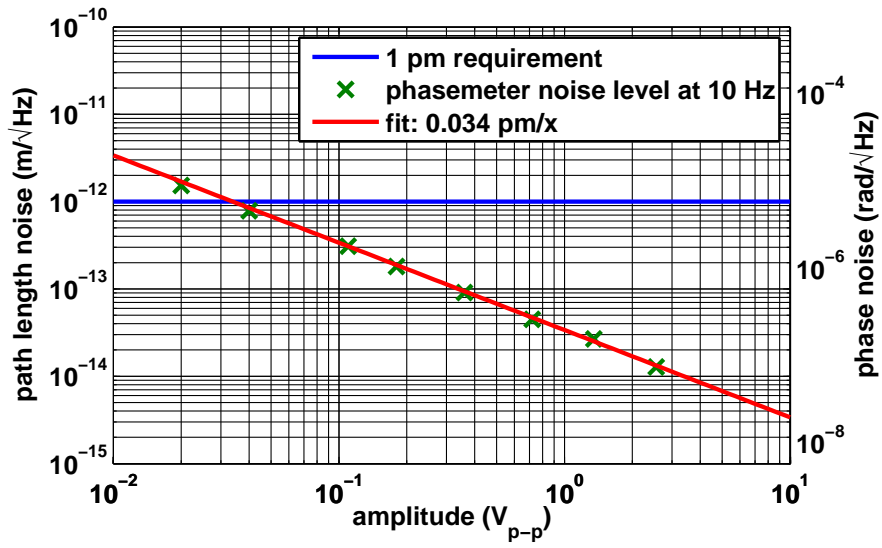


Figure 3.24.: Phase measurement noise dependence on input signal level.

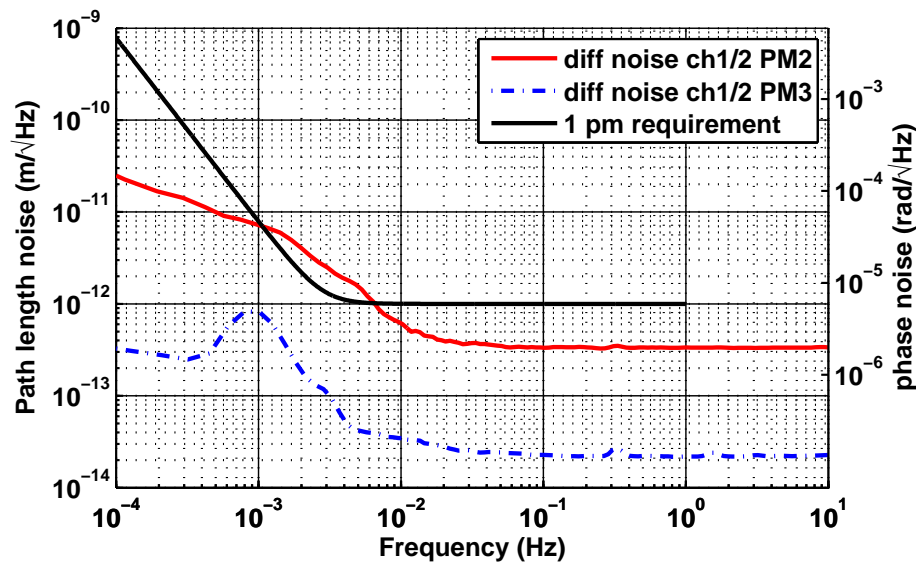


Figure 3.25.: Direct comparison between differential noise observed using a software phase meter (PM2) and a hardware phase meter (PM3).

amplitude; they may have distortions and amplitude noise. Therefore it is necessary to test the ability of the phase meter to measure the phase of such realistic signals.

In order to measure this noise, the setup was slightly changed to include an additional photo diode. A schematic of this modified setup is shown in Figure 3.26. The additional photo diode is denoted in the right hand part of the figure by the arrow labeled “New PD”. This photo diode is used to measure the phase of a beam that is split off one of the two reference interferometer outputs. The phase observed at this point should exactly match the phase observed at the original interferometer output found in the upper right part of the figure. One can therefore calculate the difference between the two phases observed by the two photo diodes and thus get a measure of the *differential photo diode noise*.

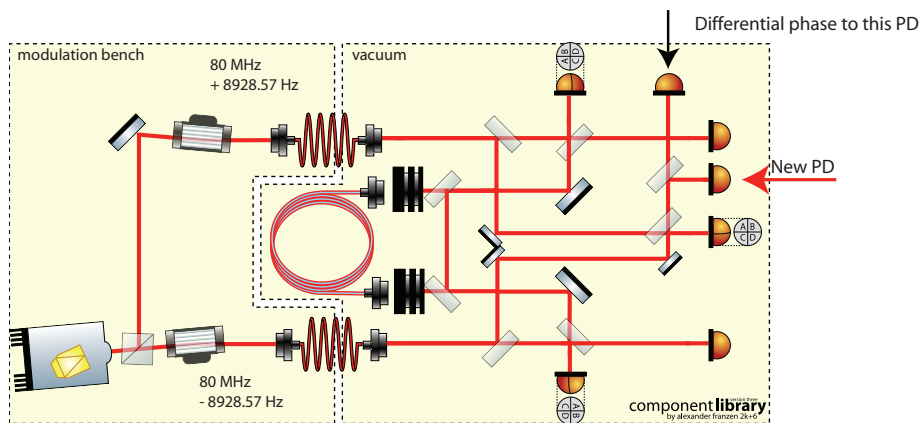


Figure 3.26.: Setup for the measurement of differential photo diode noise.

Initial measurements using this setup showed that the differential noise found between the signals from the two photo diodes sensing the same split beam is substantially higher than differential noise between two phase meter channels sampling the same electrically fed signal. The respective noise spectral density plots are shown in Figure 3.27. Here, the red, solid trace represents the differential photo diode noise. This noise is at  $0.3 \text{ pm}/\sqrt{\text{Hz}}$  for frequencies above one Hertz, increasing roughly as  $1/f$  toward lower frequencies. It violates the  $1 \text{ pm}$  requirement at frequencies below  $0.1 \text{ Hz}$ . The electronic noise of the phase meter is represented by the blue, dashed trace. This noise has an amplitude of about  $0.05 \text{ pm}/\sqrt{\text{Hz}}$  for frequencies above  $5 \text{ mHz}$ . It is also well below the  $1 \text{ pm}$  requirement in the whole measurement band. From this, one can conclude that additional noise is introduced by adding the additional photo diode and beam splitter needed for this kind of measurement.

In order to identify the exact source of this additional noise a series of experiments was conducted where in each experiment one parameter of the measurement process was changed.

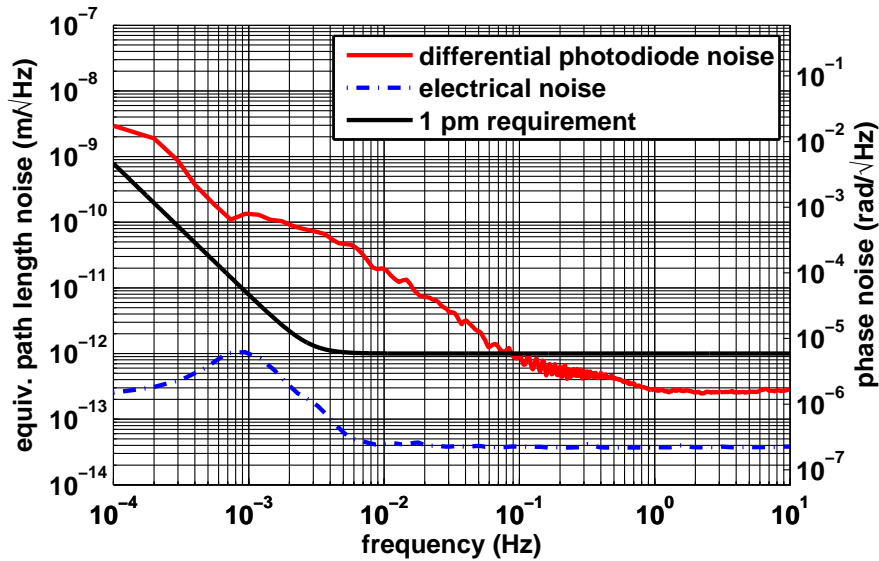


Figure 3.27.: Initial differential photo diode noise compared to the electrical phase meter noise.

### 3.4.1. Effect of removing photo diode windows

The photo diode window can lead to spurious reflections. This is illustrated in Figure 3.28a. Since the window is made from ordinary glass without any anti-reflective coating, about 4% of the light power will be reflected at each air-glass interface. This light is reflected back and forth inside the photodiode housing, which leads to a slight phase change in the measurement signal. Furthermore, a spurious cavity can form between the glass window and the photodiode substrate, because the substrate in the silicon photodiodes does not absorb all the light power but reflects a small fraction of it. This alone would not harm the measurement noise, because it would only lead to a small but constant phase offset. If, however, the distance between the window and photodiode substrate changes, due to e.g. thermal expansion of the photodiode housing, then this changes the phase of this spurious signal and thereby leads to phase noise.

A similar problem can also occur in the window itself. Light can be reflected back and forth between the two ends of the glass layer due to Fresnel reflections, leading to an etalon effect.

In order to avoid this, we used a special tool to carefully remove the photo diode windows without damaging the sensitive photo diode substrate. Figure 3.28b shows photographs of two photo diodes. The left hand photo diode still has the window on; on the right, its window has been removed.

We took measurements of the differential photo diode phase noise first with the windows still on and then with the windows taken off. The results were compared

to see if reflections from the window are responsible for the observed additional noise.

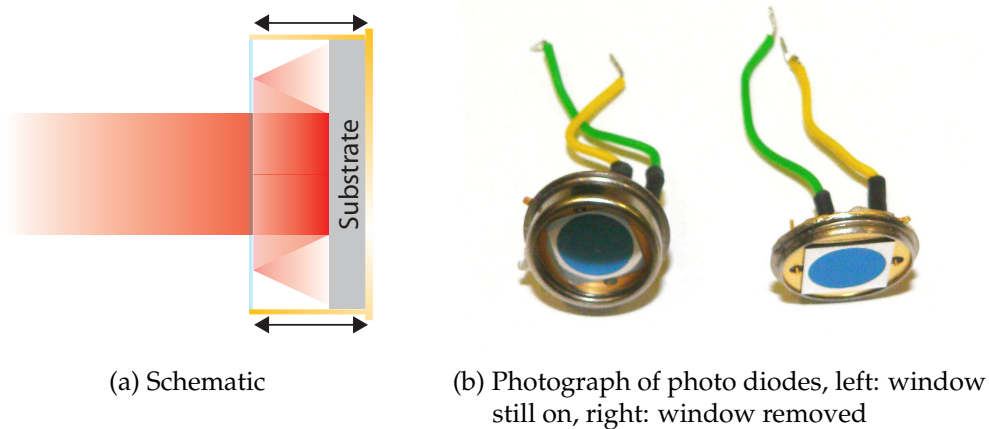


Figure 3.28.: Photo diode windows and their influence on spurious signals.

The noise spectral densities of these measurements are illustrated in Figure 3.29. The figure shows no significant difference between the two traces, which leads to the conclusion that spurious reflections from the photo diode windows do not cause excess differential photo diode noise.

As it was not possible to put the windows back on, it was decided to still keep using the photo diodes with the windows removed, as this did not lead to an increase in observed noise. Furthermore, it eliminates one possible source of noise which could otherwise become dominant if the measurement sensitivity improves.

### 3.4.2. Photo diode substrate material

Another attempt to reduce the differential photo diode noise was made by replacing the silicon photo diodes with indium gallium arsenide (InGaAs) photo diodes. These photo diodes have a higher responsivity for the wavelength of 1064 nm used in our experiments, which potentially leads to higher signals. Furthermore, they have a lower sensitivity in the visible wavelength range, which reduces the influence of ambient light.

In order to evaluate the differential photo diode noise of the InGaAs photo diodes, two silicon photo diodes were replaced by InGaAs photo diodes and the differential phase noise between these photo diodes was measured again. Figure 3.30 shows the noise spectral densities found in this measurement compared to those found in previous measurements using the silicon photo diodes. The noise of the InGaAs photo diodes, represented by the dashed blue trace, is higher than the noise of the silicon diodes, represented by the solid red trace, at high frequencies (above 0.1 Hz). This can be explained by the fact that the signal of the InGaAs photo diodes was lower in the measurements because signal levels were not optimized, which

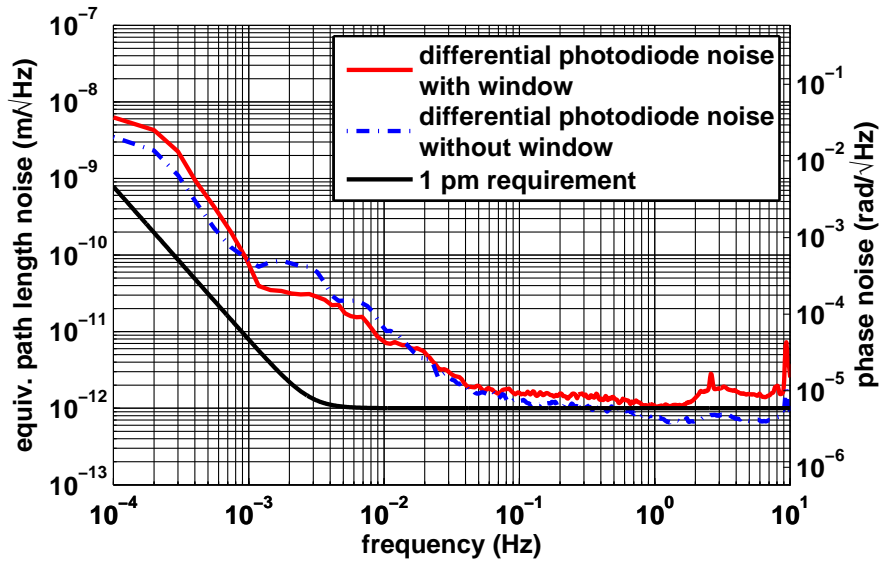


Figure 3.29.: Comparison of differential photo diode noise before and after removing the windows.

increases the digitization noise in the phase meter which is the dominant noise source at these frequencies. For frequencies below this threshold the noise has the same amplitude and shape, indicating that there is no significant reduction in differential photo diode noise through the use of InGaAs photo diodes.

Therefore, it was decided to continue using the silicon photo diodes. The InGaAs photo diodes are only available in relatively small sizes (the ones used for this test had a diameter of 500  $\mu\text{m}$ ) which makes them cumbersome in daily lab use, because additional lenses are needed to focus the beam onto the photo diode and because they are harder to adjust.

### 3.4.3. Vacuum feed-throughs

As the experiment is conducted in a vacuum, feed-throughs are required to facilitate measurement of the electrical signals by a phase meter located outside the vacuum. These feed-throughs carry all the signals on one high-density 50-pin connector. This might lead to crosstalk between adjacent cables and thereby to phase noise. To avoid this, a measurement was conducted with a direct electrical connection between the photo diodes and the phase meter through the open door of the vacuum chamber. The results of this measurement were once again compared to a measurement where the normal feed-throughs were used.

Figure 3.31 shows a comparison between the noise spectral densities observed in measurements with and without the electrical feed-throughs. Both traces lie almost exactly on top of each other. This leads to the conclusion that the electrical crosstalk in the feed-throughs is negligible and that they need not be redesigned.



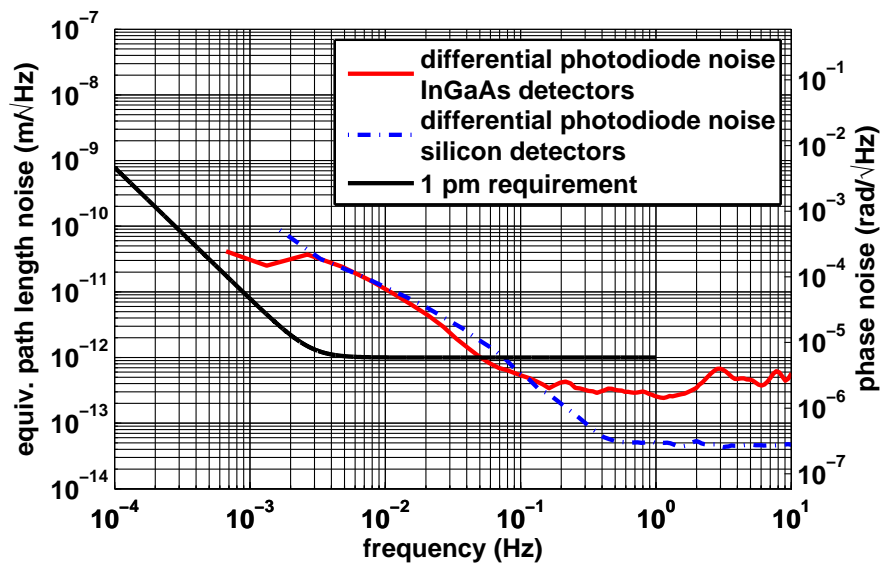


Figure 3.30.: Comparison of differential photo diode noise using InGaAs photo diodes and silicon photo diodes

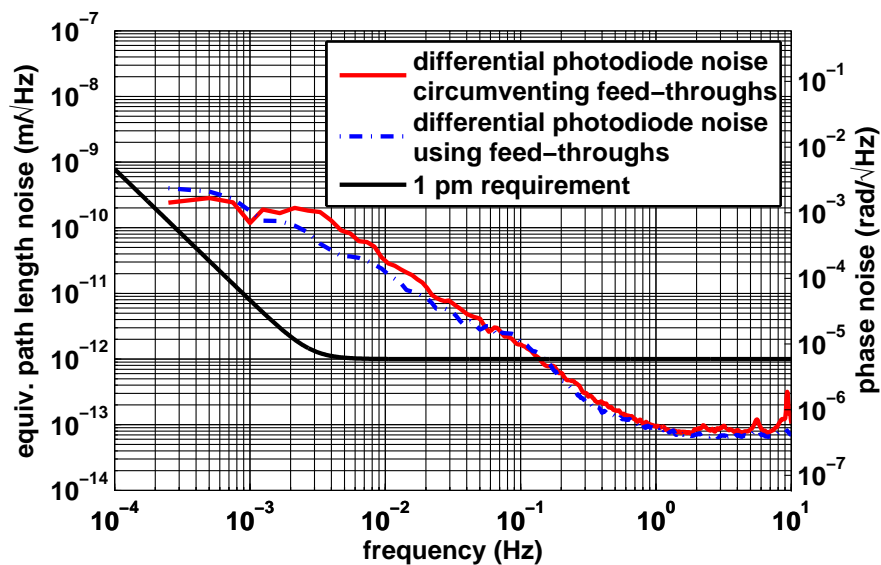


Figure 3.31.: Comparison of differential photo diode noise using vacuum feed-throughs versus the noise encountered when circumventing the feed-throughs.

#### 3.4.4. Polarizers in front of photo diodes

Another source of differential photo diode noise might be a spurious interferometer present in the light that is not in the nominal s-polarization, but in the orthogonal p-polarization state. This light could stem from imperfect polarization-maintaining properties of the fibers or it might be introduced through scattering processes.

Polarization filters were added in front of the photo diodes in order to reject the light from this spurious interferometer. Polarcor<sup>®</sup> filters with an extinction ratio of up to  $10^6$  were used to enable high rejection of unwanted signals. The measurements with these filters installed were compared to previous measurements without polarization filters.

The resulting noise spectral densities are presented in Figure 3.32. In this figure, the dashed blue trace representing the measurement with polarizers shows higher noise than the measurement without polarizers represented by the solid red trace for frequencies above 0.2 Hz. This can be attributed to the signal loss occurring due to transmission of about 70% at 1064 nm wavelength of the polarization filters. However, the noise below 0.2 Hz is lower with the polarization filters in place. It is compatible with the 1 pm requirement in the whole frequency range of interest (0.1 mHz to 1 Hz).

From the findings presented here, one can conclude that a spurious signal must be present in the orthogonal polarization state, which can diminish the measurement quality. Fortunately, the polarizers can reduce this effect to a level which is compatible with the 1 pm requirement. Therefore, all subsequent measurements were conducted with these polarizers in place.

Concerning a possible space-based gravitational wave interferometer, this means that the issue of polarization clean up will have to be kept in mind in the design of its optical bench. Measurements of potential spurious signals should be made prior to the launch and the integration of similar polarization filters is to be considered in case similar spurious signal levels are found.

### 3.5. Reduction of external influences

Now that it was established that the phase measurement system and the photo detector were capable of measuring path length noise at the picometer level, first optical path length measurements could be started. Up to this point, only the noise of the measurement equipment (photo detectors and phase meter) had been measured. This section deals with the identification and – where possible – elimination of external influences that can compromise the sensitivity of the setup to non-reciprocal phase changes.

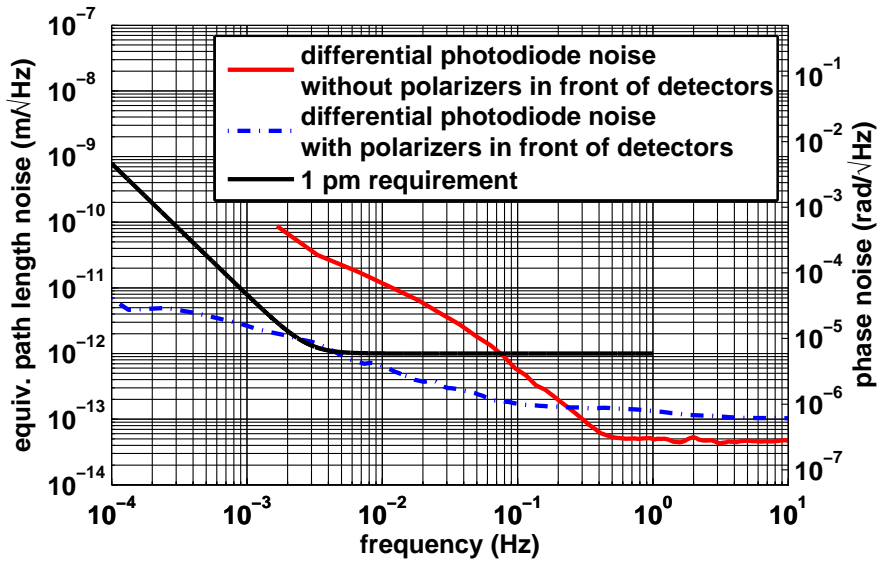


Figure 3.32.: Comparison between differential photo diode noise before and after adding polarization filters in front of the photo detectors.

### 3.5.1. Fluctuations in the refractive index of air

Air currents caused by convection or draft in the lab due to the air conditioning lead to fluctuations in the air pressure in the optical beam paths and thereby also to fluctuations in the refractive index, which will appear as path length changes in interferometric measurements.

One way to avoid this noise source is to put the experiment in a small box, such that the volume of moving air is greatly reduced and also external air currents from vents are shielded off. However, this still allows for residual currents inside the box due to convection from heated surfaces and also acoustical coupling. Pressure variations at very low frequencies are also not very well shielded by this technique, unless the box is airtight.

To completely remove noise due to refractive index variation of the air, the experiment needs to be conducted in a vacuum environment. Luckily, this is also the case in the actual LISA experiment, where the optical benches will be exposed to the vacuum of outer space.

While it is technically very challenging to achieve pressure levels below  $10^{-12}$  mbar – corresponding to less than  $10^4$  particles/ $\text{cm}^3$  – present in the interplanetary environment [48], it is usually sufficient (and also quite representative of the spoiled vacuum inside the satellites which suffers from outgassing of satellite components) to achieve pressure levels around  $10^{-4}$  to  $10^{-6}$  mBar, which are relatively easy to achieve using turbo-molecular pumps.

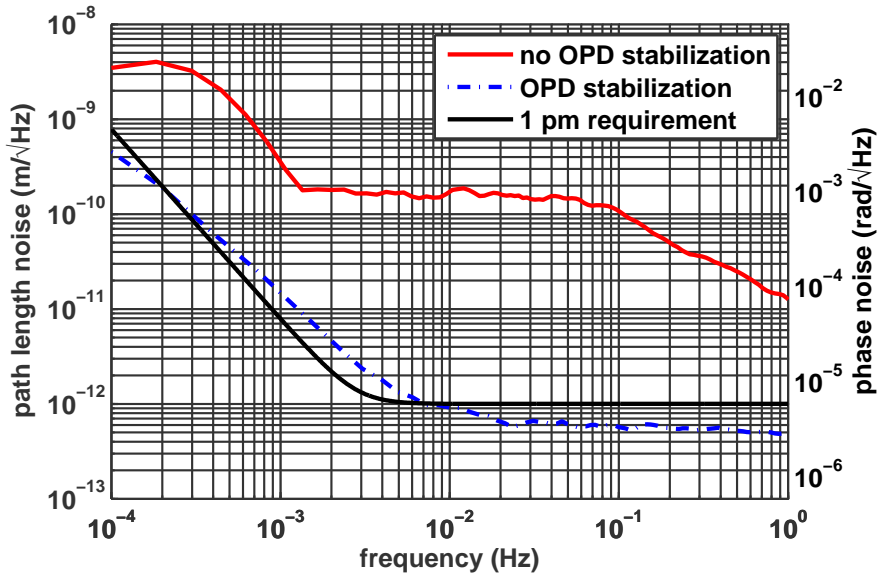


Figure 3.33.: Comparison between non-reciprocal noise observed with active optical path length difference (OPD) stabilization and without.

### 3.5.2. Optical path length difference OPD stabilization

Previous experiments using the LTP-derived modulation bench and the PM3-type hardware phase meter have identified a non-linearity in the measurement process arising from interfering electronic signals [49]. This could be overcome through stabilization of the differential path length changes of the vacuum feed-through fibers bringing the light to the experiment.

The same effect would also inhibit measurements in this experiment, because the path length difference between the two beams generated on the modulation bench is not stabilized. While this difference normally should not cause any problems because it is common to all measurement signals and cancels in the subtraction of the reference interferometer's phase, it still poses a problem in this experiment due to the non-linearity of the phase measurement system. Measurements in the different interferometers no longer show exactly the same common phase shift, but depend on the phase measured in each interferometer.

Measurements of the non-reciprocity – in fact any interferometric length measurements using this phase measurement system – without active stabilization of the differential path length consequently show a typical shoulder-shaped noise curve. Figure 3.33 shows an example of such a noise curve observed in the measurement of the non-reciprocity of the setup. The trace without stabilization shows a noise level of about  $200 \text{ pm}/\sqrt{\text{Hz}}$  between 1 mHz and 0.1 Hz, rolling off with  $1/f$  toward higher frequencies. The white noise level between 1 mHz and 0.1 Hz is caused by the non-linearity of the phase meter, leading to a peak-to-peak phase variation corresponding to 200 pm, which is spread about a wide frequency range.

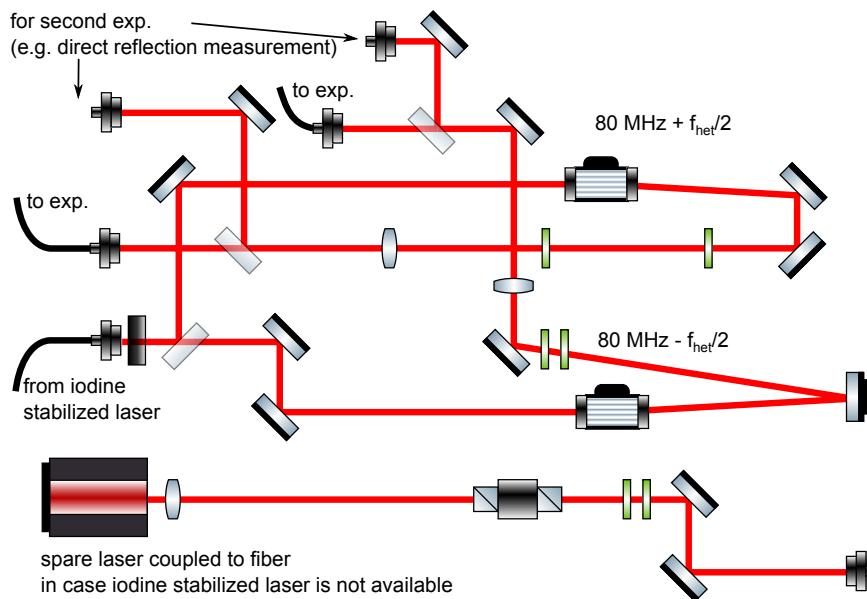


Figure 3.34.: Full schematic of the actual modulation bench.

To overcome this problem, optical path length difference (OPD) stabilization was integrated into the modulation bench, following a similar procedure that was successfully used in LTP. One beam was reflected by a piezo mounted mirror which was driven by a feedback circuit stabilizing the phase in the reference interferometer to an electronic reference phase generated by the offset-locking electronics used to drive the AOMs.

The complete modulation bench is shown in Figure 3.34. Light was brought in from an Iodine stabilized laser light source through a fiber to a fiber coupling assembly on the lower left hand side of the figure. This light is first attenuated and slightly focused by a 500 mm focal length lens and then split into two parts of equal power by a power beam splitter. Each of the two resulting beams passes through an AOM, driven by electronic signals with a frequency of  $80 \text{ MHz} \pm f_{\text{het}}/2$ . This results in corresponding frequency shifts in the first order diffracted output beams. One of the beams is reflected under a near-normal angle of incidence ( $\approx 5^\circ$ ) by a piezo mounted mirror which allows to actuate the differential path length of the two beams by applying a voltage to the piezo.

Finally, both beams pass through half- and quarter-wave plates, as well as a re-collimating lens of 500 mm focal length, before each is coupled into the vacuum feed-through fibers to be sent to the optical bench inside the vacuum chamber hosting the experiment.

### 3.5.3. Laser intensity stabilization

Another factor that could potentially impact phase measurements and thereby the observed non-reciprocal noise in the experiment is the laser power noise. One

potential coupling mechanism of low frequency intensity variations is a change of photo diode capacitance with temperature, which is in turn influenced by the absorbed light power. Intensity fluctuations near the heterodyne frequency are treated in Section 3.5.4 below.

To assess the influence of this potential noise source measurements were performed while the light power was modulated using the amplitude modulation input of the AOM drivers. These inputs allow one to easily change the amplitude of the RF-signal driving the AOMs. This will lead to a change in the light power in the first order diffracted beam output due to the change in diffraction efficiency at different RF-signal levels.

Using the amplitude coupling coefficient obtained in these measurements, it was possible to measure the direct current (DC) amplitude fluctuations and make a projection of their influence on the non-reciprocal noise. The measured DC amplitude's noise was calculated and multiplied with the known coupling factor to obtain the resulting non-reciprocal noise from amplitude fluctuations.

The results of this noise projection can be found in Figure 3.35. Measurements with and without active amplitude stabilization are compared. As can be seen from the figure, without active amplitude stabilization, the observed non-reciprocal noise is higher in the whole frequency range. The noise shape is very similar to  $1/f$ , starting out at about 100 pm at a frequency of 1 mHz and diminishing toward higher frequencies. The relative amplitude noise without active stabilization, shown in red and dashed, is at about  $10^{-2}$  for frequencies 2 mHz and 0.1 Hz. The resulting projected non-reciprocal noise is very close to the observed non-reciprocal noise at a frequency of 0.1 Hz. With active amplitude stabilization, the amplitude noise, shown dashed and in blue, is reduced by about a factor of 100 in the frequency range between 2 mHz and 0.1 Hz. The solid blue trace, representing the corresponding observed non-reciprocal noise is very close to the 1 pm requirement, plotted in black.

Therefore, one can see that observed non-reciprocal noise is greatly reduced when active laser amplitude stabilization is employed. A relative amplitude stability of better than  $10^{-3}$  is required given the amplitude coupling factor found here to allow the measurement of non-reciprocal path length noise at a level compatible with the 1 pm requirement.

To overcome the influence of the changes in laser intensity, an electronic intensity stabilization circuit was used. This circuit was already available from other LISA Pathfinder related experiments conducted at the AEI. It uses the photo current of a photo diode as input, which is passed through a trans-impedance amplifier to convert it into a proportional voltage. The resulting signal is then compared to a 10 V voltage obtained from an AD587 voltage reference and the difference serves as input signal for a feedback loop, consisting of two integrators and a proportional amplifier.

Figure 3.36 shows the closed loop gain of the amplitude stabilization circuitry, wherein the intersection of the amplitude trace with the 0 dB line shows that the

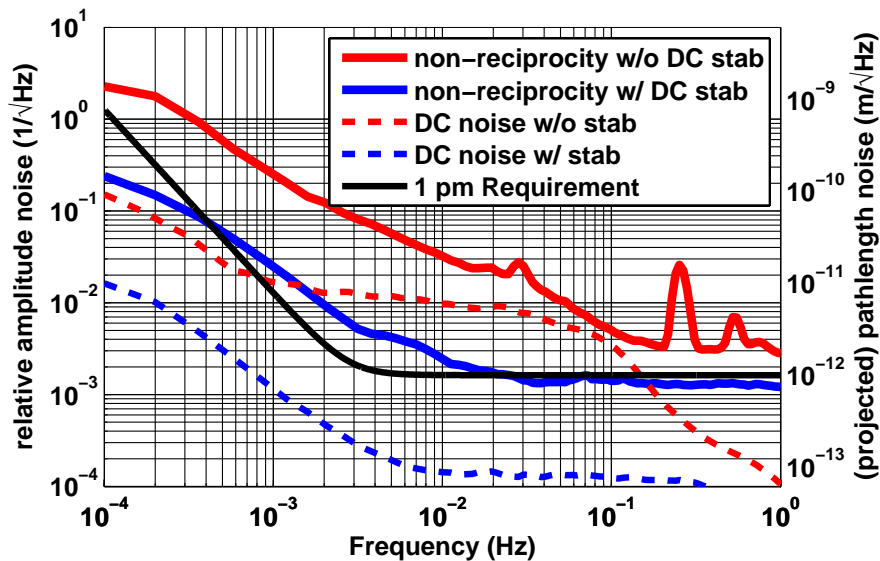


Figure 3.35.: Comparison between non-reciprocity observed with active laser amplitude stabilization and without.

unity gain frequency achieved using this circuit was around 22 Hz, i.e. amplitude fluctuations occurring below 22 Hz are suppressed by applying this stabilization.

### 3.5.4. Amplitude stabilization at the heterodyne frequency

In addition to the changes in laser intensity leading to changes in the observed phase, changes of the laser intensity at the heterodyne beat note's frequency will also be measured by the phase meter as if they were a spurious beat signal. In order to avoid this effect, a second amplitude stabilization circuit was built using an electrical circuit similar to the one described in the previous section to stabilize the DC amplitude fluctuations, with an additional band pass filter for the heterodyne frequency installed in its feedback signal instead of the low pass previously found to avoid oscillations at high frequencies. This way, only amplitude fluctuations in a small frequency band around the heterodyne frequency were suppressed.

The input signal for this amplitude stabilization circuit was taken from additional photo detectors integrated into the modulation bench, which sensed a part of the light beam that was fed into the vacuum feed through fibers. Glass wedges were introduced directly in front of the fiber couplers which reflected approximately 4 % of the incoming light power onto these additional detectors.

Two individual amplitude stabilization circuits were used, one per beam being transmitted to the vacuum chamber. Each feedback signal was connected to the amplitude modulation input of the respective AOM, which allows to modulate the intensity in each beam separately by changing the AOMs driving voltage amplitude and thereby its diffraction efficiency.

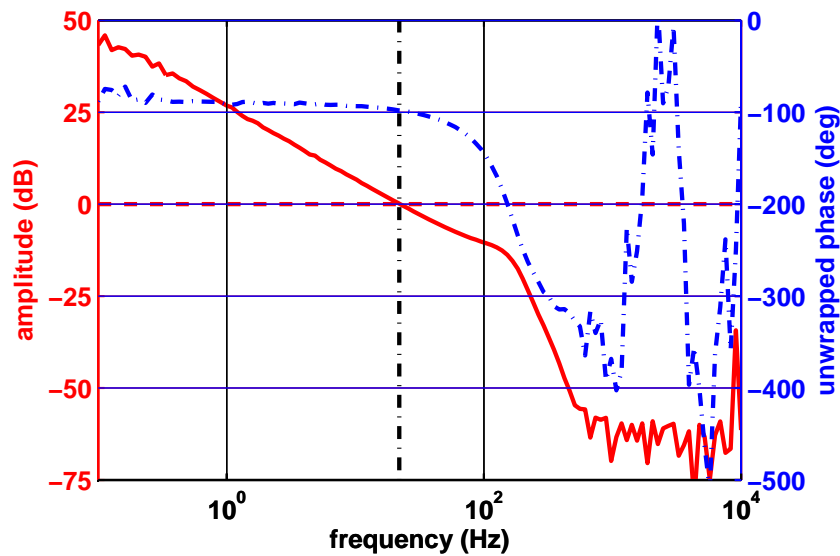


Figure 3.36.: Measured closed loop transfer function of the amplitude stabilization circuit

Applying this additional stabilization technique led to a reduction of observed laser intensity noise at the heterodyne frequency. However, no accompanying reduction in the non-reciprocal noise was found. This led to the conclusion, that the laser intensity fluctuations at the heterodyne frequency did not result in excess non-reciprocal phase noise at the picometer level.

### Straylight signal suppression using amplitude modulation

The same electronic circuit described above that was used to suppress fluctuations of the laser intensity at the heterodyne signal's frequency can also be applied to the signals measured inside the vacuum chamber. In this case, the intensity fluctuation at the heterodyne signal's frequency is caused mostly by light reflected from the fiber coupler generating spurious beat signals. With the band pass filtered amplitude stabilization discussed above, these fluctuations can be canceled, effectively suppressing the stray light signal.

This was confirmed in the experiment. Photo diodes in the vacuum chamber directly after the fiber (highlighted in Figure 3.37) were used as input to the laser intensity noise stabilization circuit at the heterodyne frequency. In the absence of stray light no beat note should be detectable at this point, and therefore also no additional laser intensity fluctuation at the heterodyne frequency. Half the light coming out of the fiber under test is observed, being reflected by the beam splitters originally introduced to facilitate a null-measurement. Spurious light reflected by the fiber can lead to a beat note which will be picked up by the photo detectors as an intensity fluctuation at the heterodyne frequency.



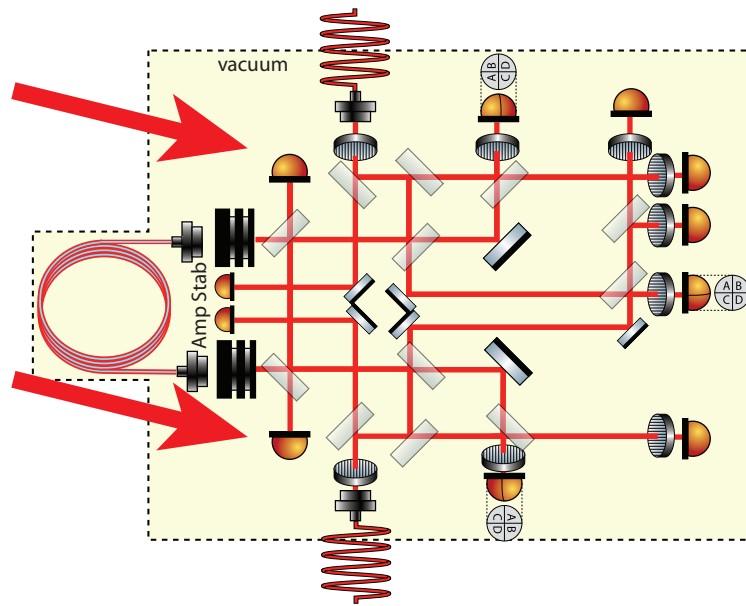


Figure 3.37.: Schematic showing the placement of additional photo detectors for measurement of amplitude fluctuations at the heterodyne frequency for the measurement and suppression of these unwanted signals.

The non-reciprocal noise observed in these measurements is shown in Figure 3.38. The non-reciprocal noise traces shown in red for the quadrant photo detectors and in dashed green for the single element detectors are much lower than in previous measurements. Additionally, it is apparent that the stray light subtraction described in Section 3.6.1 is no longer very effective and only leads to a minute reduction in noise amplitude, as can be seen comparing the dash dotted blue trace, representing noise observed with this additional noise subtraction to the other two traces. This can be attributed to the fact that the stray light is already largely canceled by the stabilization circuit feeding back the observed spurious signal to the amplitude modulators.

### 3.5.5. Reduction of thermal fluctuations

The room temperature in a laboratory is usually quite noisy in the very low frequency range, i.e. below about 0.1 Hz. The daily temperature variations due to the change between night and day can never be fully shielded from the laboratory environment, unless one is to move the experiment to an underground facility or one builds an actively temperature stabilized outer enclosure. As this was not easily possible for the non-reciprocity experiment, an alternative approach was sought where the influence of temperature variations on the experiment was minimized.

This was accomplished through the use of Zerodur™ as a base plate material for the core experimental setup. Zerodur™ is a glass ceramic manufactured by Schott, which is designed with a coefficient of thermal expansion (CTE) at room

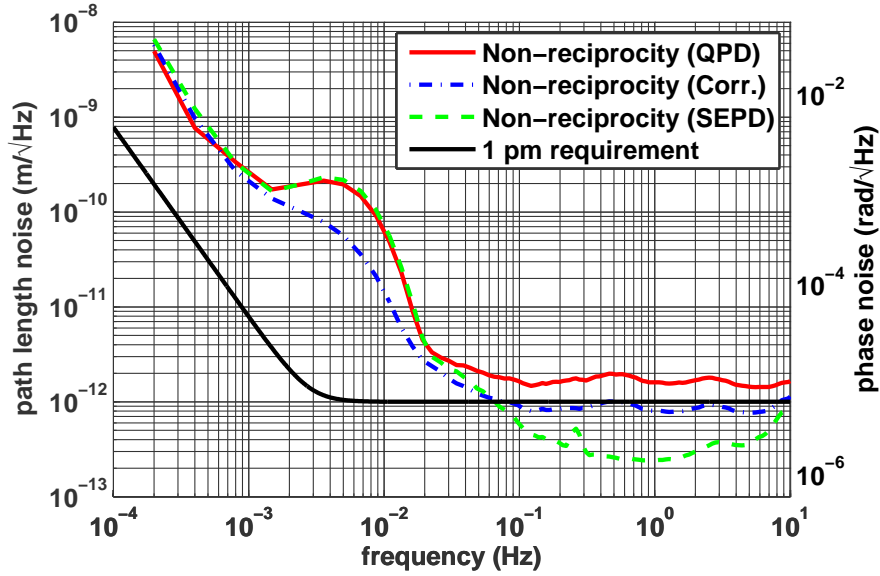


Figure 3.38.: Example of direct stray light subtraction by using an amplitude stabilization circuit at the heterodyne frequency and photo diodes that sense exclusively the stray light signal.

temperature as close to zero as possible. Typically, values for the CTE of less than  $0.1 \times 10^{-6}$  are achieved, with specially selected parts available with a CTE of less than  $0.02 \times 10^{-6}$ .

While these values are exceptionally low, they are still too high for a typically sized experiment to achieve picometer length stability under normal laboratory temperature noise conditions. Temperature fluctuations of about  $1 \text{ K}/\sqrt{\text{Hz}}$ , typically found at frequencies of  $0.1 \text{ mHz}$  would still lead to length changes of  $0.02 \times 10^{-6} \times 0.2 \text{ m} = 4 \times 10^{-9} \text{ m}/\sqrt{\text{Hz}}$ , about three orders of magnitude higher than the requirements.

It was thus necessary to reduce the temperature noise at the core part of the experiment. While the vacuum chamber in which the experiment was conducted provided reasonable passive temperature stabilization through its large thermal mass and the reduction of convective heat transport in the vacuum environment, this could still be improved upon by installing a passive thermal shield inside the vacuum chamber.

Figure 3.39 shows a schematic of the thermal shield used in the experiments. It is basically a box made out of aluminum sheet metal. It works by reflecting the thermal radiation, which is the dominant remaining heat transfer mechanism in the vacuum environment. This in turn increases the time required for external temperature variations to influence the experiment inside the thermal shield. Spacers made from Macor, a ceramic material with low thermal conductivity, and Viton

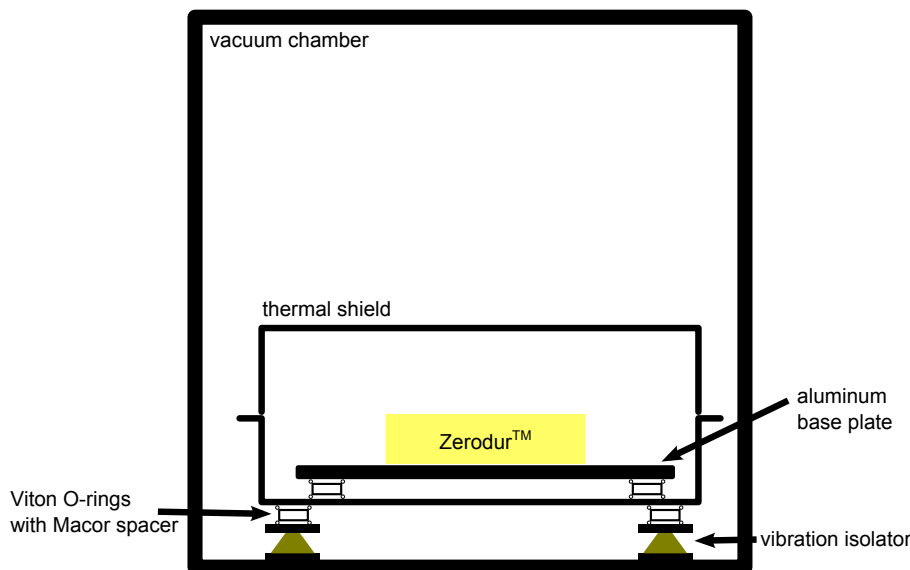


Figure 3.39.: Schematic of the thermal shield used to attenuate temperature fluctuations in the experiment.

O-rings ensure that the conductive heat transfer is minimized and that vibrations are reduced.

The effectiveness of the thermal shield was confirmed by temperature measurements within it and on the inside of the vacuum chamber. Using temperature sensors on the inside of the vacuum chamber and on top of the Zerodur™ optical bench inside the thermal shield, it was possible to calculate the thermal transfer function of the shield. This was accomplished by dividing the spectrum of the temperature recorded on the optical bench by the spectrum of temperature recorded outside the thermal shield.

The result of this transfer function measurement is shown in Figure 3.40. One can see that the thermal shield behaves like a passive, first-order low pass filter. Temperature fluctuations at frequencies below 0.1 mHz can pass almost unhindered, while a  $1/f$  behavior is observed at frequencies higher than 0.1 mHz. Above a frequency of about 0.7 mHz the signal becomes lost in the sensor noise due to the already very good thermal isolation of the vacuum chamber, as is evident by the erratic behavior of the transfer-function's phase.

Due to the very good temperature isolation performance achieved using this simple shield, it was kept in place for all further measurements.

### 3.5.6. Vibration reduction

Conducting the measurement in an evacuated vacuum chamber leads to the need for vacuum pumps. In this case, a combination of a scroll pump for the rough vacuum and a turbo-molecular pump to achieve pressure levels down to the

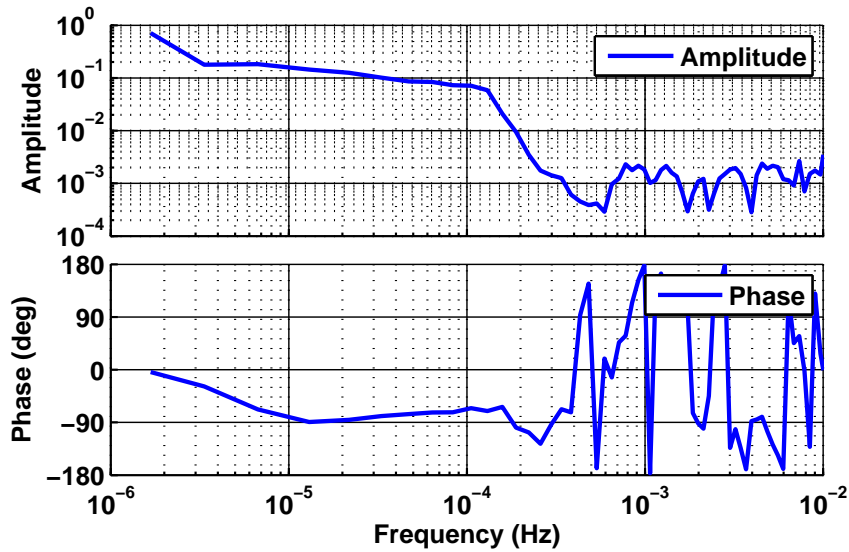


Figure 3.40.: Transfer function of the thermal shield used in all experiments

$10^{-6}$  mbar level was used. While it was always attempted to take data after the pumps had been switched off, this was not possible for extended periods of time in the case of the turbo-molecular pump, as the pressure would not remain constant after it had been switched off; probably due to leaks and outgassing.

Still, some measurements were taken with the turbo-molecular pump switched off, despite the fact that the pressure levels achieved were much higher (approximately 0.1 mbar). When comparing these to measurements taken when the turbo-molecular pump was switched on, it became apparent that a white noise floor at about  $0.1 \text{ mrad}/\sqrt{\text{Hz}}$ , corresponding to non-reciprocal length changes of  $100 \text{ pm}/\sqrt{\text{Hz}}$ , was present in the measurements with the pump switched on.

It was speculated that this might be due to the vibrations introduced by the pump, which rotates at a high frequency (966 Hz) and is rigidly connected to the side wall of the vacuum chamber. To mitigate the effect of these vibrations on the experiment, passive, vacuum compatible dampers were installed under the thermal shield. Dampers of NewDamp™ ND-50 type by Newport corporation were used, because they fit the size requirements and provided sufficient passive vibration isolation in the horizontal and vertical direction for excitation frequencies above 10 Hz. Figure 3.41 shows a photograph of one of these dampers with a 2 Euro coin on top of it for size comparison.

Furthermore, it was found that the nominal turbo pump's rotational frequency coincided with a resonance of the vacuum chamber. This led to resonant amplification of the vibrations introduced by the pump and thereby had a significant impact on the observed phase noise. Reduction of the turbo pump speed from 966/s to 630/s led to much lower vibrations, removing the white noise at  $100 \text{ pm}/\sqrt{\text{Hz}}$

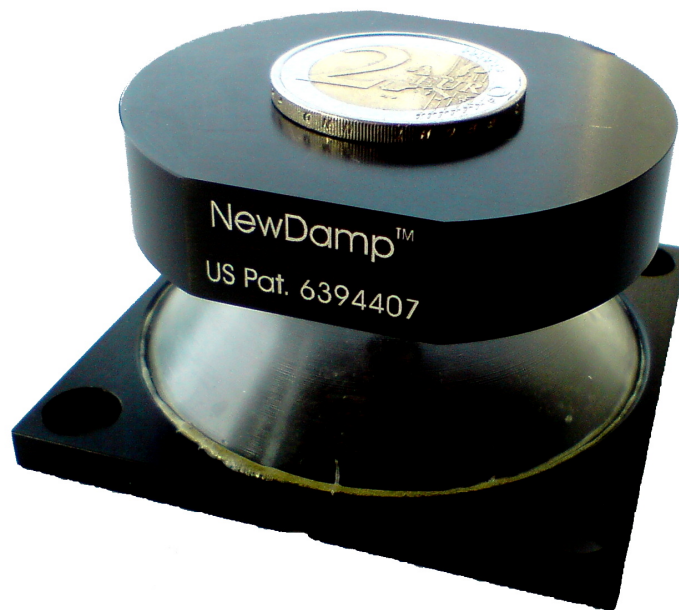


Figure 3.41.: Photo of passive, vacuum compatible vibration damper used in the experiment to reduce vibrations

previously observed when the pump was running without compromising the attainable pressure levels.

### 3.5.7. Laser frequency noise

In a Mach-Zehnder interferometer with unequal arm length, laser frequency noise fluctuations lead to phase fluctuations in the interference signal. The relationship between frequency noise and phase noise is as follows [31]:

$$\frac{\delta\varphi}{\delta f} = \frac{2\pi\Delta L}{c}$$

Here,  $\delta\varphi$  stands for the phase induced by the frequency noise,  $\delta f$ . The arm length difference is denoted by  $\Delta L$ , and  $c$  is the speed of light.

In order to find the frequency noise coupling coefficient in the experiment, we switched off the frequency stabilization of the laser and measured the length noise of the fiber. After computing the spectral density of this length noise, we found a much higher length noise, that followed a  $1/f$  shape as shown in the red trace in Figure 3.42. From the fact that the observed length noise increased after switching off the frequency stabilization it can be deduced that noise levels without laser frequency stabilization are dominated by this noise source.

This, in turn, allows one to compute the coupling factor between the known laser frequency noise without active stabilization of  $10 \text{ kHz}/f$  and the observed

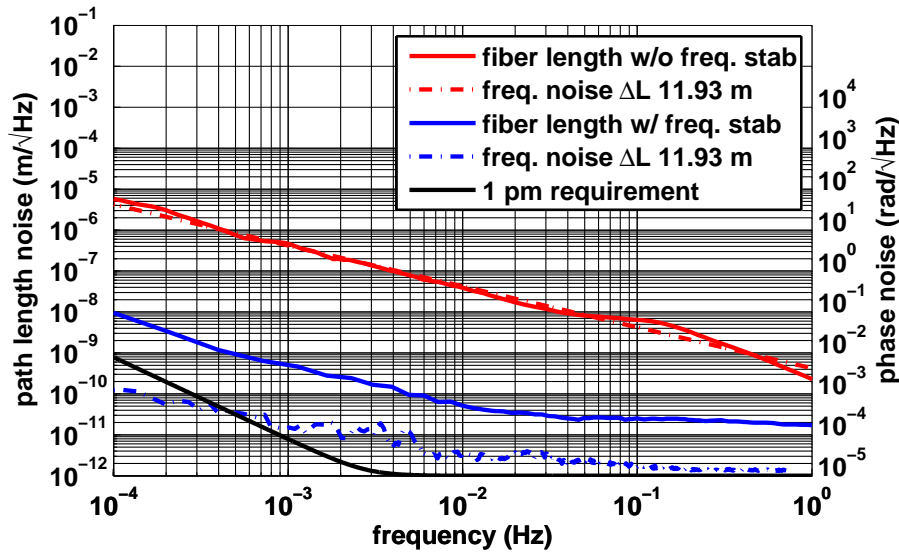


Figure 3.42.: Laser frequency noise coupling factor measurement for fiber length measurement.

path length noise. In this case, this yielded a coupling factor of  $0.25 \mu\text{rad}/\text{Hz}$ , corresponding to a length mismatch in the arms of about 12 m. This is in good agreement with the *optical* length of the fiber plus the additional path length mismatches on the optical bench present in each individual interferometer.

After repeating the measurement with frequency stabilization enabled, a much lower length noise was found, as indicated by the blue trace in Figure 3.42. Using the frequency noise of the stabilized laser – known from measurements performed by Dr. Michael Tröbs, who kindly provided the measurement data – it was also possible to predict the frequency noise induced non-reciprocal path length noise. This is represented by the dashed blue trace in the figure. Because this trace is significantly below the solid blue trace, it can be concluded that the length measurement noise is no longer dominated by frequency noise induced fluctuations when active laser frequency stabilization is employed.

The same analysis was also repeated for the non-reciprocity signal combination. Again, the red trace in Figure 3.43 represents the non-reciprocal noise observed when the laser's frequency stabilization is switched off. In the combination of interferometer signals that yields the non-reciprocal length, the path length difference in the two measurement interferometers cancels to a large extent, and a much smaller observed frequency coupling coefficient of only approximately  $0.5 \text{ nrad}/\text{Hz}$  results, displayed in the dashed red trace. This corresponds to an effective arm length difference of only approximately 25 mm.

The blue trace in Figure 3.43 shows the observed non-reciprocal noise when the laser frequency stabilization is active. Again, the dashed blue trace shows the projected laser frequency noise for comparison. Here, from the fact that this trace

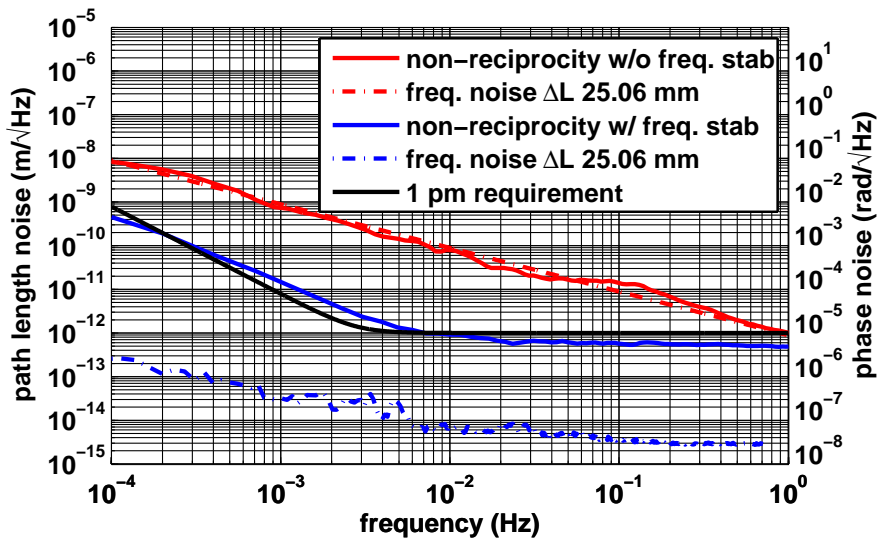


Figure 3.43.: Laser frequency noise coupling factor for non-reciprocity measurement.

is significantly below the observed non-reciprocal noise, it can also be concluded that it is no longer dominated by frequency noise induced phase fluctuations, when active laser frequency stabilization is used. However, this also means that an active frequency noise stabilization is required in order to achieve sub-picometer non-reciprocal noise measurements. Therefore, all measurements were conducted using the frequency stabilized laser.

### 3.5.8. Polarization control

Consequent to the measurements presented in Section 3.4, linear Polarcor<sup>®</sup> polarizers were added in front of all photo diodes. The photo diode mounts were upgraded during this step to accommodate the new filters. Figure 3.44 shows a photograph of these mounts. The polarization filters are located directly in front of the photo diode in a rotatable and lockable holder.

Additional polarizers were also added directly behind the fiber launchers that bring the light onto the optical bench. The Polarcor<sup>®</sup> filters could not be used in this position due to their insufficient wavefront quality. Instead, Glan-Thompson polarizers by Bernhard Halle Nachfl. GmbH were used which have a similar extinction ratio to the Polarcor<sup>®</sup> filters but better wave front quality. However, they are more bulky and therefore inadequate for use in front of all photo diodes. A schematic of the updated setup with the position of all polarizers is shown in Figure 3.45.

To further improve the polarization stability in the experiment, the input polarization state to both the input fibers and the fiber under test was matched to the





Figure 3.44.: Photograph of a newly designed photo detector mount with polarization filter in front of the photo diode

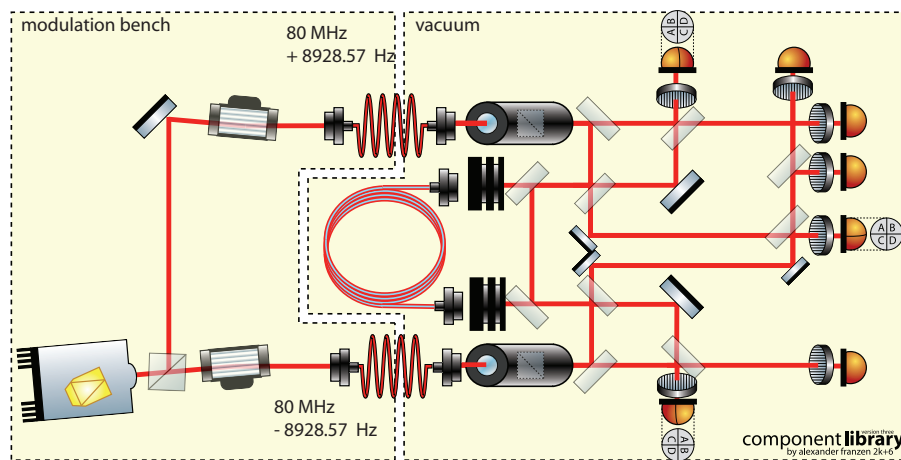


Figure 3.45.: Schematic of setup showing positions of all polarizers in use

polarization-maintaining axes. The polarization-maintaining fibers that were used in the experiment are of the PANDA-type [50]. This type of fiber features an inner core, which guides the light, and two *stress-inducing elements*, which serve to introduce stress at the fiber core in well-defined directions, which leads to stress-induced birefringence in the fiber core. This is illustrated in Figure 3.46. The difference in refractive index introduced by the stress-induced birefringence in turn makes the fiber polarization-maintaining. The larger the difference is between the refractive index along the axis formed by a line through the stress inducing elements and the axis perpendicular to this, the better the polarization-maintaining properties of the fiber. The manufacturers usually do not directly give the difference in refractive indices, as this turns out to be a relatively small number (of the order of  $10^{-4}$ ), but instead they specify a beat length. This beat length corresponds to the length of fiber after which the nominal and the perpendicular polarization have a relative phase shift of  $2\pi$ .



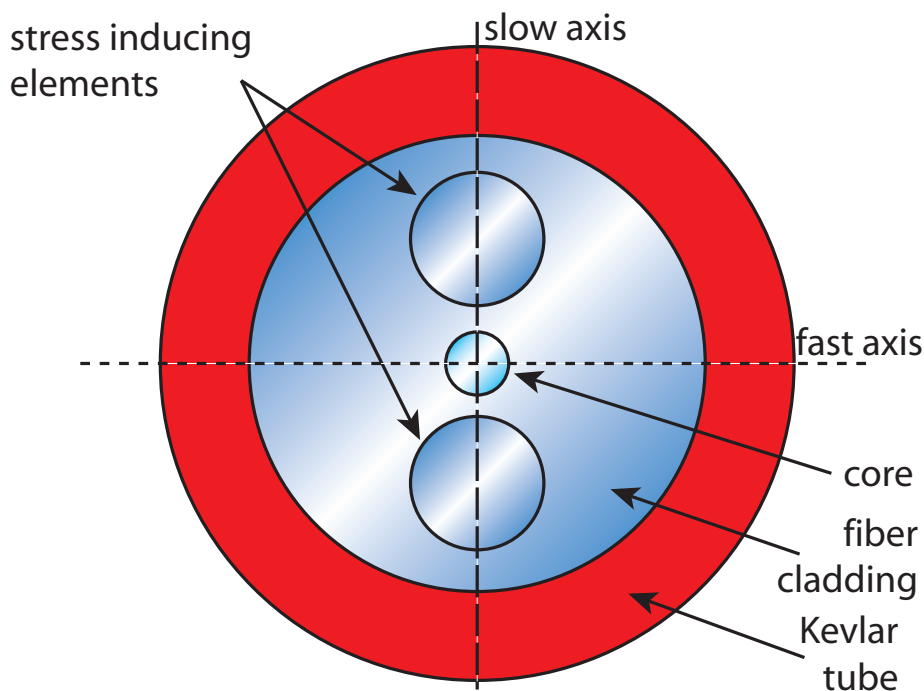


Figure 3.46.: Schematic of the internal structure of a polarization-maintaining and absorption-reducing (PANDA) type single-mode, polarization-maintaining fiber.

This beat length is on the order of meters for regular, non-polarization-maintaining fibers and can be as short as a few millimeters for polarization-maintaining fibers. Hence it is clear that a shorter beat length corresponds to a larger relative difference in refractive indices and therefore to better polarization-maintaining properties. With such a short beat length, polarization extinction ratios of 23 ... 26 dB can be achieved in typical fibers. Despite the fact that the fiber used in this experiment had a very short beat length of 1.5 to 2.7 mm [51], still great care has to be taken to match the incoming polarization to the slow axis, which is typically used because of its lower sensitivity to external influences. Only very good matching of the fiber axes allows one to reach the relatively high polarization extinction ratios (PERs) quoted above, while a polarization mismatch at the input will lead to elliptically – or in the worst case even circularly – polarized light at the fiber output, which also changes in response to external influences such as stress and temperature changes.

The alignment was conducted with the help of a polarimeter by Schäfter und Kirchhoff, as described in detail in C.1. Before this polarimeter was available, input polarization state matching was achieved by rotating the input polarization using a half-wave plate. Meanwhile, the fiber was periodically stressed (e.g. using a piezo) and the output light was sent through a polarizer before it was measured using a photo detector. The setup used for this purpose is shown in Figure 3.47. Optimal

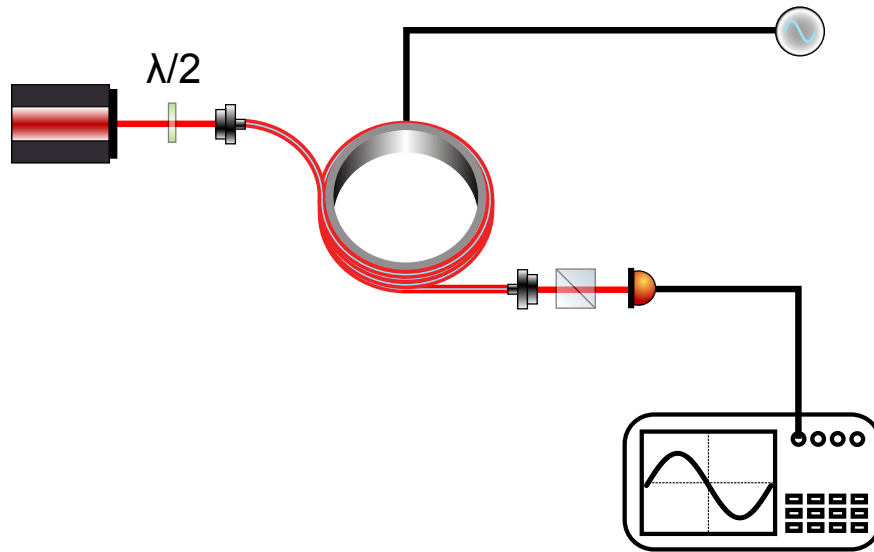


Figure 3.47.: Illustration of the method used to align the input polarization to the polarization-maintaining axis of the fiber

alignment was achieved by rotating the wave plate until the variations in the photo detector output while stressing the fiber were minimal.

### 3.5.9. Fiber length stabilization

By using a fiber wound on a cylindrical piezo as fiber under test it was possible to observe a periodic error in the non-reciprocal signal. When scanning the fiber length over several micrometers by applying a triangular voltage to the piezo on which it was wound, a sinusoidal response in the non-reciprocal length measurement was observed. This is illustrated in Figure 3.48.

Usually, it would be possible to subtract this effect in data post processing by measuring the dependence of the non-reciprocal phase on the fiber length. This was also attempted here. Several measurements were taken and the sine of the one-way phase was fit to the non-reciprocal phase. After repeating this procedure 14 times it became clear that the coefficients found using this technique were not stationary, but changed from measurement to measurement. This prevented the subtraction of this error term in data post processing.

This effect was observed previously in measurements using the PM3 phase meter [49], and is the main reason why the optical path length difference stabilization needed to be implemented, as described in Section 3.5.2.

To overcome this limitation, fiber length stabilization was implemented using a ring piezo. The fiber under test was wound around the piezo several times, enabling its length to be changed by applying an appropriate voltage to the ring piezo. An analog output signal of one of the measurement phases was used as

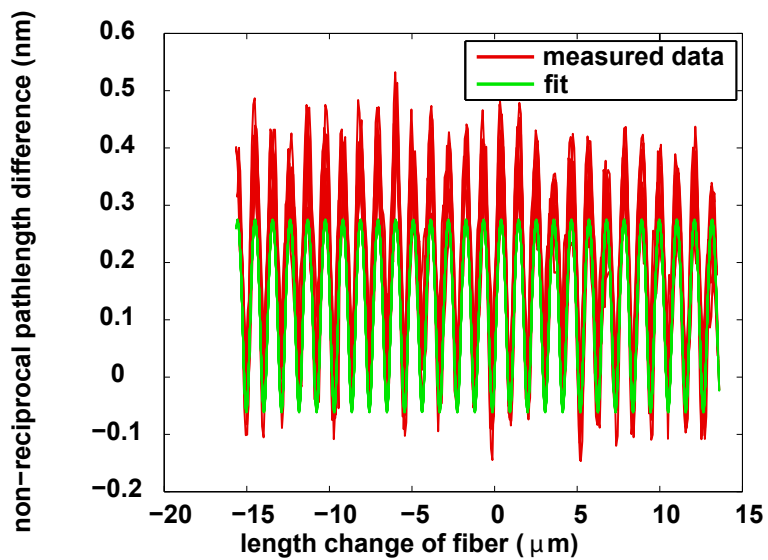


Figure 3.48.: Periodic error observed when scanning the length of the fiber under test using a piezo.

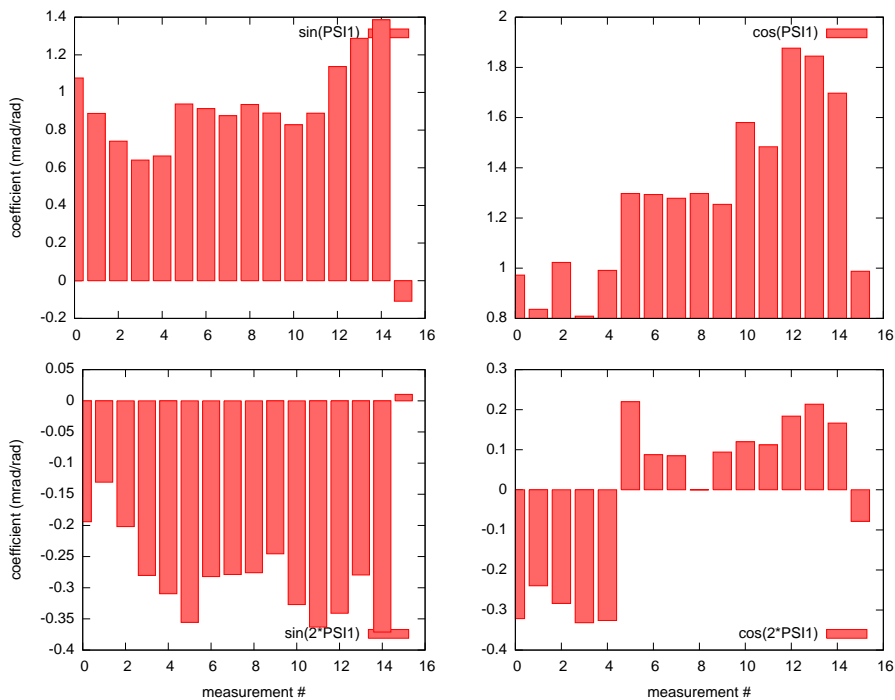


Figure 3.49.: Coupling coefficients for periodic error observed when scanning the fiber length

input to a servo loop identical to the one used in the optical path length difference stabilization, only this time feeding back to the fiber length instead of the piezo in the modulation bench. The result is a stabilized phase readout in one of the measurement interferometers. In the case of perfect reciprocity, this would also lead to a stabilized phase in the other measurement interferometer. Residual non-reciprocity is still captured in the same way as before, combining measurements from all interferometers, only with the effect of non-linearity in the phase meter removed.

The effect of fiber length stabilization on fiber length noise is shown in Figure 3.50. The solid red trace shows the noise spectral density of fiber length noise encountered in a typical measurement. The noise shape is flat at a level of about 20 picometer/ $\sqrt{\text{Hz}}$  for frequencies above 10 mHz but rises steeply proportional to  $1/f^2$  toward lower frequencies. With the fiber length stabilization enabled, as represented by the dashed blue trace, this noise level increases to 200 picometer/ $\sqrt{\text{Hz}}$  for frequencies above 2 mHz, most probably due to voltage noise of the high voltage amplifier used to generate the piezo drive voltage. Taking into account that the performance achieved with this stabilization was sufficient to reduce non-reciprocal noise levels to the picometer level and that despite this decrease in length stability at high frequencies the non-reciprocal noise in this frequency range did not increase, no effort was made to further investigate the origin of the decreased length stability at high frequencies. At low frequencies, the length noise level does not increase much further toward even lower frequencies, such that one observes a noise level of only 2 nm/ $\sqrt{\text{Hz}}$  at 0.1 mHz: much lower than the 2  $\mu\text{m}/\sqrt{\text{Hz}}$  measured without the length stabilization.

The effect on the measurement of the non-reciprocal fiber noise is illustrated in Figure 3.51. The red trace shows the non-reciprocal noise spectral density in a measurement where the fiber length stabilization was not active. While the noise is at the 1 pm/ $\sqrt{\text{Hz}}$  level for frequencies above 30 mHz, it rises like  $1/f$  for frequencies between 3 mHz and 30 mHz and a large “bump” with a peak height of 1 nm/ $\sqrt{\text{Hz}}$  is observed around 1 mHz. Comparing this to the dashed blue trace, representing the noise observed with active fiber length stabilization, one sees that the active fiber length stabilization removes the bump observed around 1 mHz and leads to an observed non-reciprocal noise level very close to the 1 pm/ $\sqrt{\text{Hz}}$  requirement represented by the solid black trace.

### 3.6. Noise subtraction in data post-processing

The techniques described in the previous section allowed to reduce the influence of external effects on the non-reciprocity of the setup, but their application alone did not yield sufficient non-reciprocal noise levels. To achieve this, a number of noise subtraction techniques that were applied in data post processing had to be implemented, which are detailed in this section.

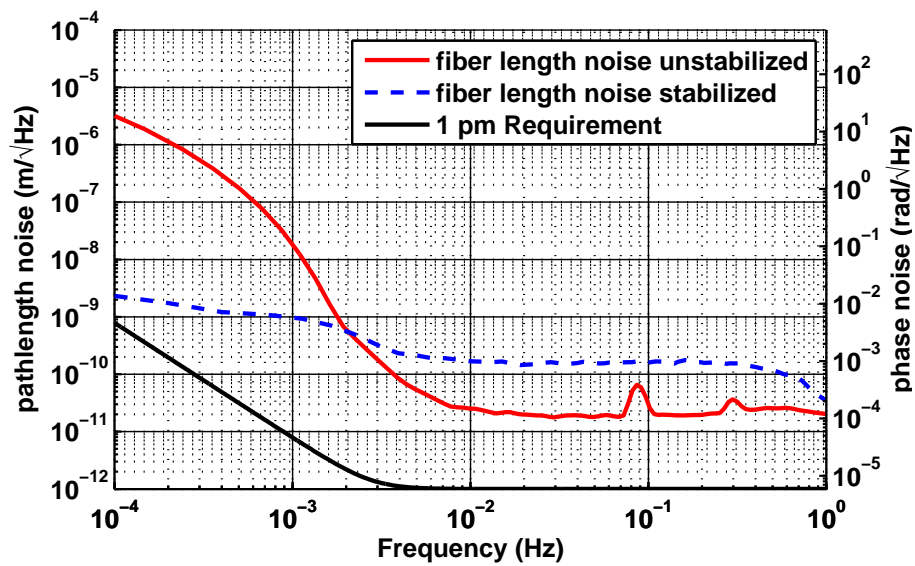


Figure 3.50.: Comparison between fiber length noise with and without active length stabilization.

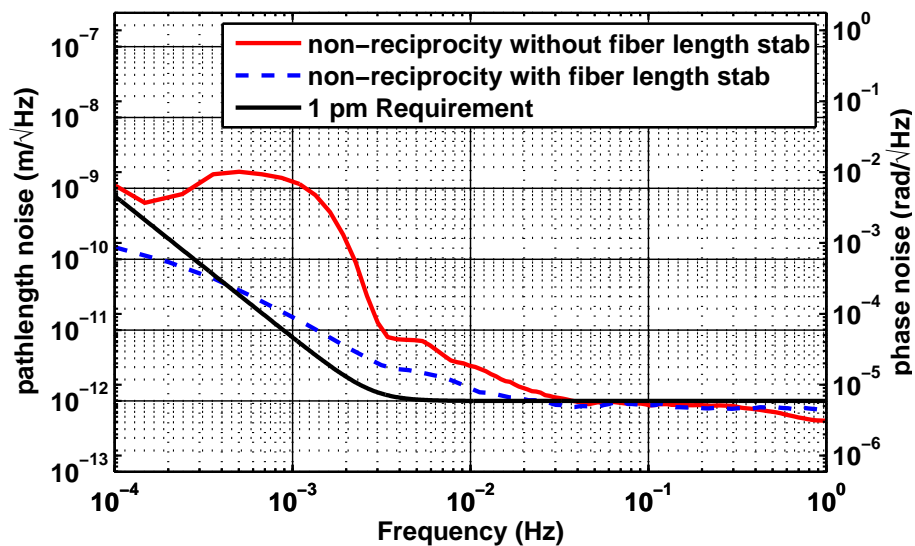


Figure 3.51.: Comparison of non-reciprocal noise observed without fiber length stabilization to noise observed with active fiber length stabilization.

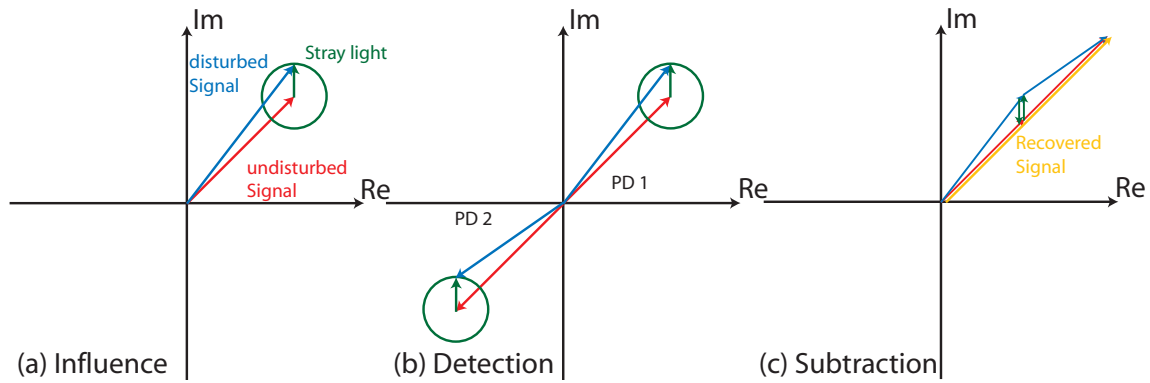


Figure 3.52.: Illustration of the principle of stray light subtraction through balanced detection

### 3.6.1. Spurious beams from fiber couplers

Fiber interfaces always lead to a small reflection. This is also a well-known problem in rotation sensing applications [52]. Here, the usual approach is to frequency modulate the light source or to use a very broad band light source with a small coherence length in order to remove these signals.

However, in this application it is not possible to change the light source or to modulate the laser frequency at will due to the limitations given by the mission design and requirements. Therefore, a different approach to deal with these reflections had to be used.

Through balanced detection [53, 34] it is possible to sense and remove spurious signals from a measurement. This is discussed in detail in the following subsections.

#### Subtraction of spurious beat note signals

Using detectors in both outputs of the recombination beam splitters makes it relatively easy to reduce the impact of stray light on the measurement by subtracting the signals of both detectors. As illustrated in Figure 3.52 this leads to a suppression of the common stray light signal and an enhancement of the differential beat note signal. Therefore, this technique was applied in post processing using data from each of the photo detectors. As this data was readily available in the form of amplitude and phase of the signals, subtraction was done by calculating the vector sum of one phase vector and the inverse of the other phase vector.

The resulting noise spectral density after this subtraction is shown in Figure 3.53, represented by the dashed blue trace, along with a noise curve obtained using only data of the quadrant photo detectors, without the application of balanced detection. It can be seen that this raw data, shown in solid red, exhibits a much higher noise level of about  $0.1 \text{ nm}/\sqrt{\text{Hz}}$ . The noise curve has a shoulder-like noise shape, dropping off steeply above approximately 1 Hz. Below about 1 mHz a  $1/f^2$  increase in noise levels is observed.

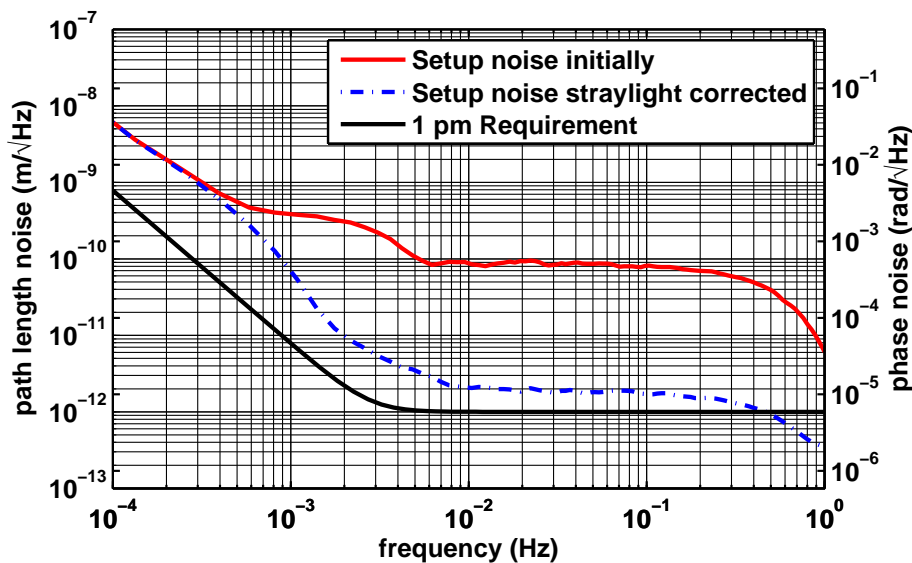


Figure 3.53.: Comparison of non-reciprocal noise levels observed in raw data and after the application of balanced detection to remove the effect of stray light.

With the introduction of balanced detection these noise levels can be vastly reduced by about two orders of magnitude. The noise after the subtraction of spurious beat note signals, shown in dashed blue, is at only 2...3 picometer/ $\sqrt{\text{Hz}}$ . The same shoulder like shape is still present, with a steep decrease in observed noise levels above 1 Hz and also a  $1/f^2$  increase below 1 mHz.

From these results it can be concluded that a lot of the apparent non-reciprocal noise is in fact due to spurious beat notes in the optical signals, which can be greatly reduced by the application of balanced detection. However, the tell-tale shoulder-like noise shape still remains present, even after the noise subtraction, possibly indicating that some portion of the spurious signal is not fully suppressed.

Therefore, further signal processing techniques were employed, as detailed in the following section.

### Normalized subtraction of spurious beat note signals

As can be seen from Figure 3.52, the stray light removal in balanced detection can only work well when the amplitudes in both detectors are matched very closely. Unfortunately this was not the case in our experiments as different detectors were used in both output ports, namely quadrant photo detectors in one port and single element photo detectors in the opposite port. This was done to reduce the number of phase meter channels required for read out.

Due to different responsivities of the different detectors and losses due to the gap in the quadrant photo detectors, the amplitudes differed by about a factor two.

This difference in amplitudes led to a greatly reduced efficiency in the stray light subtraction.

During the implementation of spurious beat note subtraction, this had to be taken into account. Beat note signals were normalized first by dividing the signal by its amplitude, thus avoiding the reduced stray light reduction otherwise expected. The results presented in 3.53 already use this normalization technique, otherwise noise levels with subtraction would be about a factor of ten higher, i.e. at 10 to 50 pm/ $\sqrt{\text{Hz}}$ .

### Direct subtraction of spurious beat notes

The subtraction of spurious beat signals described previously in Section 3.6.1 was performed using a combination of the signals sensed in both output ports of a recombination splitter using an additional photo diode per interferometer and a technique called balanced detection. This is not the only way a subtraction of unwanted signals can be performed. One alternative is to use dedicated photo diodes that ideally only sense the beat note generated by the spurious beams but not the nominal beat note.

This can be done in the experiment described here by adding photo detectors in the same places where they had previously been used in a feedback loop to suppress amplitude fluctuations at the heterodyne frequency as discussed in Section 3.5.4 and highlighted in Figure 3.37. Two diodes are added such that they sense half the light coming out of the fiber under test, being reflected by the beam splitters originally introduced to facilitate a null-measurement. In the absence of stray light no beat note should be detectable at this point. However, if light is reflected by the fiber end closest to the beam splitter or by the input fiber on the opposite side, a spurious beat note will be generated and detectable at this point.

It was also attempted to use the measurements obtained using these additional photo diodes for the subtraction of spurious beat note signals. However, these attempts failed, most probably due to the low signal amplitude and correspondingly high digitization noise in the phase meter.

To improve upon the signal to noise ratio in the direct stray light measurement channels, high pass filters with 40 dB gain and a corner frequency of about 10 Hz were installed in the respective phase meter channels. The filters were built using an active op-amp design shown in Figure 3.54.

As can be seen in the figure, a multiple feedback topology was used, because it lends itself to a high gain design and results in second order high pass behavior using a single active op-amp stage.

The transfer function of these filters was simulated using LISI (a software package for *L*inear Simulation and *O*ptimization of analog electronic circuits by Gerhard Heinzl, [54]). After the finalization of the electronics their transfer function was also measured and the result was compared to the simulations. The measured transfer function matches the simulated one reasonably well, except for a slightly lower gain. This can be explained by the dependance of the gain on the capacitor



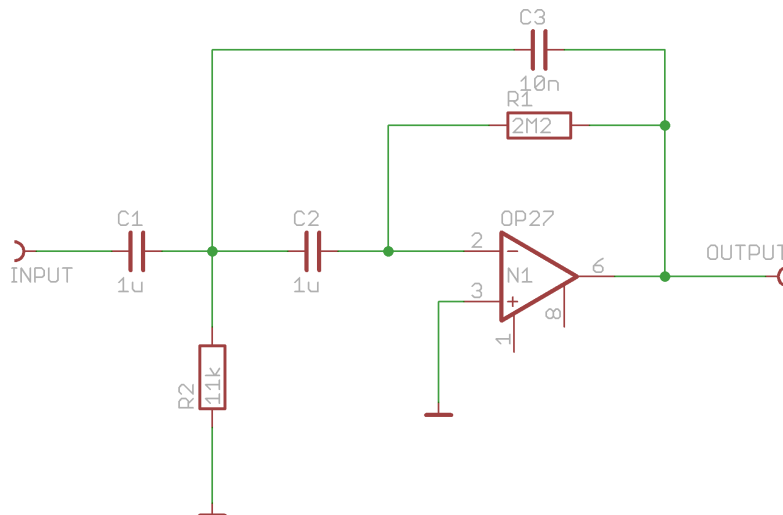


Figure 3.54.: Schematic of the electronics used to high pass filter and amplify the weak stray light signal for phase meter processing.

values which do not have very tight tolerances, but the gain variation is not harmful in this application, as only the phase of the amplified signal is measured. Figure 3.55 shows a comparison of simulation and data.

What could be shown was that the direct stray light signals match the shape of stray light signals obtained through the balanced detection scheme. This is illustrated in Figure 3.56. It shows the time series of the  $x$ -component of the calculated stray light signal phase vector compared to the  $x$ -component of the phase of the directly measured stray light signal. While the amplitudes are largely different due to the different light intensities encountered in both measurement points, the general shape of the curves is similar. The same is true for the  $y$ -component of the phase vectors and also for photo diodes in the other measurement interferometer whose time series are omitted here for brevity.

However, it was not possible to use these signals in a subtraction scheme. This is probably due to the lower signal to noise ratio found even after amplification and it should be possible to improve upon this using a more carefully designed detection scheme. This was not pursued any further because the balanced detection scheme had already proven to be working with the desired performance.

### 3.6.2. Beam pointing fluctuations

As discussed earlier (c.f. Section 3.2.2), the fiber couplers used in this experiment are not representative of those to be used in a space mission, but instead COTS components were used to facilitate the proper alignment of all fiber couplers with respect to the bonded optics on the Zerodur™ base plate. Therefore, it can be

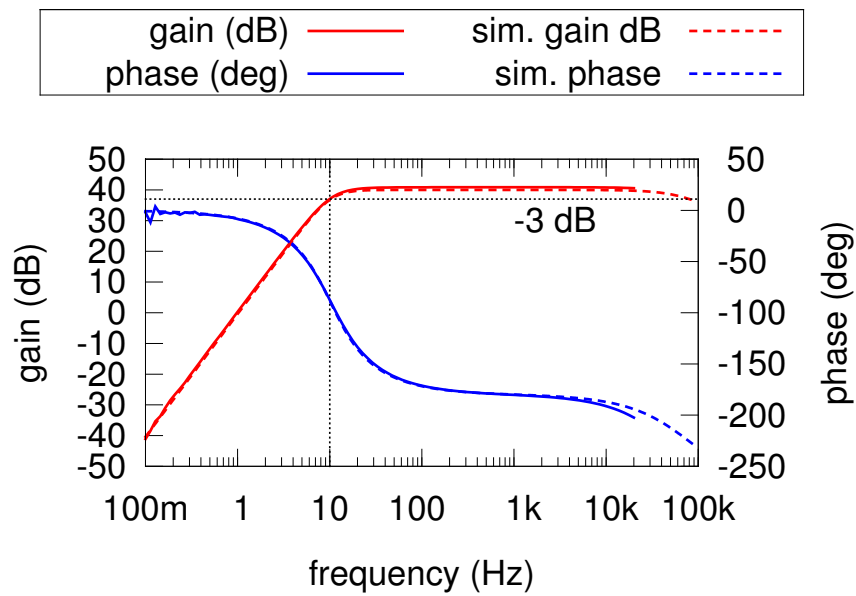


Figure 3.55.: Comparison of the measured and the simulated transfer function of the 10 Hz high pass filter implemented in some phase meter channels to amplify the weak stray light signals.

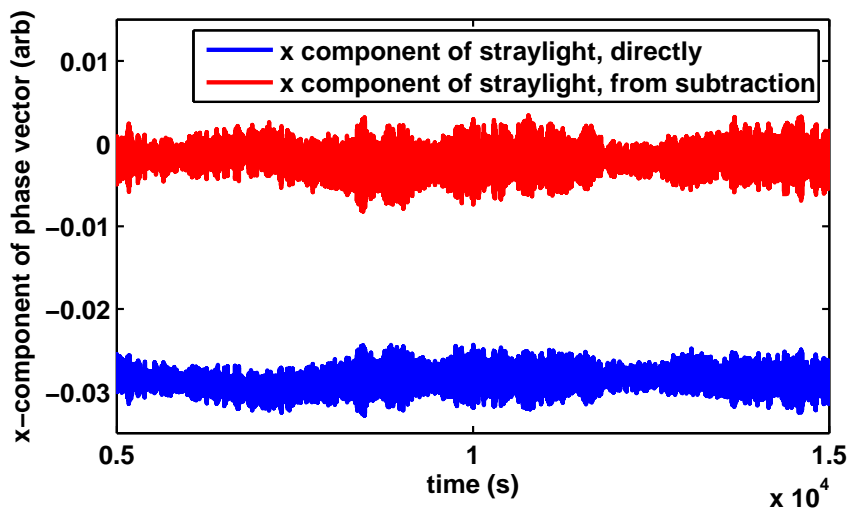


Figure 3.56.: Comparison between the directly observed stray light and the signal recovered from balanced detection. Only the x-component of the normalized phase vector is shown for clarity.

expected that the pointing stability will be compromised. While this is not generally of concern with the relatively large photo detectors used in the experiment, a potential coupling of the beam pointing to the observed phase on the detector has to be considered and taken into account. Ideally, the phase is independent of the beam's angle with respect to the detector, as long as no fraction of the beam leaves the detector and is no longer properly observed and the wave fronts are perfectly symmetrical. However, perturbations of the wave front are to be expected, and even with perfectly symmetrical wave fronts phase is only independent of the angle of incidence for infinitely large single element photo diodes. With the quadrant detectors used here, a coupling exists due to different parts of the beam impinging on the slits and being lost for the measurement process.

Additionally, imperfections in the detectors, such as defects or non-uniform response over the area of the detector, may present another source of coupling between the angle between the detector's surface normal and the beam impinging onto it and the observed phase.

To be able to quantify such couplings and sequentially subtract their influence, it is first necessary to find a means of measuring the angle of incidence onto the detector. Then, a relationship between the signal retrieved and the actual beam angle has to be established. Fortunately, measurement and calibration are both easily possible using the quadrant detectors present in the setup, as is described in detail in the following subsection.

### Calibration of differential wave front sensing signals

Using the technique of differential wave front sensing [55] it is possible to very accurately measure even tiny changes in the relative angle of two beams. This technique was therefore implemented to measure the beam pointing jitter to identify its influence and remove it.

As stated above, only the *relative* angle between the two impinging beams can be measured. The magnification factor between the actual angle and the phase response in the DWS signal depends on many parameters, such as radius of curvature of the beams wavefronts, distance traveled from source to detector and interferometric contrast / alignment quality, which are all not easily measurable.

To avoid the need to measure all these parameters to high precision (which would be necessary in order to accurately calculate the expected coupling factor between actual beam angle and DWS signal), a different approach was taken, where well defined beam angles were introduced and the resulting response in the DWS signal was recorded. With this data at hand, it was possible to calculate a calibration factor that gives the amount of DWS signal phase change per degree or per radian beam angle change, thus allowing the DWS measurements to be related to the actual beam pointing jitter. The coupling factor between the DWS signal and the actual tilt angle is usually quite large (between 1000 and 10000  $rad_{DWS}/rad_{beam}$ ), which is one of the reasons this technique is so well suited to the measurement of small angular deviations.

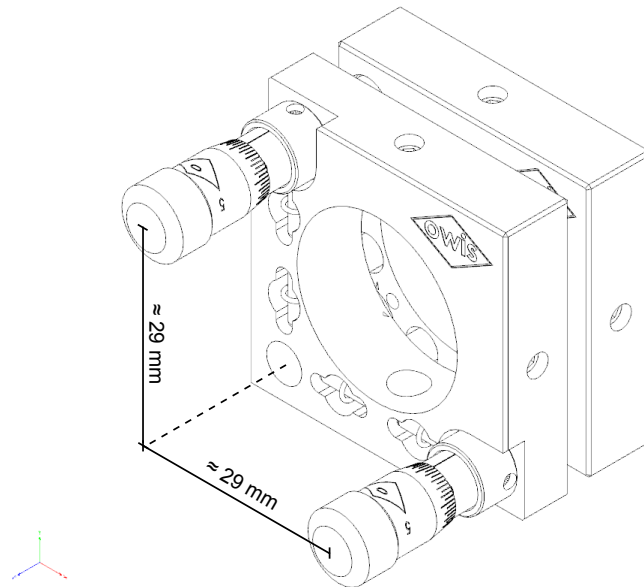


Figure 3.57.: Drawing of the OWIS TRANS 40-D25-MS mount used in the experiment, illustrating the distance between the touching point of the micrometer screw and the center of rotation used to calculate the change in angle. Source: [56], edited.

For calibration, the fiber mounts were tilted by the minimum amount readable from the scale of the micrometer screws used to facilitate the tilting. The change in angle can be calculated from the known distance between the center of rotation and the touching point of the screw, which is approximately 29 mm in this case, using the OWIS TRANS 40-D25-MS mounts installed in the experiment (c.f. Figure 3.57). Changing the length of the screw by 0.01 mm results in a change in angle of  $\text{atan}(0.01 \text{ mm}/29 \text{ mm}) \approx 0.01 \text{ mm}/29 \text{ mm} \approx 344.8 \text{ } \mu\text{rad}$  tilt. The DWS angle was recorded during this tilt and calibration was performed by dividing the peak-to-peak change in DWS phase by the value of  $344.8 \text{ } \mu\text{rad}$ .

For illustration, consider the time series data presented in Figure 3.58. It shows the DWS signals found during calibration in each of the phase meter channels. The upper two graphs show the horizontal DWS signal of all three interferometers during the time when the beam was tilted in the horizontal direction. The lower two graphs show the vertical DWS signals during vertical beam tilting. The peak-to-peak DWS variation in each of the channels is approximately 1.2 rad, yielding a calibration factor of  $1.2 \text{ rad}_{\text{DWS}}/344.8 \text{ } \mu\text{rad} \approx 3480 \text{ (rad}_{\text{DWS}}/\text{rad)}$ .

### Comparison to picometer experiment

Similar measurements have been made at a different experiment at the AEI, whose aim it was to confirm that length and beam jitter measurements at the required noise level for LISA can be made using the techniques available. For “historical”

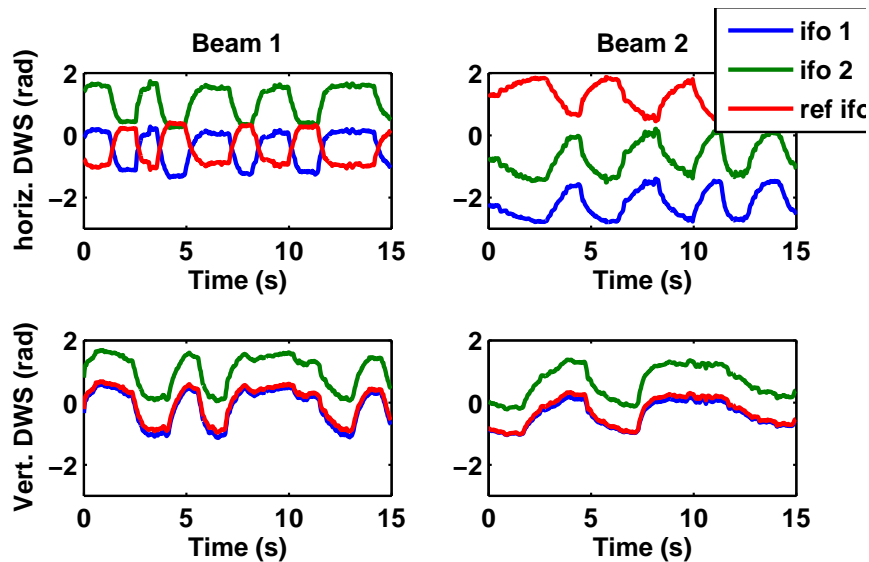


Figure 3.58.: Calibration of the differential wave front sensing (DWS) signals by tilting the input beams by known angles ( $\approx 344.8 \mu\text{rad}$ )

reasons, a different type of fiber coupler was used in this experiment, which makes it interesting to compare these measurements to the ones presented in the previous chapter, and thus to identify possible advantages or disadvantages of each type of coupler.

Figure 3.61 shows a photograph of the adjustable fiber mounts used in the picometer experiment. One of the coupler assemblies consists of a conventional tip-tilt mount rigidly connected to the aluminum base plate holding the experiment and two additional 45 degree angle of incidence mirrors which allow additional adjustment of the beam's position and direction. The other coupler only consists of a conventional tip-tilt mount, because the first mount already provides all the degrees of freedom required for the alignment of this particular interferometer. The second beam only needs to be adjusted such that it is parallel to the Zerodur™ base plate used in this experiment.

Figure 3.60 shows a similar photograph of the non-reciprocity experiment for comparison. The insets on the right hand side show a detailed view of the fiber couplers used in this experiment. Here, both couplers are identical. They feature an x-y-translation mount with solid state hinges for lateral beam position adjustment, into which a tip-tilt mount was affixed for beam angle adjustment. The fiber coupling assembly is placed in the middle of the latter.

As a calibration similar to the one described above was not performed in the picometer experiment, beam pointing fluctuations were compared on a raw DWS signal basis. Although the calibration factors are not expected to be exactly identical, they are expected to be at least of comparable magnitude due to the same beam diameter and similar distances from fiber coupler to interference point used in

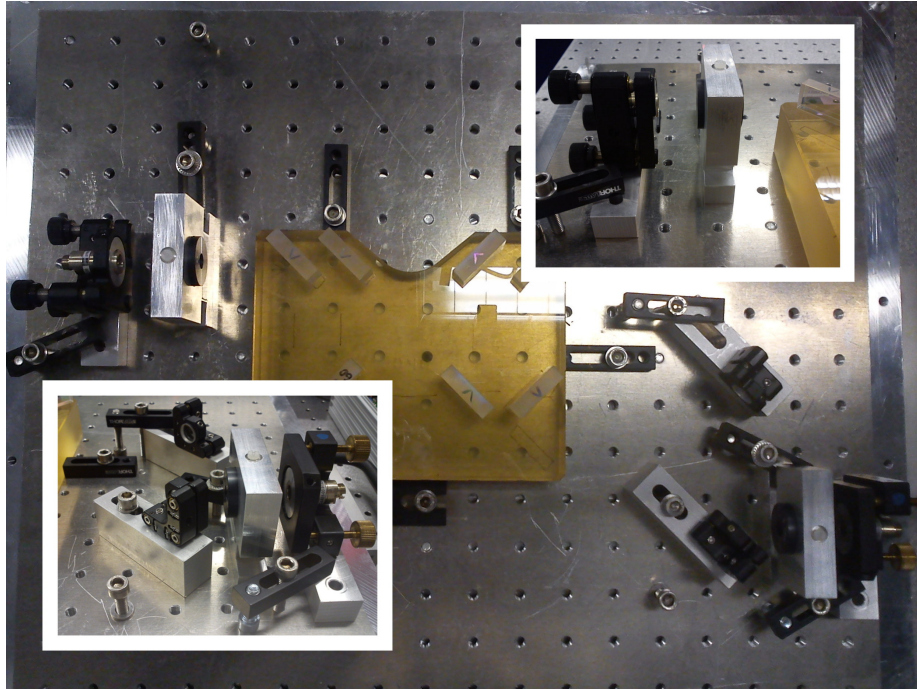


Figure 3.59.: Photograph of the picometer experiment with insets showing the fiber couplers used here in a more detailed side view.

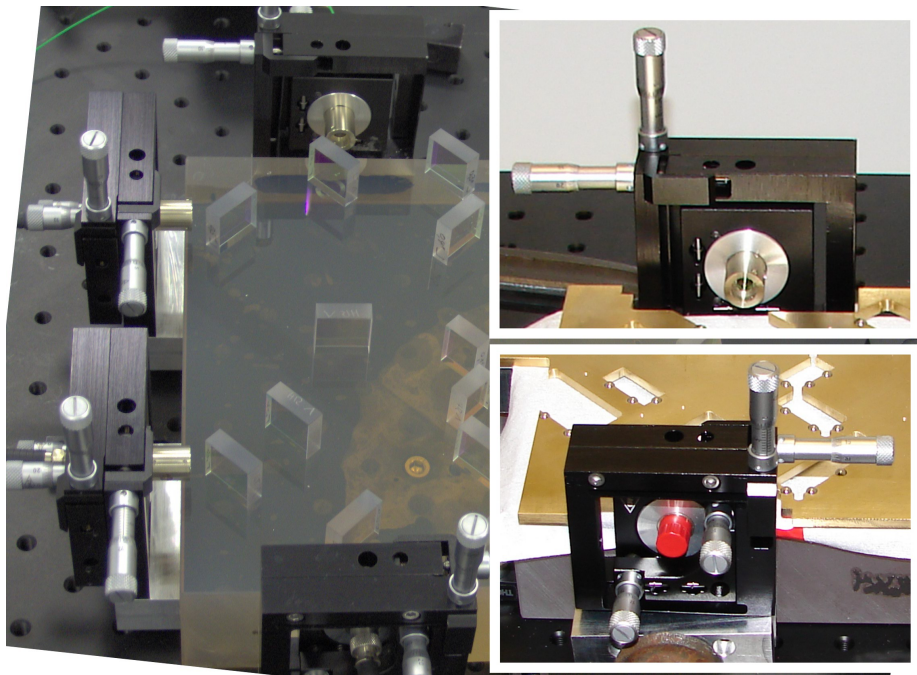


Figure 3.60.: Fiber couplers in the non-reciprocity experiment. Insets show detailed front and rear views of couplers.



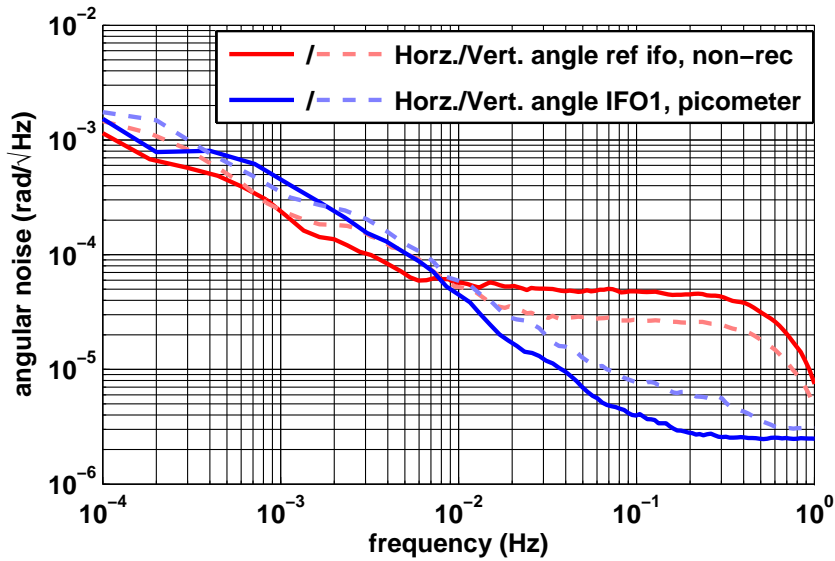


Figure 3.61.: Comparison of raw (unscaled) differential wave front sensing (DWS) signals between non-reciprocity experiment and picometer experiment.

both experiments. Data on beam jitter in the picometer experiment was taken and kindly provided by Christian Diekmann, who was responsible for this experiment at that time.

Figure 3.61 shows spectra of the angular noise from both experiments for comparison. The angular noise in both the horizontal and vertical direction in the picometer experiment are much lower than the noise in the non-reciprocity experiment in the frequency range above about 10 mHz. The non-reciprocity experiment's noise curves feature a shoulder-like noise shape, with a flat noise of about  $50 \mu\text{rad}$  which only drops off at about 1 Hertz. Below 10 mHz both noise shapes look very similar.

Comparison of the noise spectra from the different experiments suggests that the beam jitter noise is not higher in the non-reciprocity experiment but rather appears to be higher due to the increased stray light levels. Such reflections are only present in the non-reciprocity experiment, where they are known to induce shoulder-shaped noise.

### Noise reduction by differential wave front sensing (DWS) signal subtraction

As indicated above, the apparent beam pointing noise seems to be at least partly due to residual spurious beat notes from ghost beams. This makes the beam pointing jitter signal another good candidate for noise subtraction, since the signal is at least in principle sensitive to stray light, and potentially with a high gain allowing very accurate measurement of this noise source.

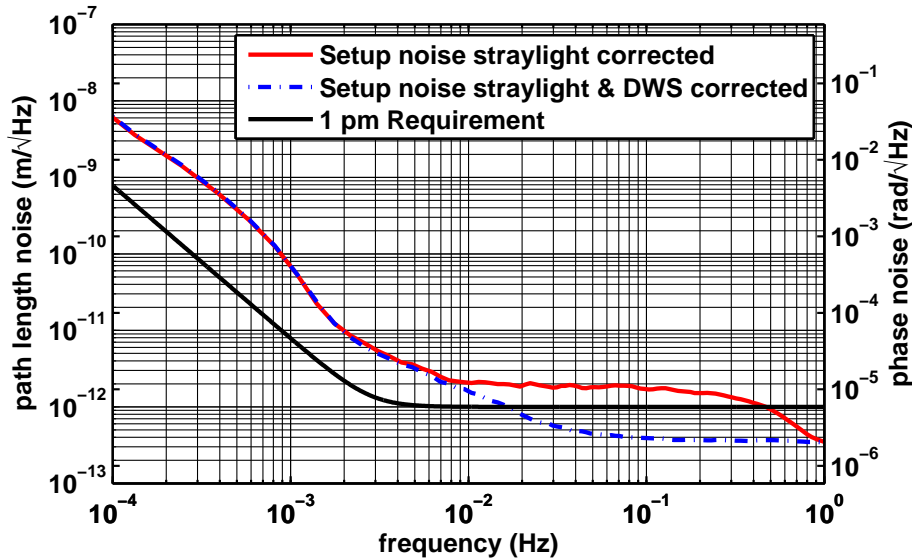


Figure 3.62.: Comparison of noise after using balanced detection and after the additional differential wave front signal subtraction.

It was therefore attempted to fit the beam pointing jitter data to the remaining non-reciprocal noise after applying balanced detection. This was accomplished using MATLAB©'s built in least squares fit method applied to filtered time series data of the DWS signals. This yielded the proper coupling factors which were later used with unfiltered data to subtract this noise source.

The application of a low pass filter before the fitting routine was crucial in this step such as to avoid fitting data that is not dominated by the influence of the beam pointing signals. A second order infinite impulse response (IIR) band pass filter with corner frequencies of 10 mHz and 100 mHz was used to isolate the mid frequency region for the fitting process.

The results of this noise subtraction step are shown in Figure 3.62. The noise level achieved after using balanced detection is shown in solid red. It has a shoulder-like shape with a steep decrease above one Hertz. The dashed blue trace represents the noise obtained after the differential wave front signals are used in a subtraction step. This trace is about a factor of five lower than the red one, and the shoulder above 1 Hz is gone. Instead, the noise flattens out at high frequencies at a level of about 0.4 picometer/ $\sqrt{\text{Hz}}$ , while it increases like  $1/f^2$  for frequencies below about 5 mHz. Thus it seems evident that the fitting routine used to remove the beam pointing jitter in fact subtracts residual stray-light, picked up by the more sensitive DWS signals.



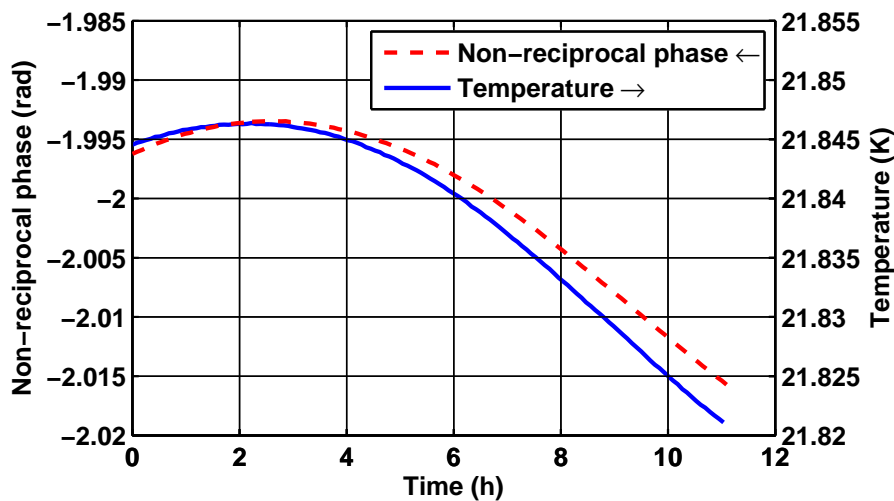


Figure 3.63.: Time series plot of the Zerodur™ base plate temperature and non-reciprocal phase revealing correlations between the two signals.

### 3.6.3. Temperature noise subtraction

Finally, at very low frequencies (i.e. below 1 mHz), the temperature noise becomes the dominant noise source. The temperature's influence on the non-reciprocal phase can still be measured, despite the fact that the temperature stability at the base plate is already very good due to the temperature isolation and the base plate's very low coefficient of thermal expansion.

Still, investigation of the time series reveals that the long term trend of the temperature measurement and the non-reciprocal phase is in fact very similar. This is reflected in Figure 3.63. It shows both these signals on a single plot over the course of almost 12 hours. The non-reciprocal phase uses the left hand y-axis and the temperature is depicted using the right hand y-axis. This way both traces line up nicely, revealing the correlation between the two signals.

An x-y plot of a segment of this data from about 6 h to 10h, as shown in Figure 3.64 allows the calculation of the coupling coefficient between temperature and non-reciprocal phase. This graph shows a linear relationship between the two variables, with a slope of approximately  $2 \text{ nm}/0.01 \text{ K} = 200 \text{ nm/K}$ . Note that this is approximately ten times larger than one would expect using the coefficient of thermal expansion (CTE) of Zerodur and an optical path length of even maximally 1 m. The expected thermal expansion of the base plate is only  $0.02 \times 10^{-6} / \text{K} \times 1 \text{ m} = 20 \text{ nm/K}$ .

The reason for this discrepancy remains unknown. One possible explanation could be that the manufacturer used Zerodur™ of expansion class 2, whose CTE is specified to be  $0 \pm 0.1 \times 10^{-6} / \text{K}$  [41], either unknowingly, due to a mistake, or to

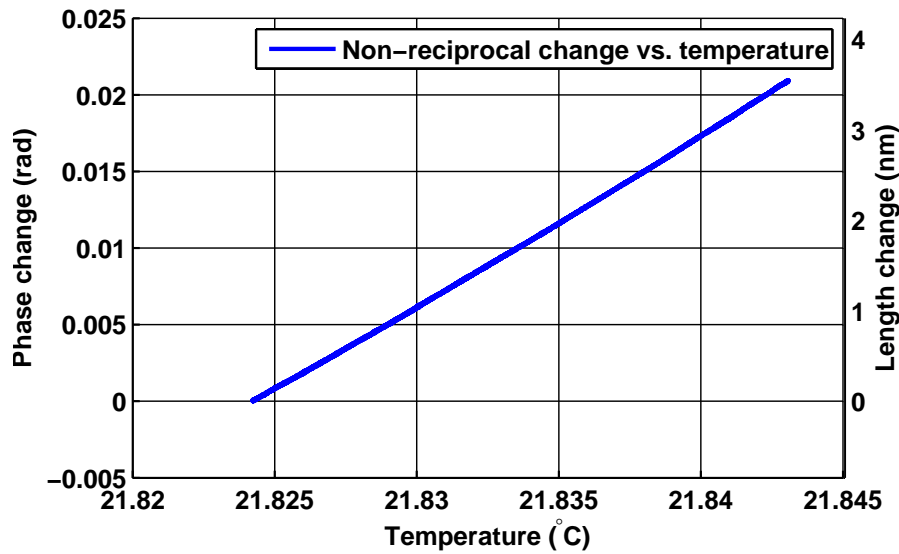


Figure 3.64.: Temperature coefficient of non-reciprocity (fiber measurement)

save money. Another factor leading to a larger observed CTE could be that the photo detectors add a temperature dependent phase shift, mimicking an expansion of the optical base plate.

Regardless of the reason for this excess thermal expansion, it was attempted to find a way to reduce its influence on the measurement of the non-reciprocal phase. One way to achieve this would be to improve the thermal isolation of the vacuum chamber.

Due to spatial constraints inside the vacuum chamber it was not possible to implement a second thermal shield similar to the first one described in Section 3.5.5. Therefore, it was decided to add an additional layer of thermal isolation on the outside of the vacuum chamber. To achieve this, extruded polystyrene foam<sup>1</sup> plates of 2 cm thickness were glued to the outside of the vacuum chamber. This type of plate is commonly used for thermal insulation purposes e.g. in buildings. This was intended to improve the thermal isolation of the chamber by reducing the temperature transfer from the air in the lab to the vacuum chamber through convection, as it shields off the air currents. Additionally, extruded polystyrene foam features a low thermal conductivity, also adding to the reduction of thermal transfer from the surroundings to the vacuum chamber.

Figure 3.65 shows a photograph of the vacuum chamber with this additional layer of temperature isolation installed. One can see that all sides of the chamber and the door are covered with the green or light violet colored extruded polystyrene foam plates.

<sup>1</sup>Commonly known as Styrofoam®, produced by Dow Chemical Company. However, a generic type was used here.

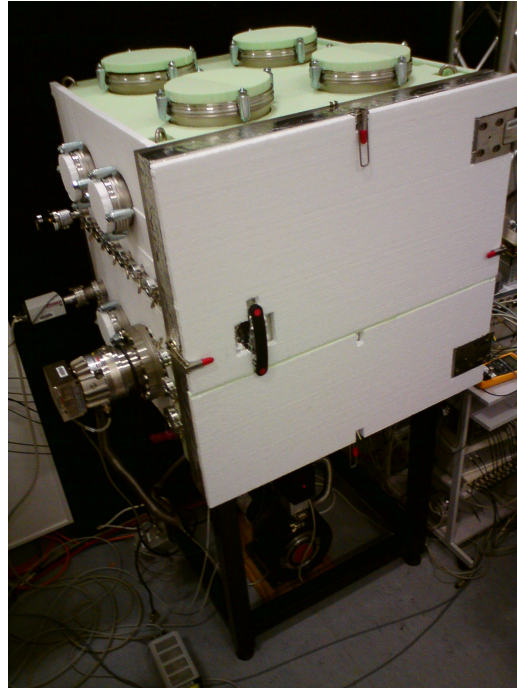


Figure 3.65.: Photograph of the vacuum chamber with external thermal shield installed.

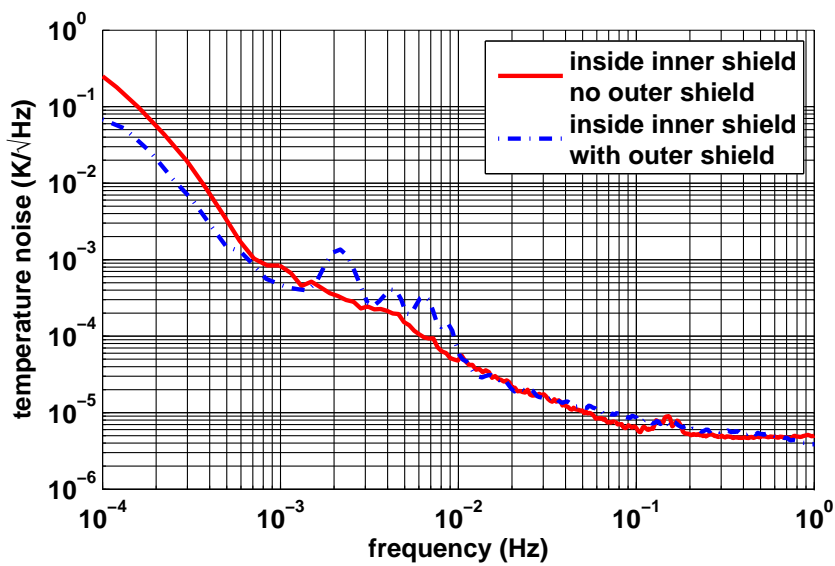


Figure 3.66.: Temperature noise encountered at the Zerodur© base plate with the new, outer thermal shield installed, compared to the noise encountered without the additional outer insulation.

A comparison between the temperature noise inside the vacuum chamber prior to the installation of the additional layer of thermal isolation on the outside and the temperature noise after the additional thermal isolation was installed is presented in Figure 3.66. The solid red trace, representing temperature noise in the vacuum chamber without thermal isolation on the outside has a flat shape for frequencies above 0.1 Hz at a level of several  $\mu\text{K}/\sqrt{\text{Hz}}$ . Between 1 mHz and 0.1 Hz the noise shape follows a  $1/f$  curve, while for even lower frequencies the noise increases as  $1/f^2$ . Comparing this to the dashed, blue trace, one finds that there is only a very small difference between the two curves in the frequency range below 1 mHz.

Thus, it can be concluded that adding additional thermal insulation on the outside of the vacuum chamber does not improve thermal stability much on the inside. Apparently, the thermal low-pass filter formed by the outer isolation has a corner frequency which is too high to lead to a noteworthy reduction of temperature noise in the vacuum chamber. The outer isolation was still kept in place for subsequent measurements, to benefit at least from the small improvement in temperature noise that was observed. However, the amount of noise reduction was not sufficient to remove the influence of temperature-induced noise on the observed non-reciprocity.

Therefore, the temperature measurements were used in a linear fit to find a coefficient between temperature and non-reciprocal phase. This coefficient was used to subtract the temperature induced non-reciprocal phase-changes leaving only genuine non-reciprocal phase changes and remaining noise sources in the measurement setup.

The resulting noise spectral density is shown in Figure 3.67. It shows the observed setup noise with all previous corrections applied in comparison to the non-reciprocal noise observed after additionally applying the temperature noise subtraction. As temperature noise only has an effect in the very low frequency range, an improvement is only observed below 1 mHz. Noise at higher frequencies remains unchanged, due to the already sensor noise limited temperature data.

## 3.7. Results

This section presents the observed non-reciprocity results after all subtractions have been applied. Section 3.7.1 deals with the setup noise, in order to evaluate the minimum achievable noise level possible using this setup and the noise subtractions presented in the previous sections.

Finally, the non-reciprocal noise of the fiber under test is discussed in Section 3.7.2.

### 3.7.1. Setup noise

During the noise hunting process most measurements were performed without the fiber in place but by using the *null measurement path*, whose beams do not pass

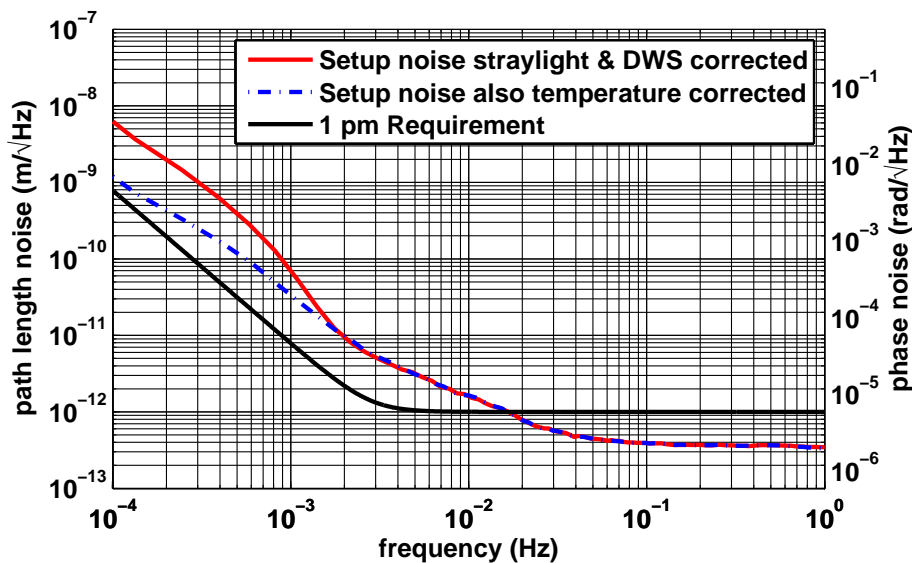


Figure 3.67.: Comparison of setup noise observed after subtracting stray light and differential wave front sensing (DWS) noise and after additionally subtracting temperature noise.

through the fiber. This path allows investigation of the equivalent non-reciprocal noise floor inherent to the setup, which is even present without the fiber and thus represents a lower limit on measurable fiber non-reciprocal noise. It avoids the complications introduced when using the fiber path, as e.g. additional alignment challenges and lower light power due to limited coupling efficiency through the fiber under test.

The results are presented in Figure 3.68, which shows first the raw setup noise data. For this trace, the raw phase measurements from all quadrant photo detectors were used in the combination yielding the non-reciprocity and eliminating the path length fluctuations in the modulation bench. As is expected, this noise is relatively high, at a level of about  $0.1 \text{ nm}/\sqrt{\text{Hz}}$ , with a shoulder-like noise shape dropping off steeply above 1 Hz.

The second trace, already well below this noise level, represents the data obtained after using the balanced detection scheme, which cancels the stray light present in the detection process. It has a similar shoulder-like shape, but the overall noise level is about two orders of magnitude lower, with only  $3 \text{ pm}/\sqrt{\text{Hz}}$  in the mid-frequency range.

A further reduction of the observed noise level is achieved by using the differential wave front sensing signals in a fit to the data and subtracting the correlations. While it may seem that this process would result in a subtraction of beam pointing jitter induced phase changes, the findings presented in Section 3.6.2 seem to indi-

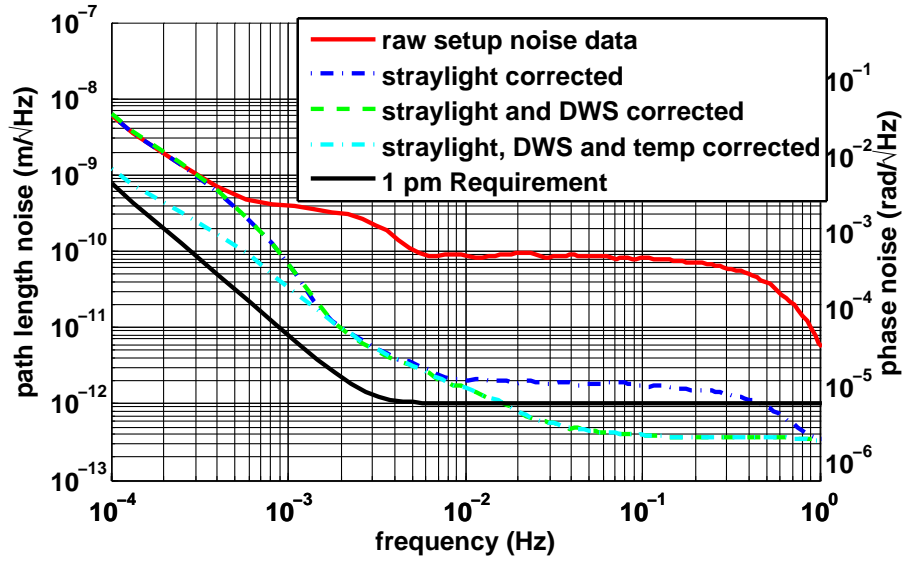


Figure 3.68.: Setup noise with all corrections applied

cate that this is merely a more sensitive measurement with subsequent subtraction of the remaining stray light.

Finally, the remaining trace shows the non-reciprocity after additionally applying a fit of the temperature data to the observed non-reciprocity. In this step, the residual expansion of beam paths only passed by one of the beams is reduced. This final trace is below the 1 pm requirement placed on the fiber's non-reciprocal noise for frequencies above 10 mHz and only violating the requirement in the low frequency range (below 10 mHz), and even there only by approximately a factor of two.

At this point it was decided to not put much more work into the improvement of the setup (e.g. by further improving temperature stability or by reducing stray light), but to instead move on to a measurement of an actual fiber, to see if the same low noise level can be achieved even with a potentially non-reciprocal medium introduced into the beam path.

### 3.7.2. Fiber non-reciprocity

After (finally) finding that the setup noise can be reduced far enough to achieve non-reciprocity measurements at the picometer level, measurements were performed on a single-mode, polarization-maintaining fiber. A Schäfter & Kirchoff vacuum compatible PANDA-type fiber was chosen, because this type of fiber is the most advanced polarization-maintaining fiber, providing the best extinction ratio among commercially available fibers. Although this fiber was acquired through Schäfter & Kirchoff, PANDA fibers from other vendors are expected to yield identical results, due to the fact that all PANDA fibers are made by the same company, namely

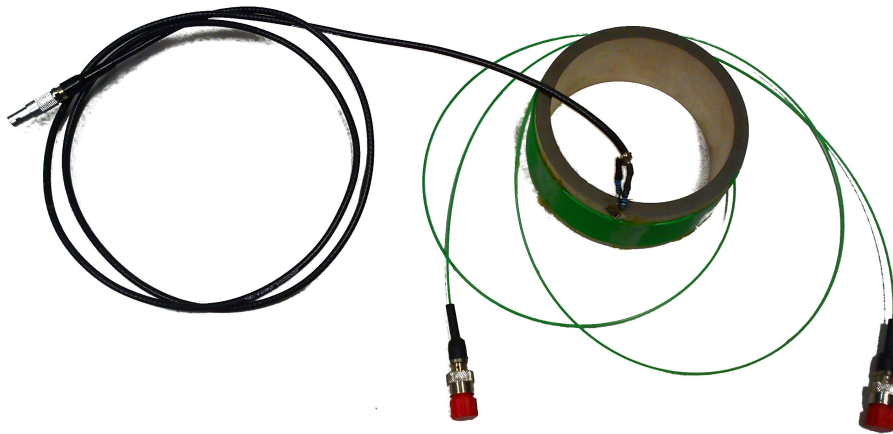


Figure 3.69.: Photograph of the fiber under test wound onto a ring made from piezo-electric ceramic, as used in the experiment.

nufern. The only difference between vendors is the type of connector (FC/APC connectors were chosen here) and the price, naturally.

As mentioned earlier (c.f. Section 3.5.9), the fiber was glued to a ring made from piezo-electric ceramic to facilitate length stabilization of the fiber path. While this is not thought to be strictly necessary to achieve low non-reciprocal noise, it was necessary here due to the imperfections in the phase meter that was used for these observations.

Figure 3.69 shows a photograph of the fiber under test wound around the ring made from piezo-electric ceramic. The fiber was 7 meters long. This is expected to be roughly representative of the length of fiber required on board a satellite to connect two optical benches, taking the extra length required for routing of the fiber into account.

This fiber was added to the experiment and the null measurement path was blocked, such that the light now had to travel through the fiber and its non-reciprocal noise could be observed. The introduction of the fiber required some alignment to achieve optimal coupling from light through the fiber while maintaining reasonable contrast in the measurement interferometers. Fortunately, the fiber mounts provided sufficient degrees of freedom to facilitate both. The coupling efficiency reached in the experiment was about 70 % in one direction and 80 % in the opposite direction. Contrast in the measurement interferometers was relatively low. About 60 % of the theoretically possible contrast was achieved. Full contrast could not be achieved mainly because the recombination beam splitter was not alignable and it was apparently not in the optimal position for ideal interferometric contrast. Furthermore, the many degrees of freedom resulting from the use of adjustable fiber mounts meant that combinations of tilts and/or position of fiber couplers were possible which did not result in strong changes in contrast, but were nevertheless displaced from the ideal position (i.e. the one used in the bonding procedure).



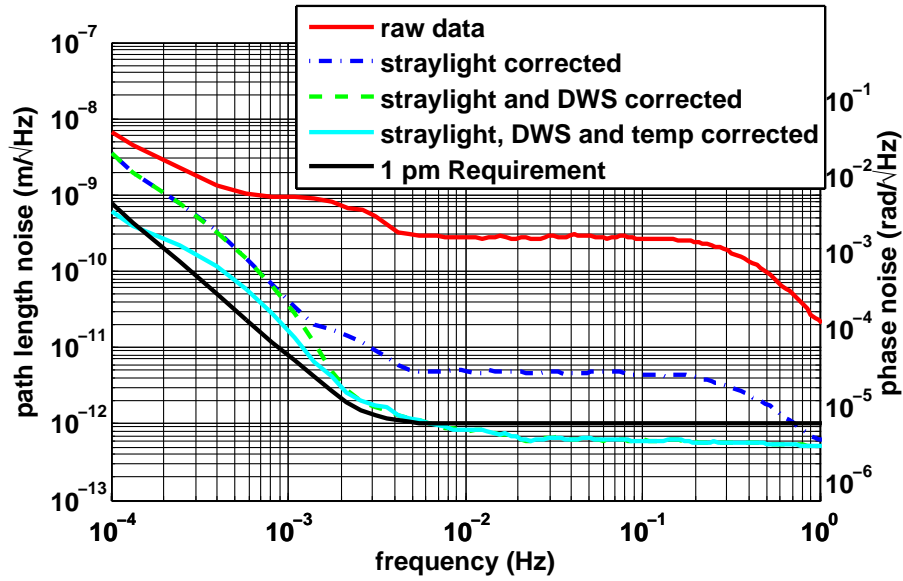


Figure 3.70.: Observed non-reciprocity. The graph is shows raw data as well as residual noise levels after subtraction of known noise sources.

After the alignment process was finished, measurements were taken. The experiment was conducted in vacuum at a pressure level of less than 20 nbar. The pressure was still decreasing during the time data was taken due to the fact that the turbo-molecular pump was still running. Optical path length difference stabilization, fiber length stabilization and laser amplitude stabilization were active and working during the time span used for the calculation of the noise spectral density.

The results obtained using this configuration are shown in Figure 3.70. As can be seen, the raw measurements, represented by the uppermost, red trace are far above the requirement (black trace). A noise level even worse than in the null-measurement of about  $0.3 \text{ nm}/\sqrt{\text{Hz}}$  is achieved using only the raw data from the quadrant detectors. The same shoulder-like noise shape is present as in the measurements of the setup noise, hinting that this is caused by the same noise source, or at least dominated by this noise source.

The next trace, shown in blue, represents the noise remaining after the application of balanced detection, where signals from both recombination beam splitter ports are used in the measurement. This strongly reduces the effect of stray light and leads to a noise level of only about  $5 \text{ picometer}/\sqrt{\text{Hz}}$ , again slightly higher than in the null measurement.

The green trace shows the remaining noise after the next step of data post processing, namely the subtraction of DWS signals from the non-reciprocal data stream. The noise is reduced even further to now only about  $0.8 \text{ picometer}/\sqrt{\text{Hz}}$ , and the shoulder-like shape is also removed. The noise is white for frequencies above 5 mHz and rises proportional to  $1/f^2$  toward lower frequencies, which



effectively lets it follow the requirements quite closely, albeit a bit above them for low frequencies due to the slightly higher corner frequency.

The noise below 1 mHz is finally slightly reduced when the temperature of the Zerodur™ base plate is fit to the non-reciprocal data and subtracted. The resulting noise level is shown here in cyan. It now lies almost exactly on top of the requirements curve, shown in black for reference.

In conclusion, it can be said that the fiber under test fulfills the requirement. Although the noise level observed here is slightly (less than a factor of two) above the requirements in the frequency range between 0.1 mHz and 1 mHz, this is most probably due to thermal effects, which will be much reduced on orbit, where the fiber is in a very temperature stable environment. However, this noise level can only be observed with the use of balanced detection, because stray light would otherwise spoil the measurement.

While the fiber generally seems to be compliant with the mission requirements, the fact that balanced detection is crucial for the performance of the measurements puts some serious constraints on the optical design of the mission. The consequences of these findings for the mission are described in detail in Chapter 6.



---

## Direct reflection measurements

---

As it became clear that most non-reciprocal noise was introduced by the presence of spurious reflections, some effort was made to identify the exact place where these signals originate and to identify ways to eliminate them.

While the measurement of reflections is generally possible using a slightly modified version of the fiber non-reciprocity measurement setup as illustrated in Figure 4.1, this is not very favorable because this setup does not allow easy removal of some optical components or interfaces individually to measure their effect on the spurious reflection. Furthermore, it is always necessary for light to travel through the fiber in both directions simultaneously, which prevents the removal of the output fiber interface.

In the slightly modified version of the non-reciprocity experiment shown in Figure 4.1, a beam dump in the path between the first fiber launcher and the recombination beam splitter prevents light from this fiber launcher to serve as a local oscillator in the measurement interferometer. Therefore, the only detectable signal at this point has to stem from spurious light from the fiber launcher that still reached the photo diode and is thereby able to interfere with the light from the fiber launcher on the opposite side to generate a beat note at the heterodyne frequency. This could in principle be done symmetrically to observe spurious beat signals in both measurement interferometers at the same time, however we chose to only do this on one measurement interferometer at a time due to the inherent symmetry of the setup.

While this setup allowed identification of the fiber under test with its two interfaces as the source of a large amount of the stray light, it did not allow removal of e.g. the output fiber coupler or the whole fiber itself to eliminate its contribution to the spurious signals and to measure the effect of the input fiber coupler individually. Therefore, a new experiment was conceived, which would serve solely to measure spurious reflections of optical components.

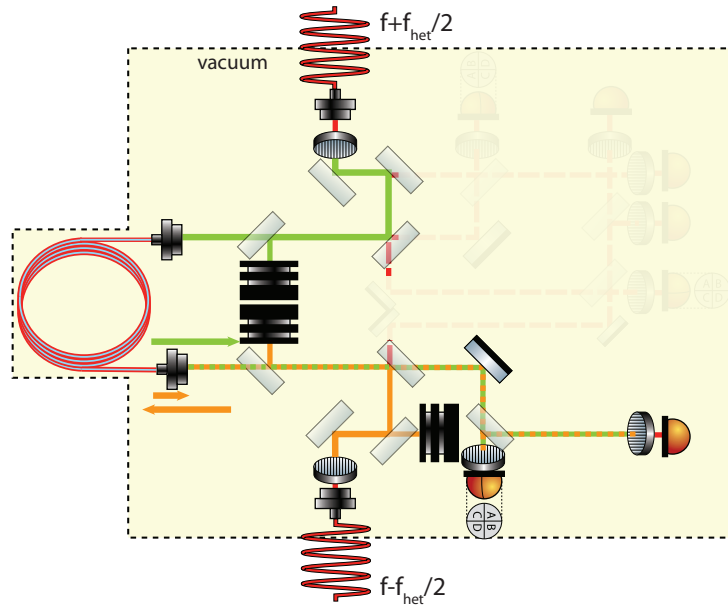


Figure 4.1.: Slightly modified non-reciprocity experimental setup to allow direct reflection measurement

## 4.1. Initial setup

The first design of this setup is illustrated in Figure 4.2. In this design, light from the same modulation bench used in the non-reciprocity experiments is used to generate interference signals. One beam enters at the top left and serves as local oscillator in the experiment. It is directed to a recombination beam splitter with a photo detector in one of its outputs. The second beam, entering directly below the first one, is also guided to the recombination beam splitter, but from a direction which does not directly lead to interference. Instead, one of the output beams is directed toward the device under test, which reflects a small fraction of the incoming light power back toward the recombination beam splitter, where it now enters from the right to interfere with the local oscillator. The amplitude of the resulting interference signal is measured and compared to the beat signal amplitude resulting from (almost) 100 % reflection from a mirror.

This technique is especially sensitive to even small amounts of reflected power due to the use of a local oscillator beam for signal amplification. From the interference of the (relatively strong) local oscillator signal and the weak reflection signal one obtains a signal amplitude that is proportional to the square root of the product of the two beams' powers,  $A_{\text{signal}} \propto \sqrt{P_{\text{reflected}} P_{\text{LO}}}$ . The relative reflectivity of the device under test is obtained by dividing this amplitude by the amplitude observed in a measurement with 100% reflectivity:  $r_{\text{DUT}} = A_{\text{signal}} / A_{100\%} \propto \sqrt{P_{\text{reflected}} / P_{100\%}}$ . Keeping in mind that the reflectivity is a number that is always between zero and one, this leads to a significant improvement over the direct measurement of the reflected beam power, which would lead a signal proportional to  $P_{\text{reflected}} / P_{100\%}$ .

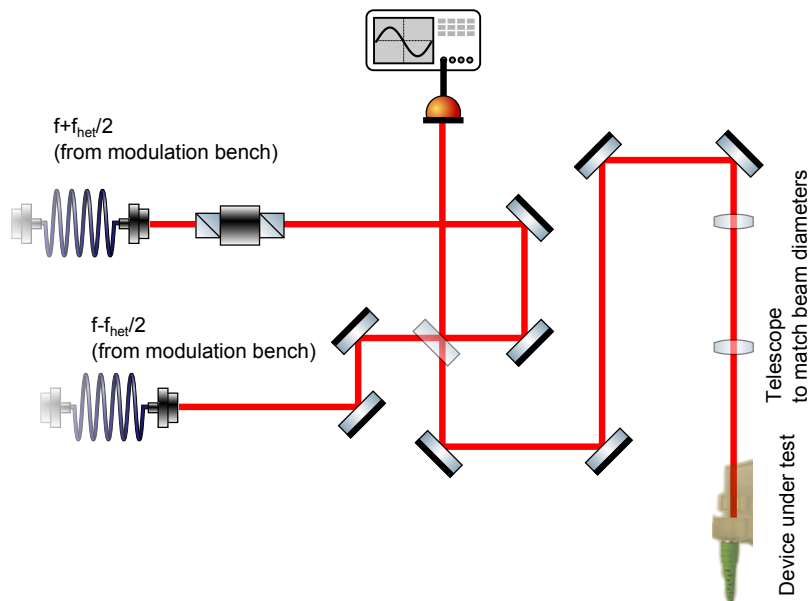


Figure 4.2.: Schematic of the first direct reflection setup, used (among other things) to measure the reflections from a first FIOS prototype kindly provided by UGL

To give an example: With a typical power reflectivity of  $10^{-6}$  one would get a signal that is at  $1 \mu\text{V}$  compared to one volt in the direct reflection measurement, whereas with this setup a signal of  $1 \text{ mV}$  compared to a  $1 \text{ V}$  signal can be obtained.

Furthermore this setup is only sensitive to the light reflected from the fiber in the same spatial mode as the beam emerging from the fiber and with a frequency difference corresponding to the offset frequency used. In a simple power detection setup, all light arriving at the detector would be accounted for, but here one is only interested in the fraction of the light leading to spurious beat signals.

A photograph of the first design of this setup can be found in Figure 4.3. Here it is shown with a prototype FIOS installed, which at that time was on loan from the University of Glasgow to conduct a measurement of its reflectivity. As was expected, this particular design produced relatively high back reflection due to its non-angled design, which featured a zero degree of incidence optical interface.

This measurement confirmed that a central design criterion of the fiber interface should be to avoid surfaces with a zero degree angle of incidence and without anti-reflective coating, as these will inevitably result in Fresnel reflections of a few percent of the incident light power. This has since been implemented in the most recent design of the LISA pathfinder FIOS, which features an eight degree angle between the incident light beam and the first substrate surface.

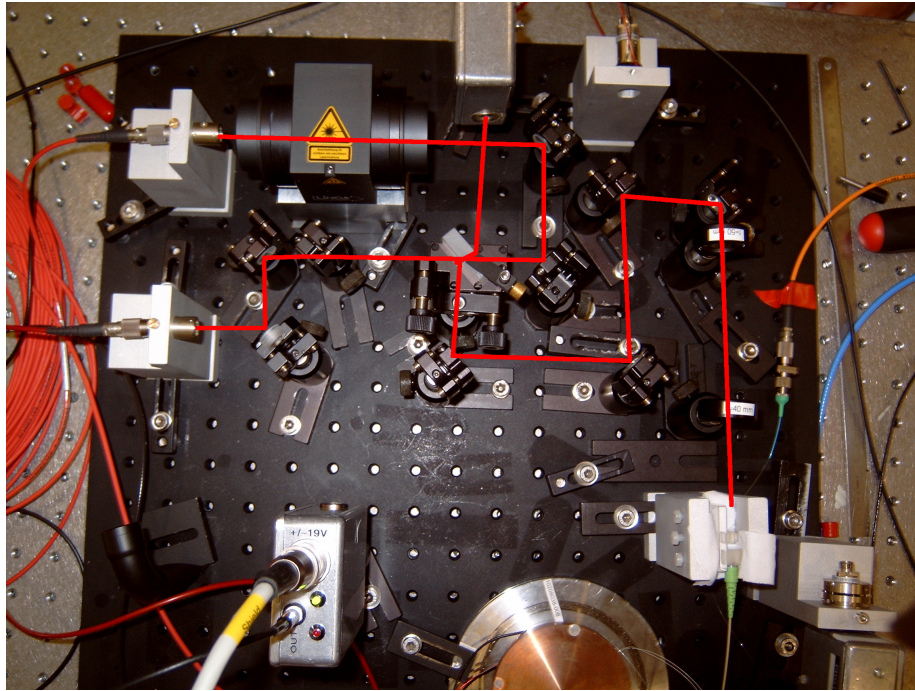


Figure 4.3.: First version of the direct stray light measurement setup in use with an early prototype of a quasi-monolithic fiber injector optical sub-assembly (FIOS)

## 4.2. Improved setup

As this setup turned out to be very useful in the measurement of minute reflections from optical interfaces, an improved version was built. The main difference in this new design is the introduction of a flip mount that allows repeatable removal of one mirror from the beam path in order to switch between a setup that allows adjustment for optimal interferometric contrast and the actual measurement of the reflectivity. This way, the measurement of many fibers could be accomplished in much shorter time. This setup was designed together with Jan Rybizki, as part of his Diploma thesis work.

## 4.3. AR coated fibers

As it was speculated that the largest part of the reflected light stems from the uncoated fiber interface, attempts were made to acquire fibers with an AR coating. This turned out to be harder than expected, as most people consider the return loss of single mode fibers with angle polished connectors at typically a few parts per million already very low, and therefore, requests for anti-reflective coatings on fibers are very uncommon. It was still possible to identify two possible suppliers and samples from both were ordered.

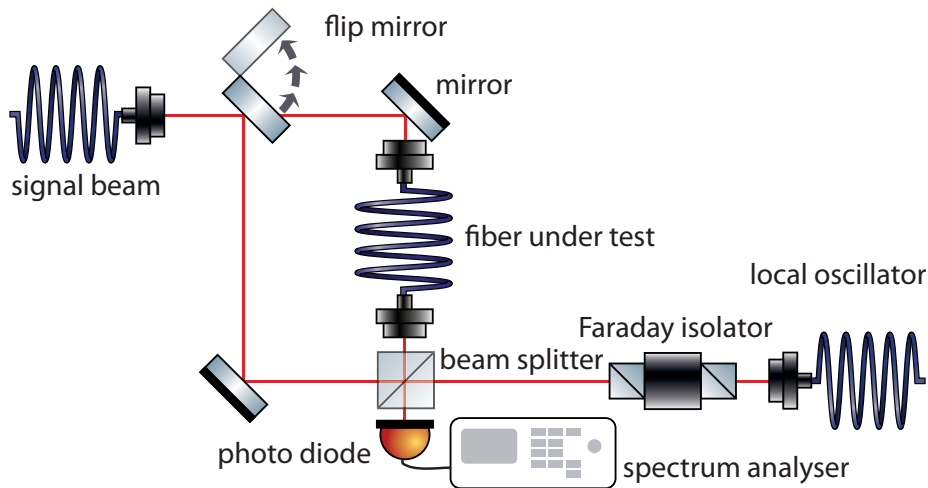


Figure 4.4.: Schematic of the improved reflection measurement setup, c.f. [57]

Unfortunately, it turned out later that one of the supplied fibers was not polarization-maintaining, so only one single-mode, polarization-maintaining fiber with an anti-reflective coating could be tested. The results of these measurements can be found in Table 4.1, along with the measurements performed on all other fibers available at that time. As one can see from the table, the AR-coated fiber shows a relatively low reflectivity, but it is not the lowest reflectivity among all fibers investigated. Notably, the reflectivity of some non-AR-coated fibers was lower. This led to the investigation of the origin of the reflection discussed in the following section.

#### 4.4. Identification of the origin of the reflection

As mentioned before, one of the main advantages of the dedicated reflection measurement setup was, that it allowed removal of individual components from the beam path to identify the origin and the relative amplitude of the reflections.

Experimentally, this was accomplished by stepwise removal of all components required for coupling light into the fiber. In the first step, the remote fiber coupler at the other end was removed. Then, a special fiber was used, which was wound very tightly around a pen, which leads to absorption of all light traveling through the fiber in its cladding, because that light is no longer guided with such steep bend angles. This was done at different fiber lengths, to identify the amount of reflected light being generated in the bulk of the fiber core. Finally, the fiber was completely removed, leaving only the lens in the front fiber coupler as a source of reflected light.

Figure 4.5 summarizes the results from all these measurements. It is evident that the reflection cannot be attributed to a single part but there are several components that contribute to the overall observed reflected light amplitude. The main con-

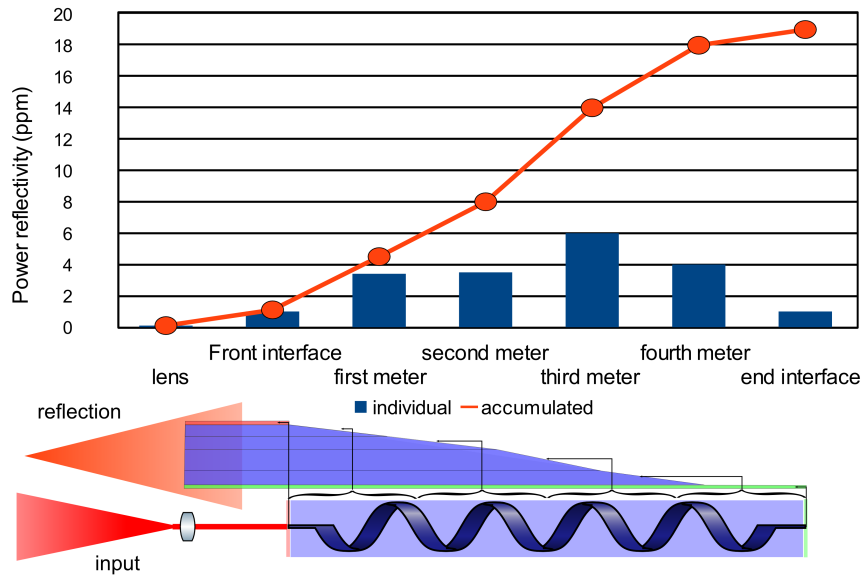


Figure 4.5.: Reflections from different parts of the fiber under test, showing the relative amplitude of each contributing element.

tributor in a fiber of 4 m length was identified as the fiber bulk material. It was observed that the reflected light increased with the length of fiber used, hence one can conclude that scattering in the fiber core of this particular fiber contributes about 4 parts per million (ppm) per meter of fiber. The lens was found to contribute only 0.1 ppm, while the fiber interface itself led to a reflection of 1 ppm.

## 4.5. Results

Using the improved setup detailed in the previous section, a survey of all available fibers in our lab was made. The results of this survey are summarized in Table 4.1. Among the various different suppliers and types of fibers and connectors, no fiber could be found that exhibited a reflectivity of less than a few ppm.

## 4.6. Conclusion

The results presented in this chapter show that it will be impossible to achieve the required extremely low power reflectivity of  $10^{-12}$  using the optical fiber technology currently available. As detailed in Section 4.4, a main contributor to reflected light is scattering in the fiber's core, which could only potentially be reduced by changing the laser wavelength to a region where lower losses are observed in the fiber core. The dominant loss mechanism in fused silica fibers at near infrared wavelengths is Rayleigh scattering, thus one can assume that lower



Table 4.1.: Reflectivities of selected fibers.

Name	Jacket	Company	R (ppm)	Length (m)
PM980-XP Panda	no	Thorlabs	4	1.5
#47439-1 AVIM	both	SuK	7	3
#49366-03 PM980HP	no	SuK	10	1.5
AR coated	no	Thorlabs	11	1.5
S/N 2358	no	OFR	17	2
#53537-2-01 iron plate	yes	SuK	20	5.5
#500727-02	yes	SuK	20	4
#53537-5-02	yes	SuK	20	4.25
PIEZO fiber	yes		20	7
#500771-01	both	SuK	28	9
#5357-2-02	yes	SuK	29	5.5
#500727-01	yes	SuK	30	4
#49087-203 PM980HP	no	SuK	30	11
#53537-1-01	yes	SuK	35	10
#53537-4-02	yes	SuK	36	4
#46210-1-01	no	SuK	63	40
PIEZO fiber #2	yes		400	7
SEDI	no	SEDI	500	4
stripped fiber	yes	SuK	570	6
broken PIEZO fiber	yes		600	
#53537-4-01	yes	SuK	1720	4

losses in transmission correspond to lower observed levels of reflection. For the fused silica fibers used here, this would mean that a wavelength of 1550 nm would have to be used [58].

Given the maturity of laser and optical designs for the current base line wavelength of 1064 nm, this seems a very undesirable move. Furthermore, this would “only” decrease reflectivity by about one order of magnitude as absorption in fused silica decreases from about 2 decibel per kilometer at 1064 nm to 0.2 decibel per kilometer at 1550 nm. Therefore, this seems hardly a good incentive to change the laser wavelength.

In conclusion, it seems to be unavoidable to find another way of dealing with the inevitable reflections stemming from the backlink fiber. Several such alternative approaches are discussed in Chapter 6.



---

## Digitally enhanced heterodyne interferometry

---

During the LISA Symposium in 2010 it became clear that recent developments in digitally enhanced interferometry at the Australian National University (ANU) would ideally fit with the measurements of fiber non-reciprocity at the AEI. This is due to the unique properties and advantages of digitally enhanced heterodyne interferometry [59], most importantly the ability to reject stray light which was at that point already identified as a main noise source.

The collaboration was established by a visit of Danielle Wuchenich, a PhD student at ANU, who worked at the AEI from October to December 2010. Work continued until mid 2011, when the digital signal processing had to be shipped back to the ANU for use there in other experiments (and due to customs regulations). Consequently, all results presented in this chapter were obtained in collaboration with and with support of Danielle Wuchenich and Daniel Shaddock.

### 5.1. Potential benefits of digital heterodyne interferometry

The use of pseudo random codes in digital heterodyne interferometry makes it possible to distinguish between beat signals originating from different points in the setup through their different travel times. The laser light is modulated with a code, and a delayed copy of the same code is used in the demodulation. A beat signal is only demodulated correctly if the relative time shift of the modulation and demodulation code matches the light's travel time in the setup. With a sufficiently high code bandwidth this allows for accurate selection of desired light travel times, leading in turn to the rejection of unwanted signals from e.g. stray-light [59, 60].

These codes are easily implemented because a very similar technique is also

foreseen for ranging, i.e for the measurement of the absolute arm length of the LISA arms [61, 62, 63]. Therefore, the “infrastructure” required to generate these codes is already in place, and the phase meter will also already be able to decode and measure these signals. The main difference is in the code rate and the modulation depth required for digital heterodyne interferometry.

While it is planned to use about 2 MHz of the available bandwidth for the ranging codes, the digital heterodyne interferometry codes will require a much larger bandwidth of several hundred MHz. This is easily possible with the modulators foreseen for LISA, because they will also be used to generate the clock tone sidebands, currently planned to be around 2.5 GHz from the main science beat note. Therefore, the modulators will provide more than enough bandwidth.

The second difference is the modulation depth. The ranging sidebands will only use about 1 percent of the carrier power. For digital heterodyne interferometry, the situation is reversed and the modulation index will be chosen such that no power remains in the carrier but power is spread over the whole bandwidth. However, this could also easily be achieved with the modulators foreseen for LISA, because they are fiber coupled and use a waveguide structure, which yields a very high modulation efficiency, enabling such a modulation with only moderate input voltages [64, 65].

The stray light beat note seems to originate from the fiber and its interface, which is considerably further away from the photo diode than the recombination beam splitter. Therefore it is possible to achieve stray light suppression without the use of an additional photo diode by just using digital heterodyne interferometry.

For this to work it is necessary to use a code whose smallest step length is shorter than the path length difference between the nominal and the stray light beat note. For use in the backlink fiber setup this means the step length needs to be shorter than about 0.5 m, as can be seen by comparing the two distances in the schematic of the current design of the LISA optical bench shown in Figure 5.1. This corresponds to a minimum modulation frequency of  $c/L \approx 600$  MHz.

## 5.2. Required setup changes

The setup changes required to facilitate digitally enhanced heterodyne interferometric readout are comparatively small. As the goal in this experiment was not to multiplex several measurements into one (as is also possible using DI, [66]) but to reduce spurious signals from reflections or polarization changes, the number of photo diodes and phase meter channels did not have to be changed.

However, as DI requires a much higher detection bandwidth, it proved necessary to replace the large area silicon photo detectors with smaller area InGaAs detectors which have a much smaller capacitance and can therefore provide much higher bandwidth. In this case we were using a modulation bandwidth of 80 MHz, limited by the capabilities of the FPGA electronics used for code generation and demodu-

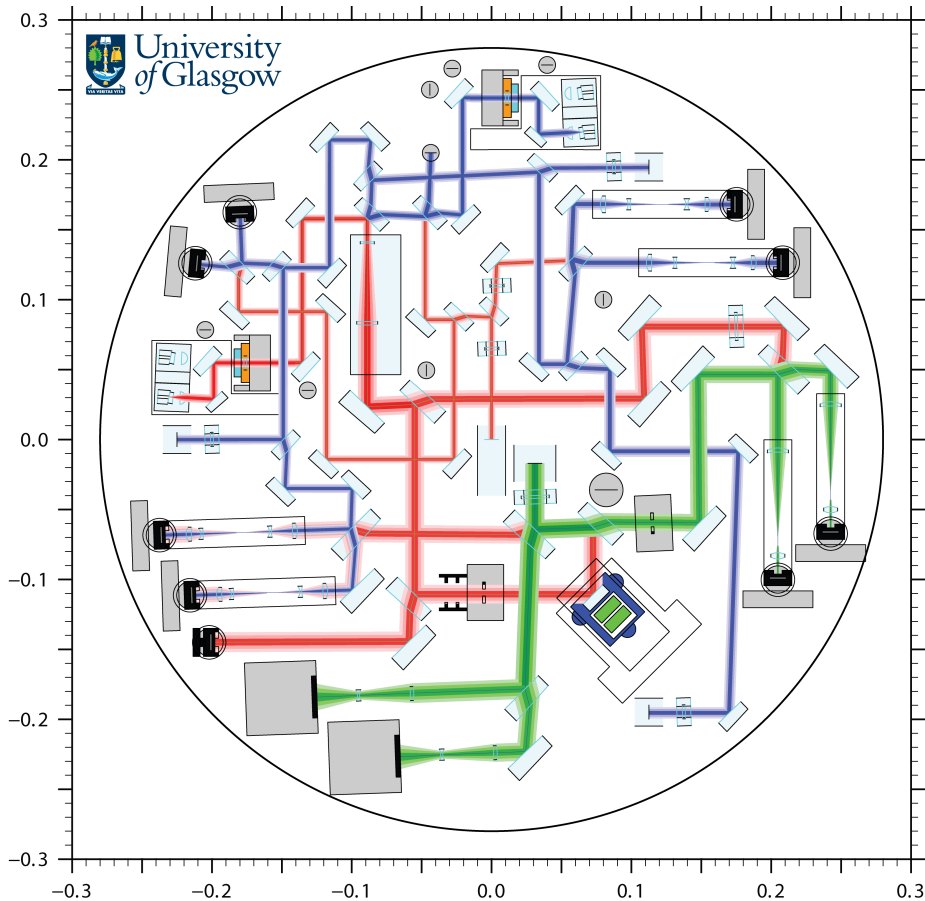


Figure 5.1.: Current design of the LISA optical bench elegant breadboard (EBB). Image courtesy of University of Glasgow (UGL).

lation. This led to a bandwidth requirement of at least 80 MHz on the new photo detectors to be used in the experiment.

To facilitate the phase modulation, fiber coupled electro-optical phase modulators (EOMs) were added to the setup. This was easily accomplished because optical fibers were already used to send light into the vacuum chamber. Therefore the modulators could be added here with a simple fiber to fiber connector, without the need for realignment. For technical reasons (one of the EOMs available was already spliced to a vacuum feed through fiber) one of these feed through fibers was replaced with the fiber containing the EOM. However, this was also possible without much realignment troubles, because the fiber only had to be added to the mounts which were already in place. Some realignment remained to be done because the fibers are not always exactly centered with respect to the mounts (fiber cores have a diameter of only a few  $\mu\text{m}$ ) and therefore the alignment of input beam and output beam coupler had to be slightly adjusted for this.

For technical reasons (high pass filters installed in the ADCs and programming of the phase meter hardware) it was also necessary to increase the heterodyne

frequency from the previously used 1.623 kHz or 17.85 kHz to around 1 MHz. Due to the design of the modulation bench, two options were available to achieve this heterodyne frequency. The first option was to leave the optical setup as it was and just exchange the offset lock previously used to generate the two modulation frequencies of  $80 \text{ MHz} \pm f_{\text{het}}/2$  with a dual function generator capable of providing two input signals for the AOM drivers offset by about 1 MHz. This is described in more detail in the following subsection.

The second alternative is to offset lock a second laser to the frequency stabilized master laser which was used in all previous experiments. To accomplish this, a few additions to the optical setup were necessary, as well as new electronics to facilitate offset phase locking of two lasers. This is described in detail in Section 5.2.2.

The remaining changes only concerned the phase measurement and data acquisition part of the experiment, i.e. no optics had to be changed. For data acquisition, the hardware phase meter (PM) was replaced with another FPGA based phase meter and demodulation system. This consisted of a 15 bit resolution 80 MHz ADC for each channel which was read out and demodulated using FPGA based electronics. The demodulated signal was then sent to a second FPGA based electronics board responsible for the phase measurement and data transfer to the host computer which was in charge of data acquisition. Phase data was saved to a file for later analysis (e.g. computation of the non-reciprocal phase and spectral analysis).

### 5.2.1. Modulation bench for MHz range offset frequencies

When the implementation of MHz offset frequencies on the optical bench began, the optical part of the modulation bench remained unchanged. First, an approach was chosen that would re-use as many parts as possible of the existing experiment. Here this meant that the AOMs previously responsible for the generation of the beat note frequency had to be driven at different frequencies, this time not several kHz apart but about 1 MHz.

Fortunately, despite the fact that the AOM electronics are tuned to a resonance frequency of 80 MHz – to ease their use by enabling moderate input signal amplitudes resulting in acceptable diffraction efficiencies – the bandwidth of the resonance still allowed the AOMs to be driven at frequencies about 500 kHz removed from the resonance without much loss in diffraction efficiency.

Thus, it was only necessary to change the AOM driving electronics [67, Section 5.5] such that they would not use their internal oscillator but merely function as an amplifier for input signals provided from a signal generator. Due to the modular design of these amplifiers this was relatively easy, requiring only the addition of another input connector directly attached to the internal amplifier of the AOM driving electronics. Even the output power stabilization and modulation input could be kept functional.

The remaining part of the electronics – the 80 MHz voltage-controlled crystal oscillators and their kHz-range offset lock – could not be re-used due to the fact

that the tuning range of their internal voltage controlled oscillators was only about 10 kHz. While replacing them with different oscillators with a wider tuning range would have been a possible alternative, it was decided to use a dual channel function generator (Tektronix AFG3102) instead. The two channels of this type of function generator are tightly synchronized, thus eliminating the need for an offset locking loop to stabilize the relative phase of the two output signals as would have been the case with two individual function generators.

### 5.2.2. Optical laser offset locking for MHz range beat notes

An enhancement of the optical part of the modulation bench to allow offset locking of two lasers was added as an alternative to the modulation technique involving two AOMs driven at frequencies offset by the desired beat note frequency described in the previous subsection. The main incentive to do this was that driving the two AOMs at offset frequencies required relatively high power electrical drive signals (about 2 Watts of radio frequency (RF) power are required to enable a diffraction efficiency of about 50 %), which led to strong electromagnetic pickup signals in the measurement. The use of offset locked lasers promised to work with much lower electrical signal power, thus greatly reducing electrical noise at the beat note frequency in the lab.

The way forward chosen in this case is outlined in Figure 5.2. To allow easy switching between the two alternative beat note frequency generation techniques, it was decided to make only a few changes to the setup to enable offset locking. Due to the modular design of the modulation bench this was possible without much effort. A second laser was already in place and coupled to a fiber. The original reason for this laser was to act as a spare in case the Iodine stabilized laser is needed in other experiments. It would then easily have been possible (and has in fact been done a few times) to plug in the fiber carrying the light from the second laser instead of the output fiber from the Iodine stabilized laser.

Another fiber coupler was added to allow light to be fed from this laser into the vacuum feed-through fibers. The open port of the beam splitter in front of the fibers was used as input, thus allowing replacement of the input from one of the AOMs with light from the second laser. Two steering mirrors had to be placed between the fiber output and the beam splitter to facilitate coupling of the light into the fibers.

To allow offset locking of this laser to the Iodine stabilized laser, a glass plate was placed in this beam which tapped off about four percent of this laser's light. This light was then guided to a recombination beam splitter via another steering mirror, which, in conjunction with the beam splitter, provided the alignment facilities required for optimal overlap of this beam with the beam from the Iodine stabilized laser, entering at the second port of the recombination beam splitter.

The light from the Iodine stabilized laser was tapped off via a fiber coupled beam splitter introduced at the input of the second vacuum feed-through fiber and brought to the recombination beam splitter by means of another fiber coupler.

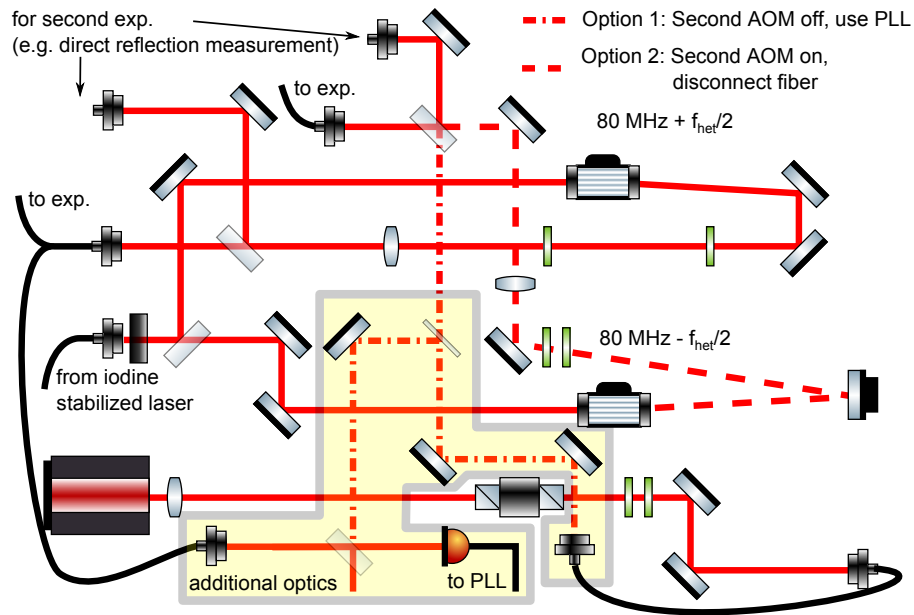


Figure 5.2.: Schematic of the modulation bench after modifications to facilitate offset-locking of two lasers were made.

The use of the fiber beam splitter was necessary to avoid the additional 80 MHz frequency shift in the light going to the experiment that would have occurred if light from before the AOM had been used for phase locking. Furthermore, it helped to avoid the need for re-alignment that would have arisen had another beam splitter or glass plate been introduced into the beam path before the fiber, which would certainly have reduced the fiber coupling efficiency through the accompanying lateral beam shift. The setup was completed by a photo diode which detected the beat note frequency of the two lasers and respective phase locking electronics [68].

To switch between the two operating modes of the modulation bench, one of the AOMs was disabled, thus eliminating the input of frequency shifted light into one of the fibers. This was then replaced by light from the second laser. This laser was in turn offset phase locked to the Iodine stabilized laser using the offset-locking electronics.

### 5.2.3. Phase measurement system

The use of digital interferometry also requires a specialized digital signal processing system, as described in detail in [59]. This was kindly provided by the Australian National University.



### 5.3. Characterization of the phase measurement system

Because the use of Digitally enhanced Interferometry required a new phase measurement system, this phase measurement system was first tested to verify that phase measurements at sub-picometer level were possible. The setup used in these tests resembled the one used previously for testing the old phase measurement system. A signal generator was used instead of the optical signals from the photo diodes. It was set to a frequency of 1.11748759 MHz (the heterodyne frequency chosen for the digital interferometry measurements) and an amplitude of  $1 V_{p-p}$ . The signal was then split using a T-piece and fed into the first two channels of the phase meter.

Figure 5.3 shows the results obtained during these tests using different configurations of the phase measurement system. At first, separate FPGAs were used to read out the analog-to-digital converters, which then reduced the resolution from 15 bits to 8 bits and transferred data to a different FPGA, which was responsible for the actual phase measurement. The scaling from 15 bits to 8 bits became necessary because of the limited number of input channels on the phase measurement FPGA board.

This configuration was initially chosen to facilitate the readout of 6 channels at once, which would have been too much of a burden for just one FPGA running the phase meter at the same time. However, as can be seen when observing the solid red trace in Figure 5.3, this led to excessive noise levels, violating the requirements at all observed frequencies.

To overcome this limitation, a different phase measurement system configuration was chosen. In this setup, the read-out and demodulation of the ADCs was still handled by one FPGA but the data was decimated to 40 MHz by averaging two consecutive decoded samples, before it was sent to the separate FPGA handling the phase measurement. This was done to reduce the burden on the data transmission. While 80 MHz transfer was possible using the system at hand, the higher data rate was associated with a higher timing jitter, which could be avoided by using this lower data transfer rate, without compromising the spatial resolution of the pseudorandom noise (PRN) codes, as data was still sampled and decoded at 80 MHz.

The differential phase noise using this configuration is represented by the dashed blue trace in Figure 5.3. This change in the configuration led to a reduction in phase measurement noise by approximately a factor of 10, now agreeing with the requirement of less than 1 picometer phase measurement noise.

Finally, a third configuration was tested, where the phase measurement was also handled by the FPGA reading the data from the analog-to-digital converters. This was previously not possible, because the FPGAs used for ADC readout were less powerful and could not handle simultaneous readout and phase measurement at 80 MHz. However, as the phase measurement rate had to be lowered to 40 MHz

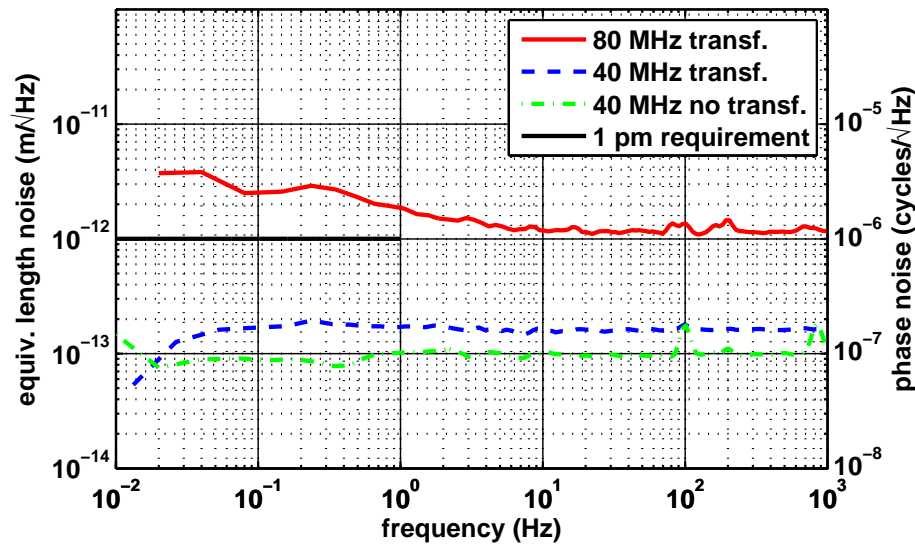


Figure 5.3.: Comparison of phase meter noise levels achieved using different configurations of the phase measurement system.

anyway to achieve appropriate phase measurement noise, it was now also possible to run the phase meter on the same FPGA, avoiding the need for data transfer and associated timing jitter issues completely. From the dot-dashed green trace in Figure 5.3, representing the differential phase noise observed using this configuration, one sees that an even lower phase noise is observed; 0.1 picometer/ $\sqrt{\text{Hz}}$  in the whole frequency range between 0.01 Hz and 1 kHz. As this setup led to the lowest differential phase noise, it was adopted for all further measurements.

It is, however, worth noting that no pseudo-random noise code was applied to the electrical signal, as this was not (easily) possible. While this code, if properly demodulated, is not expected to add phase noise in the measurement process, it presents an additional complexity in the measurement process and could potentially lead to phase noise by spurious or side effects, e.g. through imperfect, phase mismatched demodulation or signal degradation in the presence of the modulation.

In a second test, a more realistic assessment of the differential phase noise was attempted. While the signal from the signal generator in the previous test had a constant, relatively high amplitude of 1 V<sub>pp</sub> and a relatively constant phase – due to the fact that it was phase locked to the phase measurement system via the standard 10 MHz interface – typical photo diode signals encountered in the experiment had a lower amplitude of about 300 mV<sub>pp</sub> and their phase was not stable. The phase measurement noise test was therefore repeated using a corresponding amplitude setting of the signal generator and a phase modulation using the generator’s internal phase modulation source of 360° at a frequency of 1 Hz.

Figure 5.4 shows the differential phase noise between these first two phase meter channels using these input signals. It can be seen that the noise is below the 1

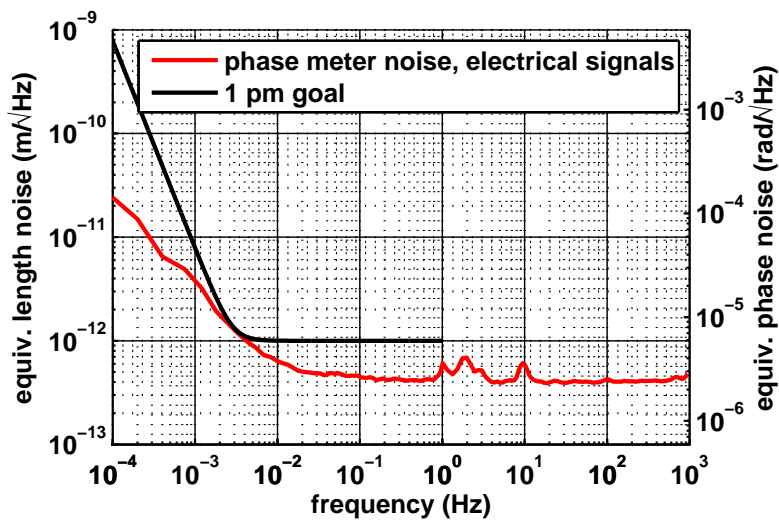


Figure 5.4.: Differential noise between two channels of the phase meter measuring the same signal generated by a signal generator.

pm requirement of the non-reciprocity, albeit only slightly at the corner of the requirements curve. This still means that the phase measurement performance of the phase meter used in the digital interferometry experiments is sufficient to potentially demonstrate sub-pm non-reciprocal noise in fibers.

## 5.4. First results

After the installation of all high bandwidth photo detectors, a first measurement of non-reciprocal noise using the digitally enhanced interferometry setup was taken. This time, only three photo detectors and corresponding phase meter channels were active, as this was only a first test of the applicability of the new technique. Thus, a balanced detection scheme as in the previous experiments was not possible. Instead the potential stray light rejection from using the digital codes would have to be relied upon. However, it was clear from the beginning that this would not be sufficient given the relatively low bandwidth of the detectors, which only allows rejection of spurious interference signals with a delay of more than 12.5 nanoseconds, corresponding to a path length difference of 3.75 meters, far more than would actually be present on the optical bench, except for reflections stemming from the opposite end of the fiber under test.

The first results of the non-reciprocal noise using digitally enhanced heterodyne interferometry are presented in Figure 5.5. Comparing the red trace – representing the non-reciprocal noise levels found in the experiment – to the black trace, – corresponding to the 1 picometer requirement – one finds that the observed non-

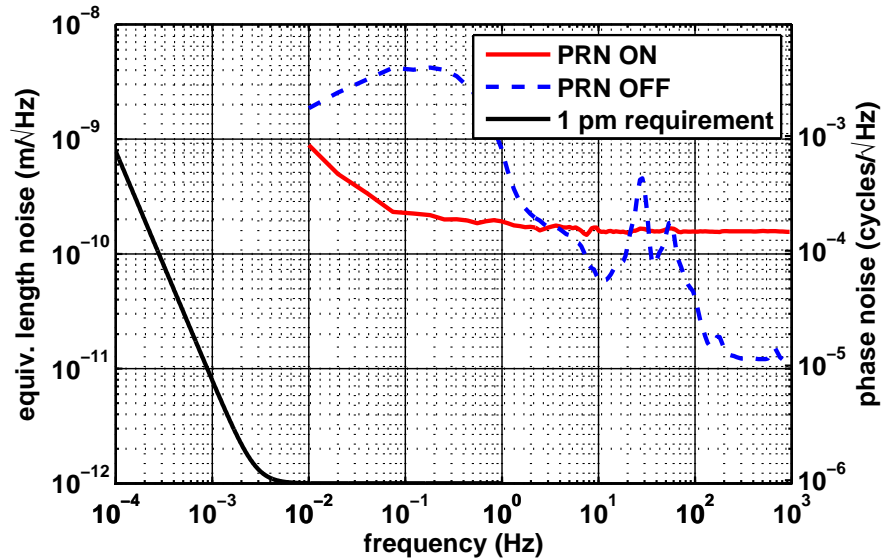


Figure 5.5.: Non-reciprocal noise encountered in a null measurement using digitally enhanced interferometry and conventional interferometry.

reciprocal noise is much higher than allowed. However, it can also be seen that this is not due to the PRN codes involved, as the measurement was repeated without using these codes. The noise observed without the PRN codes is represented by the dashed blue trace. In this case, noise is even higher at lower frequencies, but noise levels decrease as  $1/f$  toward higher frequencies.

## 5.5. Noise hunting

Soon after first measurements using the DI setup were taken, it turned out that measurement noise was far higher than in the previous experiments using classical interferometry. Therefore, noise hunting efforts were undertaken to identify the limiting noise source in this experiment. First, laser parameters were investigated to ensure single-mode operation of the laser offset locked to the Iodine stabilized laser, as described in Section 5.5.1.

After this, the differential photo detector noise was measured again for the new detectors used in this setup. This is described in Section 5.5.2. The subsequent Section 5.5.3 then discusses some aspects of the possible influence of the small detector size on this noise. This is of bigger concern than in the experiments without digitally enhanced interferometry, because there the detectors had a diameter much larger than the beam, whereas now the beam and detector are of comparable size and any pointing jitter could potentially lead to parts of the beam not being detected and consequently phase noise if the beam is not completely homogeneous (as is expected).

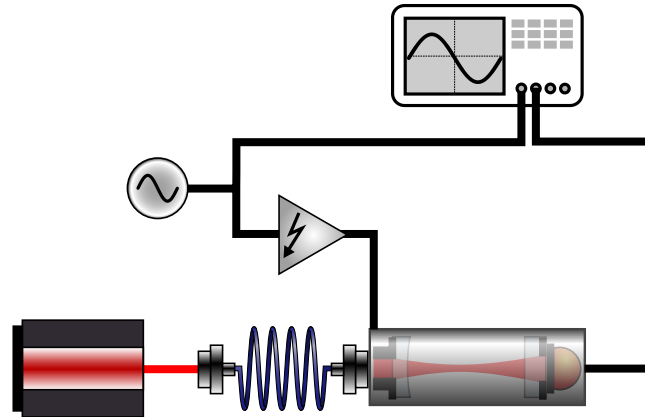


Figure 5.6.: Setup used to identify mode-hop free regions of the Innolight Mephisto laser, offset locked to the Iodine stabilized laser.

Section 5.5.4 deals with the potential influence of the pointing stability on the differential phase noise of the photo detectors. The issue of cladding modes in the fiber is somewhat related and is therefore also discussed in the same subsection. Cladding modes transmitted through the fiber may lead to apparent beam pointing fluctuations from the fiber output, in addition to the potential phase noise introduced by the changing path length seen by the modes traveling through the cladding, where they are no longer single mode.

### 5.5.1. Laser parameters

The frequent loss of lock when offset locking the Mephisto Innolight laser to the Iodine stabilized laser, as well as the increased noise levels in the differential photo diode measurements led to the suspicion that the Mephisto laser was possibly using operating parameters that led to non single-mode output. Thus, an optical spectrum analyzer was used to verify that the laser was indeed operating in a single mode fashion. The setup is shown in Figure 5.6.

Light from the laser is coupled into a fiber, which in turn delivers the light to a fiber coupled scanning Fabry-Perot interferometer. This interferometer allows identification of the presence of a second frequency in the laser's output and thus characterization of the single mode operation parameters.

Measurements were taken at seven different laser diode pump currents between 1.15 A and 1.45 A, and the laser crystal's temperature was varied for each pump current setting from the minimum to the maximum possible temperature setting of the laser driving electronics. Temperature ranges where single-mode operation was observed were recorded, and the plot shown in Figure 5.7 was generated from the data. It shows a two-dimensional plot with temperature and pump current

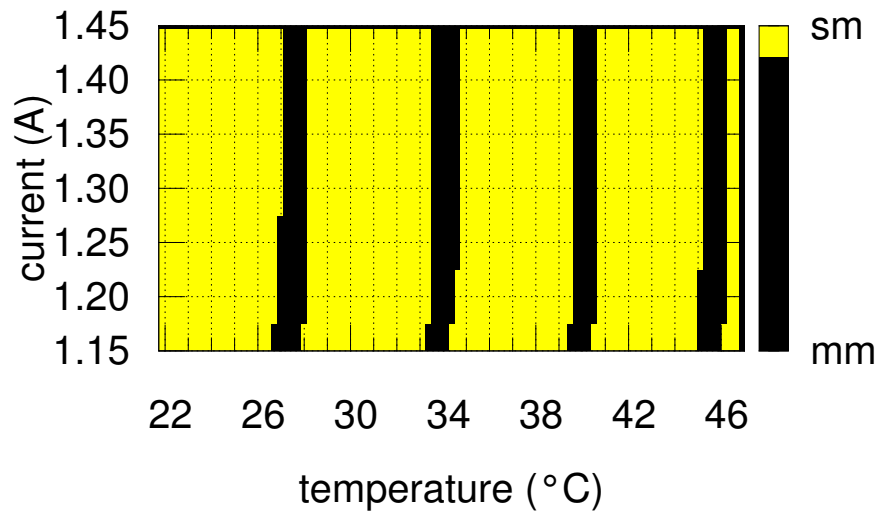


Figure 5.7.: Single mode operation parameters of the Innolight Mephisto laser used in the digitally enhanced interferometry experiments. sm = single mode, mm = multi-mode.

on the  $x$ - and  $y$ - axis respectively, where the single-mode operating regions are highlighted in yellow and the multi-mode regions are shown in black.

This “map” of the laser’s operating parameters allows selection of a combination of parameters that yields both the desired output frequency and sufficient margin for the phase-locked-loop to stay in stable operation conditions while changing the operating parameters to obtain a constant frequency offset between this laser and the Iodine stabilized master laser. In the end, these tests revealed that the operating parameters used previously (1.200 Amps pump diode current,  $\approx 31^\circ\text{C}$  crystal temperature) were not leading to multi-mode operation nor were they particularly close to a region where this would occur, and they were therefore not altered.

### 5.5.2. Differential photo diode noise

The next step after testing the phase meter and verifying that the differential noise between two channels using electrical signals was sufficiently low to allow measurement of non-reciprocal phase noise at the picometer level was to repeat the experiment using (nominally) identical optical signals, thereby testing the whole analog phase measurement chain noise. This was performed here in an analogous manner to the measurement in the experiment described in Section 3.4, i.e. by using an additional beam splitter in one of the interferometer outputs to sense a copy of the interference signal using a second photo detector.

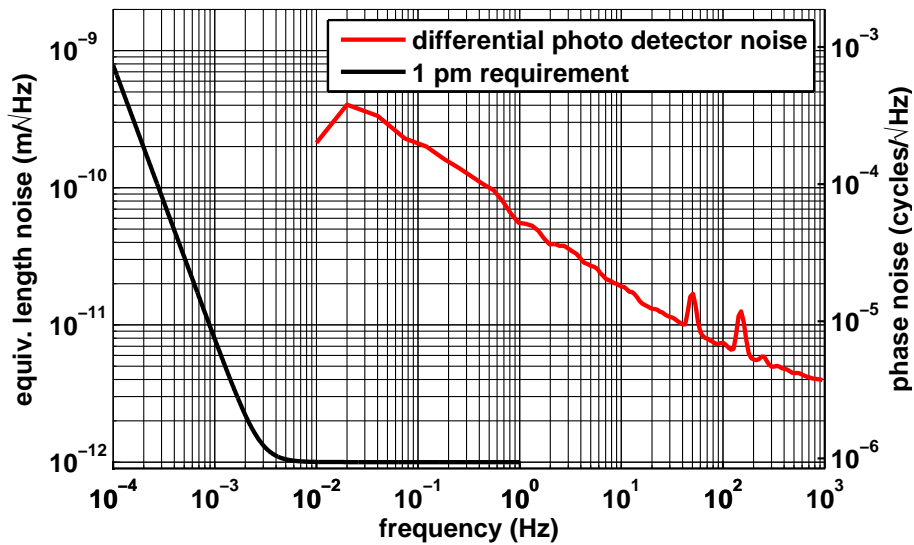


Figure 5.8.: First measurement of the differential phase noise of two photo detectors sensing an identical signal.

The result of this measurement can be found in Figure 5.8. The figure shows that the differential photo detector noise, shown in red, is much higher than the one picometer requirement. It begins at about  $4 \text{ pm}/\sqrt{\text{Hz}}$  at a frequency of 1 kHz and increases as  $1/f$  toward lower frequencies.

### 5.5.3. Beam centering considerations

The investigations described in the previous section revealed that one source of additional noise lay in the differential photo detector noise. Hence, additional investigations similar to the ones described in Section 3.4 were also carried out on this setup.

The experience from previous experiments was taken into account and polarizers were immediately put in front of all photo diodes to eliminate this noise source. Unfortunately, it turned out that this time they did not lead to an improvement in differential photo diode noise observed.

Considering the main differences between the previously used photo detectors and the new ones, the most likely candidate for the new noise source seems to be the small detector size. The high bandwidth requires a much lower photo diode capacitance, which is generally reached more easily using small active areas. The detectors used in this experiment had a diameter of merely  $70 \mu\text{m}$ , which requires an additional lens to focus the beam such that it impinges only on the active area and thus avoiding the loss of a major part of the signal.

Given the beam diameter of 2 mm set by the fiber couplers used in the setup and

the spatial constraints in the vacuum chamber and thermal shield, this requires lenses of relatively short focal lengths. Lenses of 100, 75, 50 and 40 mm focal length were used in the experiment since these were available. This in turn lead to two alignment challenges: first, the beams have to hit a detector active area of only  $(70\ \mu\text{m})^2$  and second, the detector has to be in close proximity of the focal length for the spot size of the beam to be below the diameter of the detector.

The latter is illustrated in Figure 5.9. Sub-figure 5.9d shows a simulation of the  $1/e^2$  beam diameter behind a 100 mm focal length lens around its focal point. The beam diameter is only below the critical  $70\ \mu\text{m}$  in a very small area around the focal point. A deviation of only about  $\pm 2\ \text{mm}$  is enough to make the beam larger than the detector. While a lens of shorter focal length (e.g. 50 mm as shown in Figure 5.9b) makes the beam slightly smaller around the focal point, it still requires a very good alignment of the distance between lens and detector.

This is further complicated due to the fact that the active area of the detector is usually inside a photo diode housing, which is not very accessible, such that the exact distance between detector and lens cannot be easily measured. One has to resort to an alignment technique where the beam is shifted sideways repeatedly while the photo diode is moved back and forth and its DC output signal is monitored. When the beam diameter is larger than the active area of the detector (i.e. when the diode is either too far from the lens or too close) the output signal starts rising when the beam starts hitting the photo diode at one edge. It continues to rise until the beam is fully centered on the diode and will then drop off again when the beam leaves it on the opposite side. In the case where the beam diameter is smaller than the active area, the output signal also starts to rise as soon as the beam starts to hit the detector on one side. In contrast to the situation where the beam is larger than the diode, in this case a constant maximum signal will be reached when the beam fully hits the diode, which only starts to drop off when part of the beam leaves the diode on the opposite side. Thus, the correct distance can be identified when the plateau in the output signal remains stable under the largest sideways deviations of the input beam.

While this allowed centering the beams relatively reliably on the detectors, the small size of the detectors still poses a problem due to a potential increase in beam pointing sensitivity. With large active areas the beam still stays on the photo diode, even in the presence of relatively high beam pointing noise. However, this may not be the case with smaller detectors, where even very small changes in beam pointing can lead to a different part of the beam being detected, and thus to a different overall phase. As this effect can be more or less pronounced depending on the distance between the fiber coupler and the detector, this can also lead to differential photo diode noise.



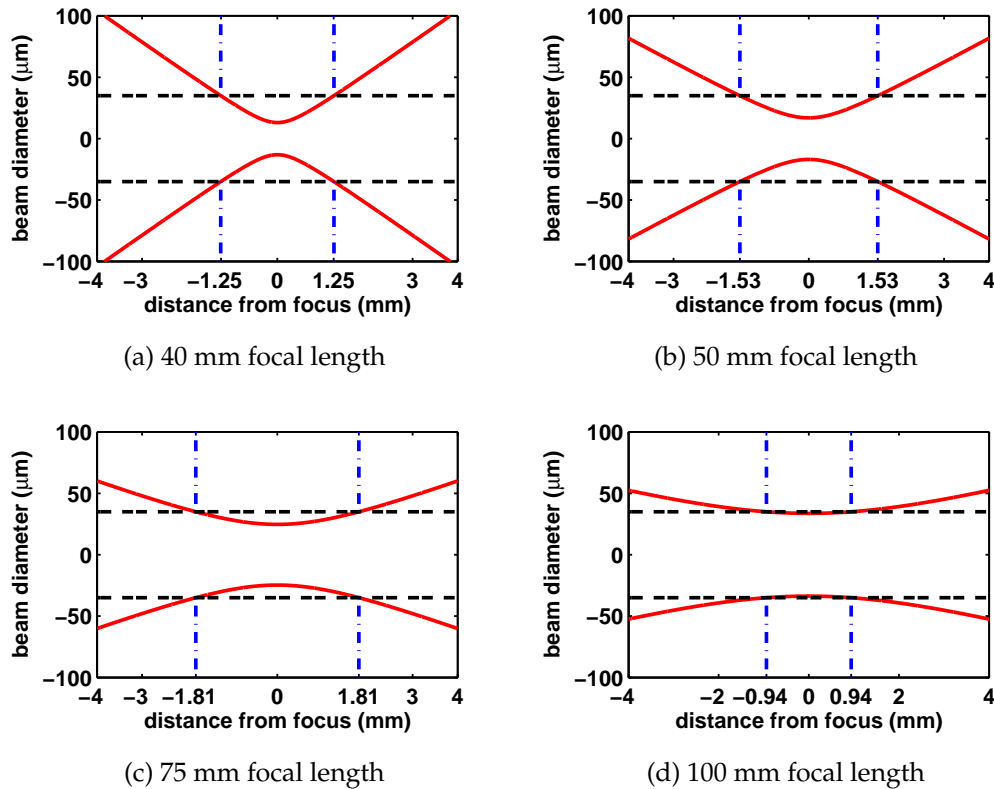


Figure 5.9.: Simulation of beam diameters behind lenses of different focal length.

#### 5.5.4. Cladding modes and pointing stability

Cladding modes in fibers can lead to apparent output beam angle fluctuations due to the higher order mode contents guided in the cladding of the otherwise single-mode fiber [69, 70]. This, in combination with the relatively small-area photo diodes used in this experiment, can lead to apparent phase fluctuations when different parts of the resulting multi-mode beam are not detected because part of the beam misses the detector.

One way to avoid or at least suppress cladding modes is to tightly bend the fiber, such that its bend radius approaches the minimum bend radius specified by the manufacturer. In this situation, the nominal fiber mode will still be guided, whereas the cladding modes are subject to large losses due to the larger minimum bend radius required to still guide light in the much wider cladding.

Therefore, the input fiber used in this experiment was tightly wound several times around a standard Thorlabs™ optical mount with a diameter of 24.5 mm. Although this is even slightly below the minimum bend radius of 30 mm given by the manufacturer of the fiber, no loss in optical power throughput was observed, thus allowing efficient attenuation in the cladding modes.

After implementing this simple cladding mode filter, measurements of the differ-

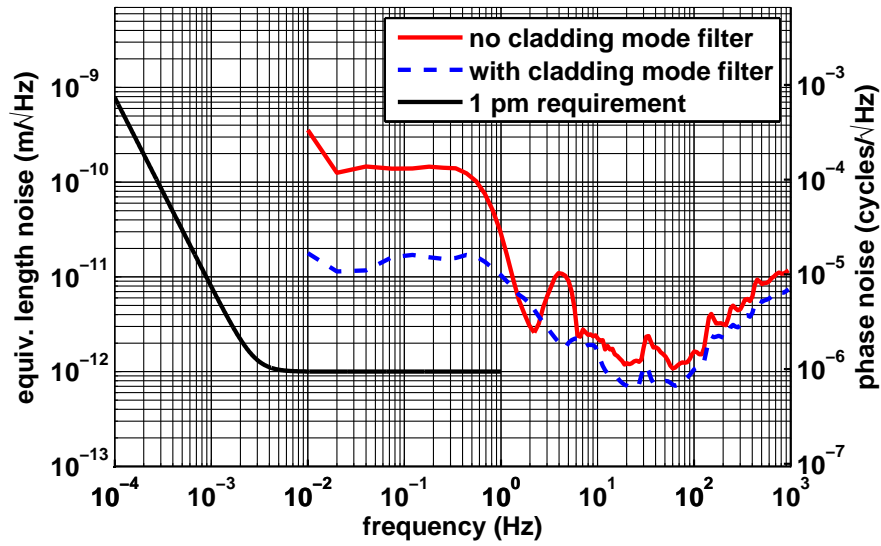


Figure 5.10.: Differential photo diode noise before and after removal of cladding modes by tightly winding the fibers around posts.

ential photo diode noise were repeated. A comparison of the measurements with and without cladding mode filtering can be found in Figure 5.10. Observing the red trace, which represents the differential photo detector noise without the cladding mode filter one finds that in this case a shoulder-shaped noise curve results. For frequencies between 10 mHz and 1 Hz the noise is at  $100 \text{ pm}/\sqrt{\text{Hz}}$ , dropping off steeply at 1 Hz to about  $1 \text{ pm}/\sqrt{\text{Hz}}$ . With the cladding mode filter installed, as represented by the blue curve, the shoulder shape remains, but the noise level for frequencies between 10 mHz and 1 Hz is reduced to only  $10 \text{ pm}/\sqrt{\text{Hz}}$ .

From this it can be concluded that some higher order mode content was present in the fibers delivering the light to the Zerodur<sup>TM</sup> optical bench, which could be filtered out by bending the fibers tightly. The effect of this higher order mode content seems to be worse when smaller photo diodes with higher bandwidths are used, as it was not observed using the relatively large photo diodes used in the previous experiment without Digitally enhanced Interferometry.

## 5.6. Conclusion

In this chapter, the changes to the non-reciprocity measurement setup necessary to allow the implementation of Digitally enhanced Interferometry (DI) were presented and described. All changes were successfully carried out such that first measurements using DI in fiber non-reciprocity could be conducted.

Measurement data showed excess noise, which led to follow-up investigations on the source of this noise. It was found that the photo detectors used for these

experiments, which require a higher bandwidth than the previously used ones. The differential photo detector noise has been measured and was found to be in violation of the 1 pm requirement, preventing low noise measurements.

Potential sources for this noise have been investigated, but it was not possible to reduce the differential photo diode noise below the requirement. However, the introduction of cladding mode filters by tightly winding the fiber with a small radius of curvature (30 mm) was found to reduce this noise source leading to the conclusion that at least some of the excess noise was caused by the higher order mode content in the fiber's output beam.

Unfortunately, it was not possible to further improve the sensitivity of the setup as the equipment had to be shipped back to the ANU for use there in other experiments and due to customs regulations. Therefore, it was not possible to reach the same sensitivity as in Chapter 3.

The non-reciprocal noise levels observed using DI are presented in Figure 5.11. Measurement results without the fiber installed are shown, resulting in a measurement of the non-reciprocal noise inherent to the measurement system. The solid red trace represents data from a measurement where the PRN code modulation for DI was switched on, while the dashed blue trace represents results from a measurement where the modulation was switched off, leading to a conventional heterodyne interferometric measurement. As can be seen, both noise spectral densities are far above the requirement. Both traces show a shoulder-like shape, with noise levels between 10 mHz and approximately 300 mHz of  $200 \text{ nm}/\sqrt{\text{Hz}}$ , dropping off steeply above 300 mHz to a level of approximately  $30 \text{ pm}/\sqrt{\text{Hz}}$  above 5 Hz.

From the fact that both trace are very close to each other one can conclude that the DI neither had a positive nor a negative impact on the measurement sensitivity at this level. The reason for the relatively high setup noise in this case is probably the lack of balanced detection or any other means of rejection of spurious reflections. As mentioned before, the modulation bandwidth was not sufficient to effectively suppress spurious reflections with a path length difference of less than 3.75 m with respect to the nominal interference signal. As typical distances in the experiment were shorter than this, the potential stray light rejection of DI was not effective here. Balanced detection could also not be implemented due to the lack of a sufficient number of high bandwidth, low noise photo detectors.

However, this does not mean that Digitally enhanced Interferometry is not applicable to the measurement of non-reciprocal noise or that the measurement sensitivity achievable with DI is necessarily worse that without it, but it just means that more investigations are necessary to identify suitable photo detectors and/or to increase the bandwidth of the modulation such that the rejection of spurious signals in the setup becomes possible. Unfortunately, this could not be accomplished during the time the phase meter and modulation electronics were available.

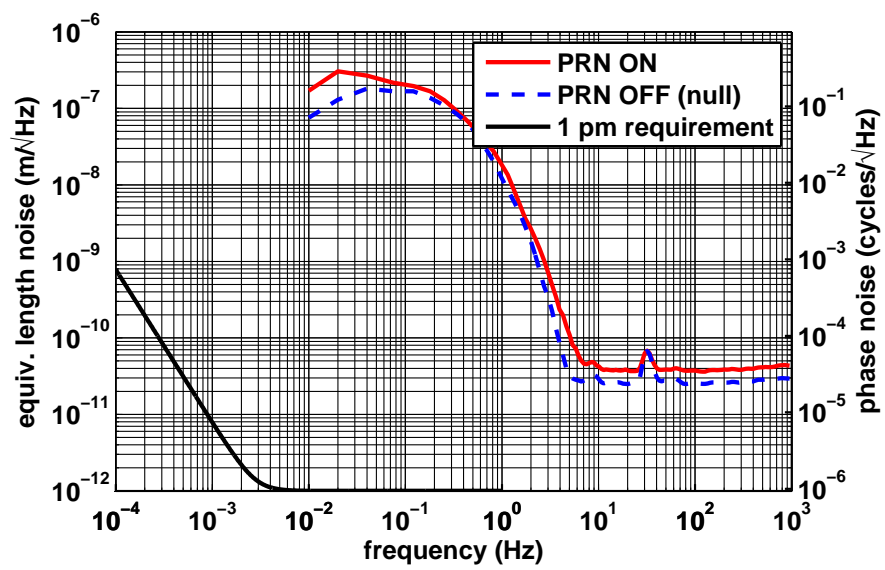


Figure 5.11.: Non-reciprocal noise observed using the digitally enhanced heterodyne interferometry setup.

## CHAPTER 6

---

## Consequences for the design of the LISA optical bench

---

The findings presented in the previous two chapters imply some consequences for the design of the LISA optical bench. These are discussed here in detail.

As described in Sections 3.6.1 and 4, the main source of non-reciprocal noise in the experiments was found to be spurious reflection off the fiber interface. An obvious way to mitigate this noise source would be to eliminate the source of the reflections by choosing special fibers with a very low reflection compatible with the requirements.

This, however, does not seem to be (easily) feasible. An investigation of a number of fibers with and without special treatment and design features to reduce reflections did not identify any potential candidates with a reflectivity compliant with the requirements. None of the investigated fibers showed a power reflection coefficient of less than 1 ppm [57], while in order to comply with the requirement a reflectivity of less than 1 part in  $10^{12}$  is required.

While it is not entirely impossible that such a fiber will be found in the future, it is still advisable to give some thought to possible other ways to facilitate a fiber back link with compatible performance for the mission under the premise that one has to deal with such a relatively high fiber reflectivity. Such possible mitigation paths and their impact on the mission are identified and described in the following sections. Advantages and disadvantages of the proposed solutions are discussed in the individual sections and a comparison can be found in the final section of this chapter.

### 6.1. Attenuation of stray light

A commonly used option when facing excess reflected stray light is to use attenuators in front of the reflective surface. This will reduce the power of the light

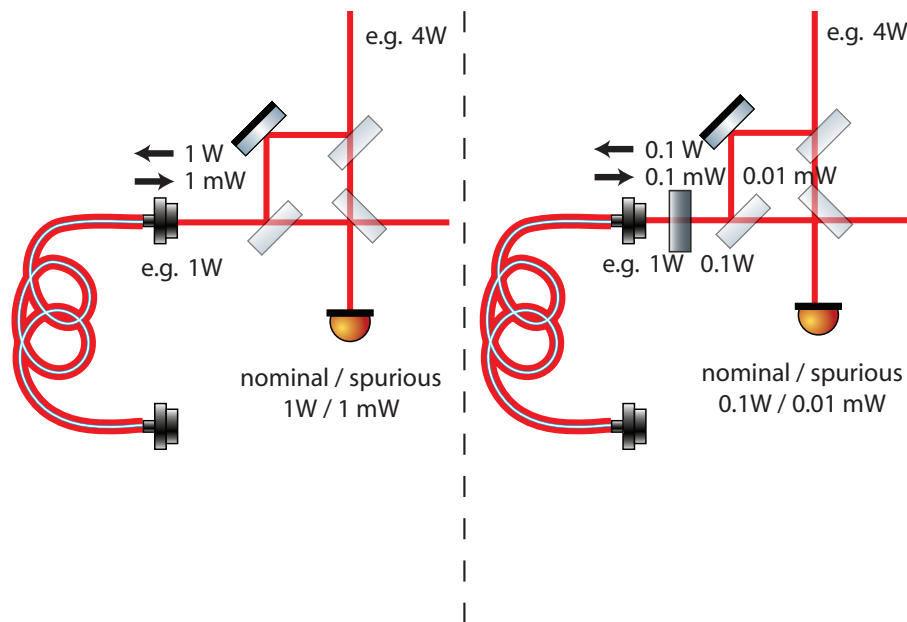


Figure 6.1.: Schematic showing the application of an attenuator to reduce spurious reflected beat notes. A transmission of 0.1 % is assumed for the attenuator.

entering the measurement but it will also attenuate the unwanted reflected signal again when passing through the attenuator from the opposite side as illustrated in Figure 6.1.

With the available high power laser and extremely sensitive photo diodes this seems an attractive option despite the high losses introduced by the attenuators. One could apply a lot of attenuation and still have a beat signal large enough to be easily measured by the photo diodes and the phase meter which are both capable of detecting pW-level signals.

However, it turns out that this technique is not applicable for the LISA backlink fiber, ironically because of its reciprocity (or more exactly, because of the reciprocity/symmetry of the setup). In a single-ended measurement, as indicated in Figure 6.1, it is possible to attenuate the input beam on one end independently of the input beam at the other end, thereby achieving the desired decrease in relative amplitude of the spurious reflection. If such a scheme is to be applied for the backlink fiber it would have to be implemented on both optical benches to reduce the effect of reflections occurring at either end.

As depicted in Figure 6.2, this will inevitably lead to a decrease in the amplitude of the desired beat note signal as well as in the amplitude of the spurious signal, thereby not gaining anything with respect to the suppression of spurious signals.

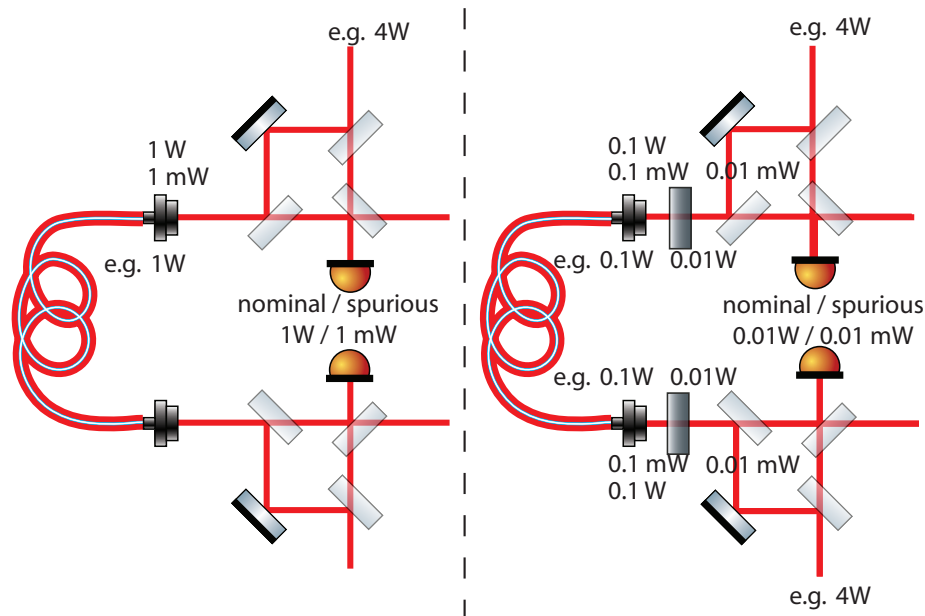


Figure 6.2.: Schematic showing the impossibility of spurious signal reduction using attenuators in the LISA backlink fiber. A transmission of 0.1 % is assumed for the attenuator.

## 6.2. Balanced detection

Balanced detection has been used in the course of this work to reduce the influence of spurious reflected beams on the measurement sensitivity as described in Section 3.6.1. Using this technique and the signals from both output ports of the recombination beam splitter, it is possible to drastically reduce the influence of spurious beat signals. While this can be done easily on the ground for testing purposes, the special requirements of a space mission – namely the requirement of tolerance against single-point failures – make this unattractive for use in LISA.

For a space mission it is required that it is still operable even with failures of some critical components. Often, such critical systems will be foreseen to be redundant in order to cover such failures. This means that photo diodes in both outputs of the recombination beam splitters are already planned in the design of the optical bench. It is envisaged to operate them in hot redundancy, using the sum of both photo diode signals in normal operation and just one of the two signals in case of failure of the other. This leads to a *graceful degradation* where the signal to noise ratio is only reduced by a factor of  $\sqrt{2}$  in case of failure of one of the diodes.

This is however not the case when using the photo diodes in a balanced detection scheme to cancel undesired spurious signals. Balanced detection requires both detectors to be operating in order to work as desired. A failure of one detector no longer leads to a degradation by  $\sqrt{2}$ , but immediately leads to a large degradation due to the loss of spurious signal reduction. Results presented in Section 3.6.1 show

that this would lead to an increase in observed noise levels by about three orders of magnitude, far too much to be still compliant with the requirements.

The only way to avoid this loss of redundancy is to install additional beam splitters in each output port of the recombination beam splitter and use two redundant photo diodes to sense the signals in each output port. This requires twice as many photo diodes as previously planned and also additional beam splitters and therefore much more room on the already crowded optical bench. It would also require twice as many phase meter channels, and therefore probably higher power consumption and increased complexity of the phase meter, all of which are very undesirable (but not impossible).

### 6.3. Direct stray light subtraction

As discussed previously, it is also possible to use a dedicated photo diode to detect and subtract spurious beat notes instead of an additional photo diode in each output of the recombination beam splitters.

Such a scheme is illustrated in Figure 6.3 for the LISA optical bench. Such an additional photo detector would also have to be redundant, therefore a beam splitter and a second photo detector are required if this scheme is to be applied in LISA. Interestingly enough, one detector is already foreseen on the optical bench which could take this role. So far, it has been planned to be used as an amplitude monitoring and stabilization photo detector, but it could easily be converted to a proper LISA phase measurement photo detector, without sacrificing the amplitude monitoring part. The only arguable downside of this solution is that this detector then serves two purposes and a failure of this detector would affect two subsystems, the amplitude stabilization and the stray light correction. Still, this detector would not have to be considered a potential single point of failure, as it is already foreseen to be redundant.

Taking the results discussed in Section 3.5.4 into account, this detector would enable the monitoring of stray light beat notes to either subtract them (in post processing or directly on the space craft) or to use the signal in a scheme very similar to the one presented in this thesis to cancel the stray light signal.

This approach would require an increase in the bandwidth of the power monitor photo diode. Currently, the requirements on the power monitor photo diode only extend to 1 kHz [24], which would have to be increased to up to 20 MHz, such that it also fulfills the same requirements as all other photo diodes, on top of the power monitor requirements. While such detectors are obviously available due to their use in the interferometers, they are somewhat larger than the power monitor and hence they require some additional space on the optical bench. Still, the additional amount of space required for this approach is much smaller than having to double the number of photo detectors in each interferometer as discussed in the previous section.

The main advantage of this concept over balanced detection is the lower number



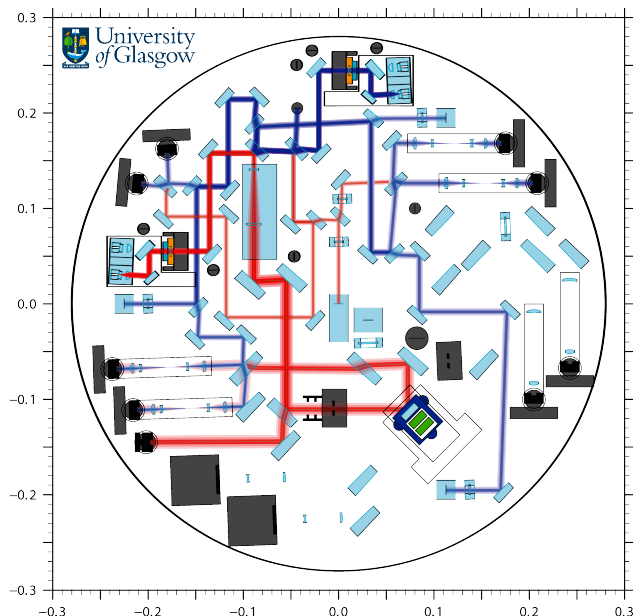


Figure 6.3.: Schematic of the current design of the *elegant breadboard*, a possible implementation of a LISA optical bench for testing purposes, to be manufactured in the frame of the LISA optical bench contract. All beams affected by stray light are shown together with the power monitor photo detector and beam path. Combination of images kindly provided by The University of Glasgow.

of additional components required. In the balanced detection scheme, the number of photo detectors has to be doubled in each interferometer potentially affected by the spurious beat signals. The signals from the dedicated stray light detectors can be used to subtract spurious beat notes in all interferometers “downstream” of them. Therefore, if only one interferometer is potentially affected by stray light, both methods are equally involved. However, it can be beneficial to use the dedicated detectors if more than one interferometer is facing the same stray light problems.

Close examination of the current design of the LISA optical bench, as developed in the frame of the LISA optical bench contract by European Space Agency (ESA), reveals that ghost beams from the back link fiber injectors arrive at several photo detectors and can indeed influence the measurements in several interferometers. All interferometers using light from the other optical bench as one part of the interference are affected:

- Reference interferometer
- Test mass interferometer
- point-ahead angle mechanism (PAAM) metrology interferometer
- All three optical truss interferometers (though the effect may be smaller due to the different polarization used)

Interestingly enough, the science interferometer is not affected. While at first this seems to indicate that the objective of LISA is therefore not endangered, this is unfortunately not the case, because a combination of the test mass, reference and science interferometer is required in the “split interferometer” architecture to measure the distance variations between the test masses on two satellites.

## 6.4. Measurement of the reflection signal

Using the additional photo detector discussed in the previous section, it is possible to suppress the ghost beams by using the detected spurious beat note in a feedback loop and applying its feedback signal to the light source or via a suitable modulator, e.g. an electro-optic amplitude modulator to cancel the spurious signal.

Similarly, it should also be possible to measure the spurious signal directly and to correct for its effect in data post processing on board the satellite. This was also attempted in the non-reciprocity experiment, as discussed in detail in Section 3.6.1. However, this achieved only limited success.

Depending on the reason for failure in the attempts to directly measure the reflected light, it could still be possible to apply this technique. Similarly to the technique discussed in the previous section, it has the benefit of only requiring one set of additional redundant photo diodes to correct for the spurious signals present in the science, test mass and PAAM metrology interferometers, as well as in the optical truss interferometers.

Application of this technique would however still require that it be verified in detailed tests prior to the final decision on the actual technique to be used. Ideally, this could be performed on the elegant breadboard manufactured as part of the LISA optical bench contract. It features all relevant interferometers as well as an additional power monitor/stabilization photo diode which could be enhanced or replaced by a phase-measurement photo diode with higher bandwidth and could hence be used in such tests.

## 6.5. Digitally enhanced heterodyne interferometry

Another method to overcome the influence of stray light on the phase measurement in the local interferometers would be to use a sophisticated modulation technique to enable its detection and subtraction. One candidate modulation technique for this purpose has been tested in the course of this work, i.e. digitally enhanced heterodyne interferometry. As has been discussed already in Section 5, it could be implemented in LISA without (much) additional hardware, the main changes would be in the software of the phase meter and in the application of the necessary modulation. However, it should be noted that digital interferometry has so far not been tested at the picometer level in the presence of strong stray light.

Furthermore, the codes to be used to enable digitally enhanced interferometry are very similar to the codes which are to be used for absolute distance measurements between the satellites detailed in e.g. [63]. Thorough testing is required to ensure that the codes do not interfere with each other and that both techniques can be applied simultaneously without reducing the performance of either one.

A third open point is the increase in bandwidth required in both the phase meter and the photo detectors. So far, both these components are specified with a bandwidth compliant with the highest beat note frequency that is anticipated, which is in the range of 10 to maybe 40 MHz. These beat note frequencies stem from the fact that the operating principle of the interferometer is heterodyne interferometry. To avoid zero crossings of the beat note frequencies (which would prevent phase tracking of the phase meter), beat note frequencies have to be of the same magnitude as the Doppler shifts introduced by the relative motion of the satellites on their geodesic orbits. These Doppler shifts are computed to be up to 10 MHz for realistic orbits [6, 71].

If stray light subtraction by digitally enhanced interferometry is to work for the distances between stray light source and detector on an on-board optical bench with typical distances of the order of tens of centimeters, then this calls for modulation frequencies in the GHz range ( $c/0.1\text{m} \approx 3\text{ GHz}$ ). While modulators with such high bandwidths are readily available and are in fact foreseen to be used [64], the need for such high bandwidth is a strong driver in photo diode electronics development.

## 6.6. Discussion of the possible alternatives

Taking into account the results from the previous sections, it becomes clear that some alternatives are more appealing, while others are either too complex or not tested well enough to be considered for a real mission in the 2020 to 2025 time frame<sup>1</sup>.

The simplest approach – to attenuate the stray light using neutral density filters – has unfortunately been found to be inapplicable due to the shared paths of all relevant beams, as discussed in Section 6.1. This prevents the selective attenuation of reflected light while preserving the transmitted light.

The second alternative discussed here is balanced detection. This technique is well proven and has been used in many applications. In the experiments presented in this work it has been applied successfully for the removal of stray light from the measurements. The main disadvantage of this technique in a real space mission is that it compromises the failure tolerance required in such a mission. In order to restore single point of failure tolerance, the number of photo detectors on the optical bench would have to be doubled. This would also increase space required on the optical bench, and it would significantly increase the number of phase

---

<sup>1</sup>This is the launch data currently planned for LISA, but of course this could change due to unforeseen circumstances like those discussed in [72, 73, 74, 75, 76].

meter channels required and the overall power consumption of the satellite. All of these are scarce resources on board a satellite, which makes this option appear unattractive, though viable.

The direct stray light subtraction, discussed in Section 6.3, promises to reduce the number of additional photo detectors required to only one, or possibly even none, if the existing amplitude stabilization detector can be changed to allow sensitive phase measurements in the relevant frequency range. However, this technique has not been tested extensively so far, but it has only been demonstrated to work once. It is not clear if this technique will work as expected, and hence more testing is required, ideally on a prototype optical bench model. The same is true if one wants to measure and subtract the stray light signal as discussed in Section 6.4. This technique is even a little more challenging, because it requires an additional high bandwidth amplitude modulator.

Finally, Digitally enhanced Interferometry (DI) could also be applied for the rejection of the signals caused by spurious reflections. While the optical components that are required for this technique are all foreseen on the satellite anyway, it requires photo detectors with a much larger bandwidth if stray light rejection is to work despite the small travel time differences between spurious and nominal beam. Taking into account that the photo detector development is already a challenging task, even with the relatively benign requirement of 20 MHz bandwidth, this option does not seem to be viable.

---

## Other potential applications

---

### 7.1. Rotation calibration using the Sagnac-effect

As mentioned in the beginning of this thesis (cf. Section 2.1) the Sagnac-effect leads to a genuinely non-reciprocal phase shift that is measured in the non-reciprocity experiment. While this is considered as a noise source in the context of these measurements, it can also be useful under certain circumstances. For example, the Sagnac-effect can be used to calibrate the experiment.

While heterodyne interferometric measurements generally do not rely on calibration – because the phase can be measured and tracked very well even over large ranges – it is useful to compare the results achieved in a calibration measurement to the expected results as a kind of sanity check.

When one expects to measure a null result it is always comforting to be able to check whether a genuine non-reciprocity is sensed the way it is expected, because otherwise it can easily happen that through a small flaw or mistake, a channel which is insensitive to non-reciprocal noise is measured and thereby the noise floor is underestimated. In such a situation it is normally hard to establish confidence in the results because a non-functional measurement could potentially look very favorable and contain low noise. Luckily, a confirmation measurement using a rotating fiber and the non-reciprocal Sagnac-effect allows one to check the correct operation of the experiment because results can be predicted reliably and compared to the measurements.

To facilitate a rotation calibration in the non-reciprocity experiment it was necessary to introduce a known non-reciprocal signal. This was achieved by mounting the fiber spool on a movable platform driven by a motor. A piston and a joint changed the rotational motion of the motor into a back-and-forth rotation of the platform, as illustrated in Figure 7.1.

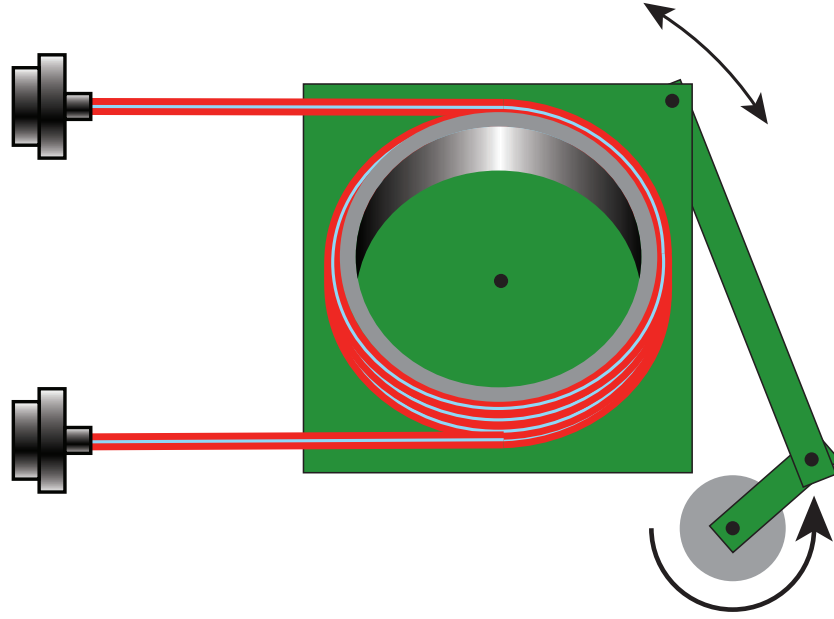


Figure 7.1.: Mechanism used to rotate the fiber back and forth.

Using this mechanism it was possible to rotate the fiber back and forth at different angular velocities by changing the motor's driving voltage and thereby the rotational speed of its axis. The amplitude of the motion is approximately a quarter of a full revolution, while the angular velocity could be varied. Measurements were taken at fixed input voltage and therefore (peak) angular velocity for many cycles. Data was then analyzed in the frequency domain where a peak at the repeating frequency of the rotational motion could be observed with a magnitude corresponding to the angular velocity of the motion.

From the period of the back and forth motion corresponding to the location of the peak on the frequency axis, the angular velocity and therefore the expected peak height can be calculated. Using the known rotation amplitude of approximately a quarter rotation, the angular velocity of the rotation,  $\Omega$ , can be calculated from the frequency  $f_{\text{rot}}$  as  $\Omega = \pi f_{\text{rot}}/2$ .

The non-reciprocal phase-shift  $\delta_{\text{Sagnac}}$  is proportional to the angular velocity  $\Omega$  and the area  $A$  enclosed by the fiber, according to the formula derived in [8]:

$$\delta_{\text{Sagnac}} = \frac{8\pi A\Omega}{\lambda_0 c}$$

Here,  $\lambda_0$  denotes the laser wavelength in vacuum and  $c$  is the speed of light in vacuum.

In our case, the fiber was wound 25 times around a ring piezo of 80 mm diameter. This results in an overall area of  $25\pi r^2 \approx 0.126 \text{ m}^2$ , corresponding to a phase shift of  $9.9 \text{ ms}/\Omega$ , i.e. a phase-shift of 9.9 mrad at an angular velocity of 1 rad/s. At a

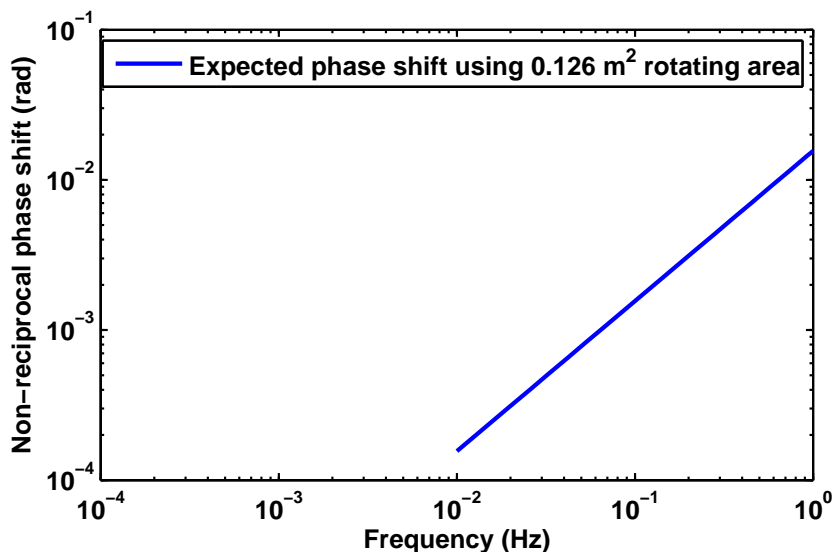


Figure 7.2.: Expected amplitude of Sagnac phase shift versus rotation frequency of the fiber rotation mechanism.

given noise floor of about  $6 \mu\text{rad}/\sqrt{\text{Hz}}$  this would allow rotation measurements at angular velocities down to the mrad/s level.

Combining the above two derivations, one can compute the expected phase shift for a given rotational frequency as

$$\delta_{\text{Sagnac}}(f_{\text{rot}}) = \frac{8\pi^2 A f_{\text{rot}}}{2\lambda_0 c}$$

This is plotted in Figure 7.2 for realistic frequencies using the motor and voltage source available.

Figure 7.3 shows the spectrum of a measurement taken while the mechanism was running and rotating the fiber back and forth. When comparing the observed spectrum of the non-reciprocal phase to the expected non-reciprocal phase shift from the rotation one sees that the observed amplitude matches the expected phase shift perfectly. This nicely confirms the accuracy and validity of the non-reciprocal phase measurements.

## 7.2. Heterodyne Sagnac interferometry

The ability to measure non-reciprocal length changes with high resolution and low noise enables the measurement of non-reciprocal phase shifts introduced by the Sagnac-effect, discussed in detail in Section 2.1.

The availability of high quality optical fibers and light sources led to the implementation of many different sensors using the Sagnac-effect, including, but not

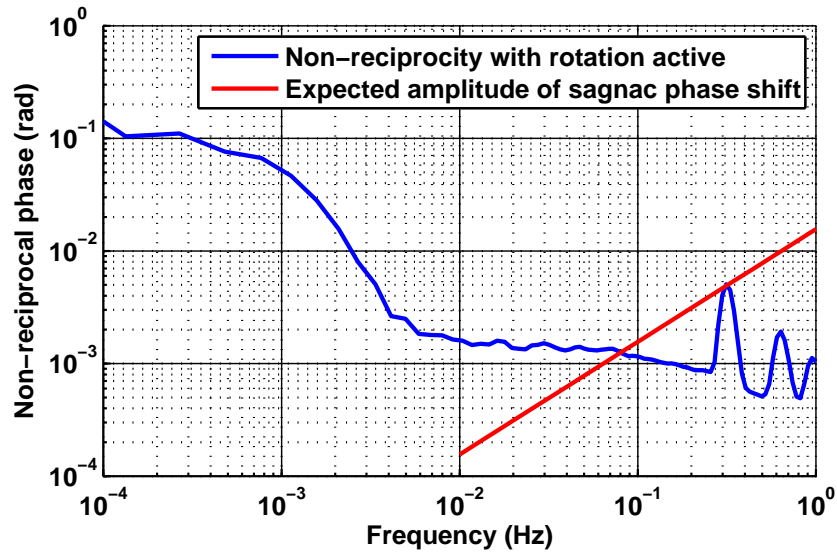


Figure 7.3.: Spectrum of non-reciprocal signal as observed during back and forth rotation of the fiber at 0.3 Hz.

limited to: current sensing; voltage measurement [17, 77]; and of course rotation measurements for navigational purposes.

Usually, the readout of the non-reciprocal phase in these sensors is implemented using a different technique, often involving low coherence length light sources to avoid the effects of reflected light and modulation techniques to enable phase readout.

The heterodyne readout used in this work has the potential advantage of providing a means of measuring continuously over several wavelengths, tracking large phase shifts unambiguously and avoiding the use of modulators in the non-reciprocal path.

Previous approaches to implement heterodyne interferometric readout of Sagnac phase shifts, like the one described in [78], achieved rotation rate measurements of  $\approx 100 \text{ deg/h} \equiv 0.4 \text{ mrad/s}$ . Apparently, this has not been further investigated due to the better performance of other approaches.

Still, the approach used in this work seems to be unique, probably due to the fact that it adheres to the design constraints set by the requirements of a space-based gravitational wave detection mission. However, the phase readout performance achieved here is at least comparable to the  $10^{-7} \text{ rad}$  quoted in [8], which should make it possible to implement fully heterodyne readout of fiber optic Sagnac interferometers.

To achieve useful rotation rate sensitivity, the fiber length would have to be increased to allow a larger area and thus a higher sensitivity to induced non-reciprocal phase changes. Using the sensitivity found here, and assuming that a fiber of 1 km length wound on a coil of 30 cm diameter could be added to the setup



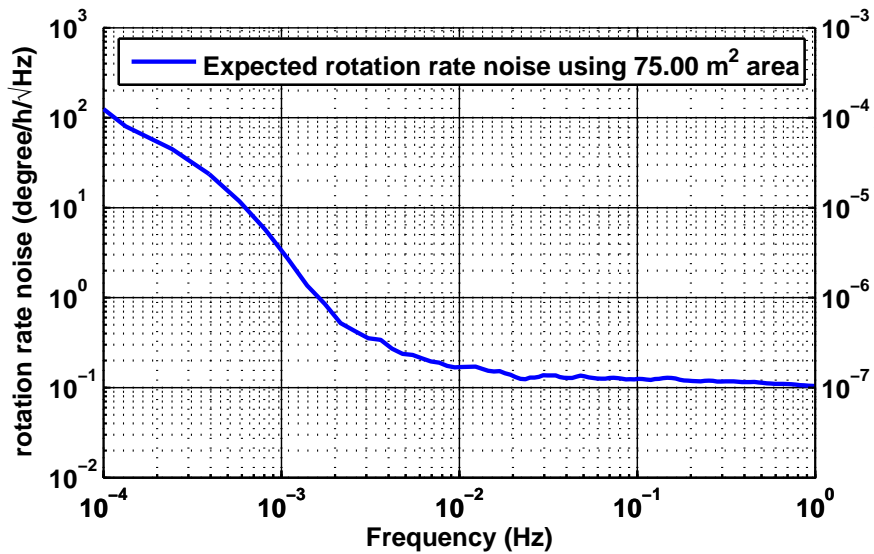


Figure 7.4.: Projected rotation rate noise floor assuming the demonstrated non-reciprocal phase noise levels and a fiber length of 1 km wound on a spool with 30 cm diameter, resulting in an area of approximately 75 m<sup>2</sup>.

without compromising measurement sensitivity, a rotation rate noise floor of 0.1 degree/hour should be achievable.

The projected rotation rate noise floor is shown in Figure 7.4. Rotation noise levels are computed to be around 0.1 degree per hour per  $\sqrt{\text{Hz}}$  for frequencies between a few mHz and 1 Hz, increasing as  $1/f^2$  toward lower frequencies.



The main goal of this work was to investigate the applicability of single-mode, polarization-maintaining fibers on board a future space-based gravitational wave observatory. The main concern here is that such fibers could potentially introduce non-reciprocal noise which will spoil the very sensitive length measurements necessary for the observation of gravitational waves.

Therefore, an interferometric measurement system was developed and presented that is capable of measuring the non-reciprocal noise of optical fibers under realistic conditions expected to be present on board a satellite for gravitational wave detection.

This setup is representative of the relevant section of a potential optical bench to be installed on such a satellite. Special care was taken to use the same materials (i.e. Zerodur™ for the base plate and fused silica for the optics) that would be used in such a mission and the whole setup was built using hydroxide catalysis bonding to provide a quasi-monolithic interferometer with high mechanical stability.

This setup was characterized in terms of its own non-reciprocal noise, which ultimately limits its measurement performance. In the course of these measurements a number of noise sources were identified and techniques for their removal were developed and applied. The main source of measurement error was found to be spurious reflections from the fiber, leading to distorted measurement signals.

To overcome this problem, additional readout channels were installed, enabling the use of a data post processing technique capable of suppressing these unwanted signals. This technique was applied successfully in the measurements and led to a noise reduction of two orders of magnitude.

Along with this technique, several other ways to mitigate this problem have been proposed and tested, and their respective advantages and disadvantages for the application in a gravitational wave detection mission were presented and discussed.

One of these techniques, namely digitally enhanced heterodyne interferometry, was investigated in more detail, in collaboration with the Australian National University (ANU). Despite the fact that it could not be verified to provide the necessary sensitivity and noise suppression due to technical problems, this has led to a first hands on experience with this potentially very useful technique. Many experiments could benefit from its advantages of spurious signal reduction and parallel measurement of several length changes with just one detector.

Additionally, a special setup was developed and implemented that was capable of identifying the origin and amplitude of spurious reflections under realistic conditions. This was used to investigate several candidate optical fibers in terms of their spurious reflections. Measurements performed using this setup revealed that the power reflectivity of single-mode polarization maintaining fibers varies between approximately 4 ppm to 40 ppm for different fibers, with some extreme cases where up to 0.1 % power reflectivity were observed. Additionally it was found that reflections do not only occur at the fiber interface, but that Rayleigh scattering in the fiber is responsible for a major part of the returned light amplitude. This means that reflected light cannot be removed by spatial filtering in the reverse direction, as it shares the same spatial mode as the transmitted beam.

Finally, using the noise reduction techniques identified in the course of this work, measurements on a potential optical fiber for use in a space-based gravitational wave detection mission were made and it was shown that the non-reciprocal noise is in compliance with the strict requirements of  $1 \text{ picometer} / \sqrt{\text{Hz}}$ .

## APPENDIX A

---

## POV-Ray output extension for IFOCAD

---

IFOCAD is a software package developed by Gerhard Heinzl et al. to assist in the design process of complex interferometers; especially those built using permanent bonding, where careful planning is of utmost importance. To this end IFOCAD provides a number of functions that enable the parametrization of the interferometer in terms of path lengths, angles or distances [43].

IFOCAD partially extends the possibilities of OptoCad [44] to a three-dimensional space and is able to use OptoCad as a back-end for the generation of graphical representations of the optical setup. Due to this use of an interface for the generation of graphical output, it was possible to extend and modify the interface to allow the use of a different program for the generation of the graphical output.

Because IFOCAD brings with it the possibility to use three-dimensional coordinates in the simulation, a back-end capable of producing three dimensional graphical representations from scripted input would lend itself ideally to this task. Fortunately, with POV-Ray such a tool readily exists and is even available under an open-source license [45]. The remaining work to be done is restricted to the definition of such an interface, allowing IFOCAD to communicate with the ray-tracing back-end. The result can be found in the following code-snippet.

```
1 void
2 povbs (beamsplitter * bs, FILE * fp)
3 {
4     double x, y, z, width, height, thickness, angle, r1, r2;
5     x = 1e-1 * bs->s.zen[0];
6     y = 1e-1 * bs->s.zen[1];
7     z = 1e-1 * bs->s.zen[2];
8     width = 1e-1 * bs->s.rs * 2;
9     height = 1e-1 * 20;
10    thickness = 1e-1 * bs->d;
```

```

11 angle = atan2 ((-bs->s.nv[1]), (-bs->s.nv[0])) / DEGREE;
12 r1 = 1e-1 * bs->s.k;
13 r2 = 1e-1 * bs->k2;
14 printf ("%3f,%3f", r1, r2);
15 if (r1 == 0)
16     {
17         if (r2 == 0)
18         {
19             fprintf (fp,
20                 "object{box{<-.5*%3f,-.5*%3f,0>,<.5*%3f,.5*%3f,*%3f>}\n",
21                 width / 2, height / 2, width / 2, height / 2, thickness);
22             fprintf (fp, "_____translate_z*%3f\n", thickness / 2);
23             fprintf (fp, "_____rotate_y*%3f\n", angle);
24             fprintf (fp, "_____translate_x*%3f\n", x);
25             fprintf (fp, "_____translate_z*%3f\n", y);
26             fprintf (fp, "_____translate_y*%3f\n", 4 + height / 2);
27             fprintf (fp, "_____}\n\n");
28         }
29         else if (r2 < 0)
30         {
31             fprintf (fp, "object{\n");
32             fprintf (fp, "_____difference_{\n");
33             fprintf (fp, "_____box_{<-%3f,-%3f,0>,<%3f,%3f,%3f>}\n",
34                 width / 2, height / 2, width / 2, height / 2,
35                 thickness - r2);
36             fprintf (fp, "_____sphere_{<0,0,%3f>,%3f}\n", thickness - r2,
37                 -r2);
38             fprintf (fp, "____}\n");
39             fprintf (fp, "_____translate_x*%3f\n", x);
40             fprintf (fp, "_____translate_z*%3f\n", y);
41             fprintf (fp, "_____translate_y*%3f\n", 4 + height / 2);
42             fprintf (fp, "____}\n");
43         }
44         else if (r2 > 0)
45         {
46             fprintf (fp, "object{\n");
47             fprintf (fp, "_____intersection_{\n");
48             fprintf (fp, "_____box_{<-%3f,-%3f,0>,<%3f,%3f,%3f>}\n",
49                 width / 2, height / 2, width / 2, height / 2,
50                 thickness + r2);
51             fprintf (fp, "_____sphere_{<0,0,%3f>,%3f}\n", thickness - r2,
52                 r2);
53             fprintf (fp, "____}\n");
54             fprintf (fp, "_____translate_x*%3f\n", x);
55             fprintf (fp, "_____translate_z*%3f\n", y);
56             fprintf (fp, "_____translate_y*%3f\n", 4 + height / 2);

```

```

57     fprintf (fp, "}\n");
58 }
59 }
60 else if (r1 < 0)
61 {
62     if (r2 == 0)
63 {
64     fprintf (fp, "object{\n");
65     fprintf (fp, "_____difference_{\n");
66     fprintf (fp,
67         "_____box_{<-%.3f,-%.3f,-%.3f>,<%.3f,%.3f,%.3f>\n",
68         width / 2, height / 2, -r1, width / 2, height / 2,
69         thickness);
70     fprintf (fp, "_____sphere_{<0,0,%.3f>,%}.3f}\n", r1, -r1);
71     fprintf (fp, "____}\n");
72     fprintf (fp, "____translate_x*%.3f\n", x);
73     fprintf (fp, "____translate_z*%.3f\n", y);
74     fprintf (fp, "____translate_y*%.3f\n", 4 + height / 2);
75     fprintf (fp, "}\n");
76 }
77 }
78     else if (r2 < 0)
79 {
80     fprintf (fp, "object{\n");
81     fprintf (fp, "_____difference_{\n");
82     fprintf (fp,
83         "_____box_{<-%.3f,-%.3f,-%.3f>,<%.3f,%.3f,%.3f>\n",
84         width / 2, height / 2, -r1, width / 2, height / 2,
85         thickness - r2);
86     fprintf (fp, "_____sphere_{<0,0,%.3f>,%}.3f}\n", r1, -r1);
87     fprintf (fp, "_____sphere_{<0,0,%.3f>,%}.3f}\n",
88         -r2 + thickness, -r2);
89     fprintf (fp, "____}\n");
90     fprintf (fp, "____translate_x*%.3f\n", x);
91     fprintf (fp, "____translate_z*%.3f\n", y);
92     fprintf (fp, "____translate_y*%.3f\n", 4 + height / 2);
93     fprintf (fp, "}\n");
94 }
95     else if (r2 > 0)
96 {
97     fprintf (fp, "object{\n");
98     fprintf (fp, "_____intersection_{\n");
99     fprintf (fp, "_____difference_{\n");
100    fprintf (fp,
101        "_____box_{<-%.3f,-%.3f,-%.3f>,<%.3f,%.3f,%.3f>\n",
102        width / 2, height / 2, -r1, width / 2, height / 2,

```

```

103     thickness);
104     fprintf (fp, "_____sphere_{<0,0,%.3f>,%}.3f}\n", r1, -r1);
105     fprintf (fp, "_____}\n");
106     fprintf (fp, "_____sphere_{<0,0,%.3f>,%}.3f}\n",
107             -r2 + thickness, r2);
108     fprintf (fp, "_____}\n");
109     fprintf (fp, "___translate_x*%.3f\n", x);
110     fprintf (fp, "___translate_z*%.3f\n", y);
111     fprintf (fp, "___translate_y*%.3f\n", 4 + height / 2);
112     fprintf (fp, "}\n");
113 }
114 }
115 else if (r1 > 0)
116 {
117     if (r2 == 0)
118     {
119         fprintf (fp, "object{\n");
120         fprintf (fp, "_____intersection_{\n");
121         fprintf (fp, "_____box_{<-%.3f,-%.3f,0>,<%.3f,%.3f,%.3f>}\n",
122                 width / 2, height / 2, width / 2, height / 2, thickness);
123         fprintf (fp, "_____sphere_{<0,0,%.3f>,%}.3f}\n", r1, r1);
124         fprintf (fp, "_____}\n");
125         fprintf (fp, "___translate_x*%.3f\n", x);
126         fprintf (fp, "___translate_z*%.3f\n", y);
127         fprintf (fp, "___translate_y*%.3f\n", 4 + height / 2);
128         fprintf (fp, "}\n");
129     }
130 }
131 else if (r2 < 0)
132 {
133     fprintf (fp, "object{\n");
134     fprintf (fp, "_____difference_{\n");
135     fprintf (fp, "_____intersection_{\n");
136     fprintf (fp, "_____box_{<-%.3f,-%.3f,0>,<%.3f,%.3f,%.3f>}\n",
137             width / 2, height / 2, width / 2, height / 2,
138             thickness - r2);
139     fprintf (fp, "_____sphere_{<0,0,%.3f>,%}.3f}\n", r1, r1);
140     fprintf (fp, "_____}\n");
141     fprintf (fp, "_____sphere_{<0,0,%.3f>,%}.3f}\n", -r2 + thickness,
142             -r2);
143     fprintf (fp, "_____}\n");
144     fprintf (fp, "___translate_x*%.3f\n", x);
145     fprintf (fp, "___translate_z*%.3f\n", y);
146     fprintf (fp, "___translate_y*%.3f\n", 4 + height / 2);
147     fprintf (fp, "}\n");
148 }

```



```

149     else if (r2 > 0)
150     {
151         fprintf (fp, "object{\n");
152         fprintf (fp, "_____intersection_\n");
153         fprintf (fp,
154             "_____box_{<-.3f,-.3f,-.3f>,<.3f,.3f,.3f>\n",
155             width / 2, height / 2, r1, width / 2, height / 2,
156             thickness);
157         fprintf (fp, "_____sphere_{<0,0,.3f>,.3f}\n", r1, r1);
158         fprintf (fp, "_____sphere_{<0,0,.3f>,.3f}\n",
159             -r2 + thickness, r2);
160         fprintf (fp, "_____}\n");
161         fprintf (fp, "___translate_x*%.3f\n", x);
162         fprintf (fp, "___translate_z*%.3f\n", y);
163         fprintf (fp, "___translate_y*%.3f\n", 4 + height / 2);
164         fprintf (fp, "}\n");
165     }
166 }
167 }
168
169 void
170 povpbs (pbscube * pbs, FILE * fp)
171 {
172     double x, y, z, width, height, thickness, angle;
173     x = 1e-1 * pbs->s.zen[0];
174     y = 1e-1 * pbs->s.zen[1];
175     z = 1e-1 * pbs->s.zen[2];
176     width = 1e-1 * pbs->s.rs * 2;
177     height = 1e-1 * 20;
178     thickness = 1e-1 * pbs->s.rs * 2;
179     angle = atan2 ((-pbs->s.nv[1]), (-pbs->s.nv[0])) / DEGREE;
180     fprintf (fp, "object{box_{<-.5,-.5,-.5>,<.5,.5,.5>_\n");
181     fprintf (fp, "_____scale_{<.3f,.3f,.3f>\n", width, height, thickness);
182     fprintf (fp, "_____translate_z*%.3f\n", thickness / 2);
183     fprintf (fp, "_____rotate_y*%.3f\n", angle + 90 + 180);
184     fprintf (fp, "_____translate_x*%.3f\n", x);
185     fprintf (fp, "_____translate_z*%.3f\n", y);
186     fprintf (fp, "_____translate_y*%.3f\n", 4 + height / 2 - 1e-3);
187     fprintf (fp, "_____}\n\n");
188 }

```

Two functions are provided, which replace the equivalent functions for OptoCad output implemented in IFOCAD. They write the POV-Ray code for generation of the equivalent optics to a special file, that can later be included in a POV-Ray scene to render a photo-realistic graphical representation of the interferometer.

One example of such a scene is presented in Figure 3.16. A comparison to an actual photograph of the interferometer shown in Figure 3.17 reveals the impressive capabilities of POV-Ray at the generation of photo-realistic images of simulated objects.

It should be noted that not much attention has been paid to detail in the graphical representation of the optics in POV-Ray. For example, it would be easily possible to add chamfers to all edges of the components, which would greatly enhance their realism. However, as this extension was only planned to be used for a single application in the course of this work (namely to render the representation of the non-reciprocity interferometer), it was decided that it was not worth this extra effort. Given enough time and interest for the application in the design of further interferometers, it would also be advisable to make the interface more versatile and configurable, e.g. to include more types of optics typically used in interferometers or even add template scenes to also allow a photo-realistic rendering of conventionally built interferometers after the simulation.

Another potential extension of IFOPov would be the implementation of automatic generation of beams. The optical beams shown in Figure 3.16 were added manually after the automatic generation of the optical components using IFOCAD. It is, however, conceivable that an interface be implemented for tracing of the optical beam. Currently, this is somewhat cumbersome, because each individual beam segment would have to be converted into a corresponding POV-Ray object by an additional line of code.

Figure A.1 shows another interferometer rendered using IFOPov, to show that it is easily applicable to all IFOCAD simulations. In this case, the *polifo* interferometer was chosen as an example, due to its relatively complex optical design. Again, a photograph of the same setup is shown in Figure A.2 for comparison.

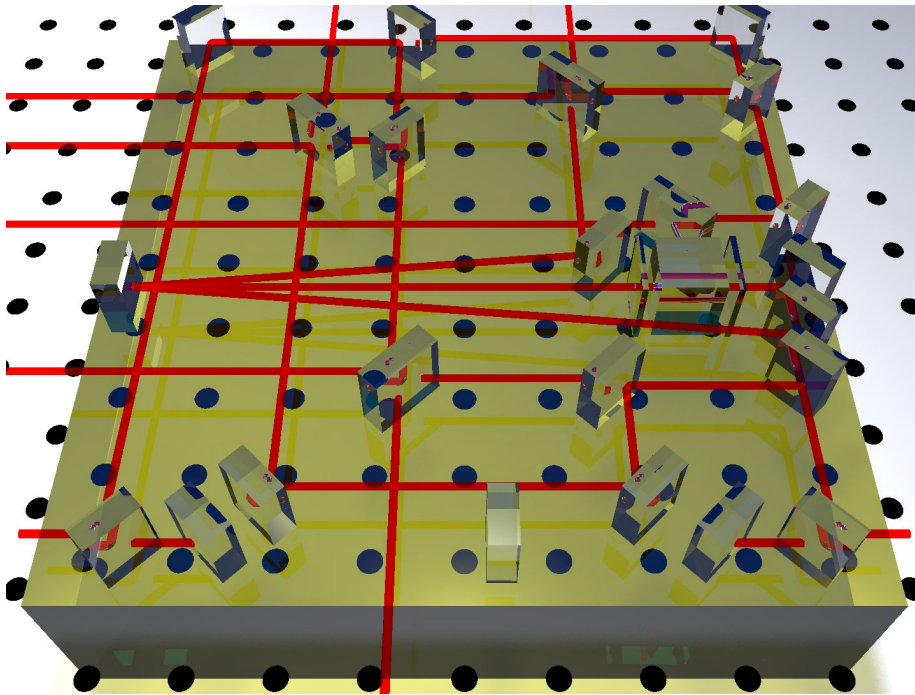


Figure A.1.: IFOPov rendering of *polifo* interferometer used to verify the feasibility of polarizing interferometry, design courtesy of Marina Dehne

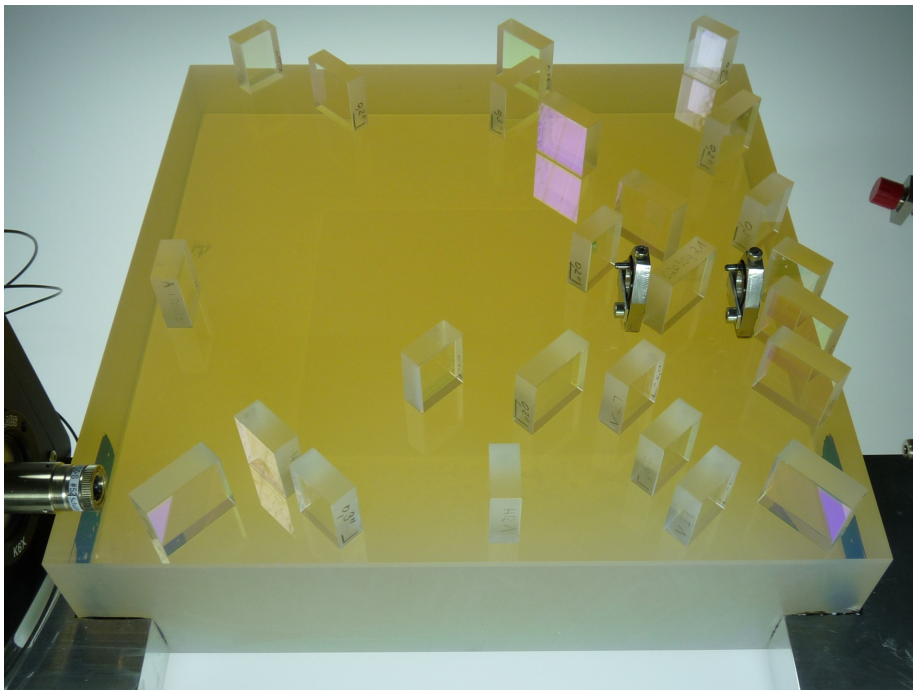


Figure A.2.: Photograph of the *polifo* interferometer after bonding, courtesy of Marina Dehne



---

 Matlab code to calculate bending of a Zerodur™ base plate
 

---

```

1 EYoung = 90.3E9; % 90.3 GPa
2
3 nu = 0.243; % poissons ratio , dimensionless
4
5 a = 0.2; %x dimension of plate in m
6 b = 0.2; %y dimension of plate in m
7
8 for H = 0.005:0.005:0.1
9     H
10    %H = 0.01; %z dimension of plate in m
11
12    D = H^3*EYoung/(12*(1-nu^2));
13
14    rho = 2.53e3; %density of Zerodur , kg/m^3
15    g = 9.81; %m/s^2
16    q0 = a*b*H*rho*g/(a*b); %Pa
17
18    result = zeros(steps , steps);
19
20    x= zeros(1 , steps);
21    y= zeros(1 , steps);
22
23    for xind = 1:steps
24        for yind = 1:steps
25            result(xind , yind) = 0;
26            x(xind) = (xind-1)/steps*a;
27            y(yind) = (yind-1)/steps*a;
28            for m = 1:100
  
```

```

29     for n = 1:100
30         result(xind,yind) = ...
31         result(xind,yind) + 16*q0 / ((2*m-1)*(2*n-1)*pi^6*D) ...
32         *( ( ( (2*m-1)^2)/a^2)+ ( (2*n-1)^2/b^2) )^-2 ...
33         *sin((2*m-1)*pi*x(xind)/a)*sin((2*n-1)*pi*y(yind)/b);
34     end %for n = 1:100
35     end %for m = 1:100
36     end %for yind = 1:steps
37     end %for xind = 1:steps
38
39     results{round(H*100*2)} = result;

```

---

## Proper treatment of optical fibers

---

When dealing with fibers in everyday lab life, some important points are often overlooked due to the ease of use of connectorized, polarization-maintaining, single-mode optical fibers. With the commercial availability of fiber-to-fiber couplers, fiber collimators and even integrated fiber beam splitters and modulators, it has become very easy to simply plug things together and get a working experiment. It is however very important to take care, especially of the interfaces. Despite their ease of use, they can be quite susceptible to contamination by dust and even damage, either from mistreatment or from thermal stresses introduced by high laser powers.

Furthermore, despite the fact that all components are typically polarization maintaining and come with an index that is meant to prevent polarization mis-alignment, it has to be kept in mind, that the alignment precision that is usually provided can be less than what is required in typical high precision experiments. While this can become a problem when using fiber-fiber interfaces and connectors, it becomes an even bigger issue when using free beam interfaces, where the polarization state of the incoming beam has to be matched to the fiber's axis with high precision. This procedure is particularly challenging as both entities to be matched are not visible or even easily accessible in the case of the fiber's axis. In summary, it can be quite easy to mess up the polarization unless very close attention is paid to this property.

### C.1. Polarization issues

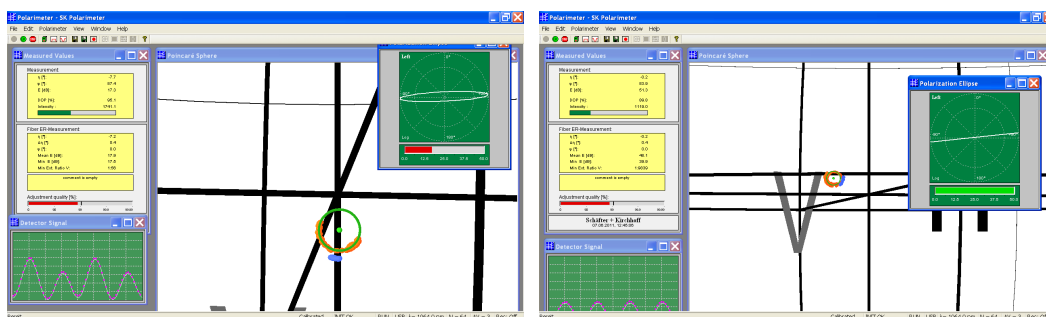
The polarization issue is illustrated in Figure C.1. Figure C.1a shows the main window of the polarimeter's computer display before any special alignment of the input polarization with respect to the fiber's axis was undertaken. The current

polarization state is shown in the polarization ellipse view in the upper right hand side of the picture, which indicates a fairly elliptical polarization state.

The main display shows the polarization state on the Poincaré sphere. Thanks to the special *extinction ratio* (ER) mode of the polarimeter, a circle is shown indicating all the polarization states that come from the fiber when it is heated or subjected to external stress, leading to arbitrary phase relationships between the two possible internal polarization states of the fiber. This circle is large in Figure C.1a, indicating a rather bad alignment if the fiber's polarization maintaining axis with respect to the input polarization.

The quality of the alignment is also indicated by the ER-bar directly under the polarization ellipse view on the right hand side of the figure. This bar shows the current polarization extinction ratio (PER) of the light coming from the fiber in dB. Here, it shows a rather low PER of about 20.

Figure C.1b shows the main window of the polarimeter software after a quarter-wave plate and a half-wave plate have been introduced in front of the input fiber end and aligned to maximize the PER of the fiber output beam. This was greatly eased by the extinction ratio mode of the polarimeter software, because it allows the use of the wave plates in front of the fiber to adjust the output polarization state to the center of the circle indicated on the Poincaré sphere. If the output polarization vector assumes this value, the influence of external disturbances such as temperature changes and pressure applied to the fiber should be minimal. This was confirmed by re-running the extinction ratio measurement procedure. This time, the circle on the Poincaré sphere has a much smaller diameter, which is almost as small as the noise of the individual polarization measurements.



(a) before alignment of input polarization      (b) after alignment of input polarization

Figure C.1.: Polarization measurements of optical fibers.



## C.2. Contamination and damage of the fiber interfaces

When dealing with optical fibers, and especially reflections off their ends, it is very instructive to take a detailed look at them through a fiber microscope. While one would naïvely assume to see something very similar to the illustrations usually seen in fiber context, in fact the results may look vastly different, as shown in Figure C.2a, which shows a magnified view of a typical fiber end after years of use in the lab (and probably very little cleaning).

For comparison, the same fiber end is shown in Figure C.2b. It was also found that the amount of dirt on the interface can have a significant impact on the observed reflectivity. In light of this discovery, all fibers involved in the experiment were thoroughly checked and cleaned. However, the influence on the amplitude of the ghost beams in the setup was negligible, as it was still orders of magnitude too high to be compatible with the mission requirement.

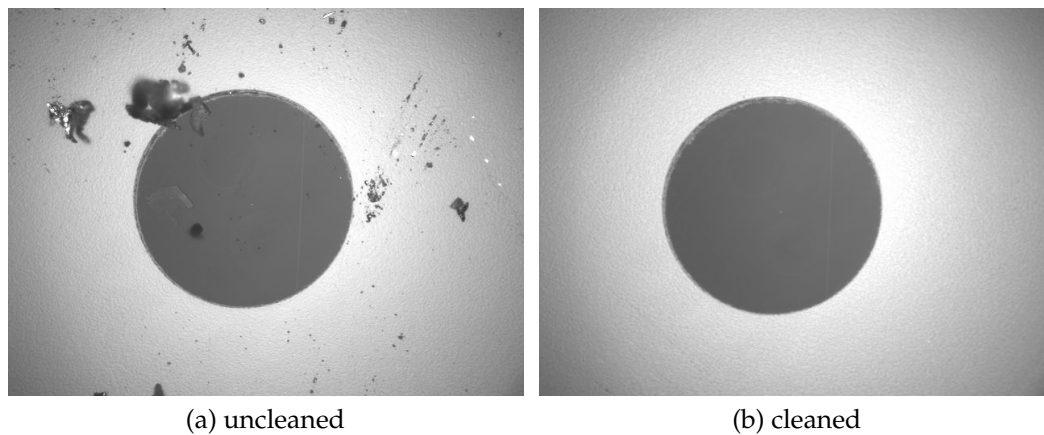


Figure C.2.: Magnified view of a fiber interface

An even worse fiber end was found at the fiber carrying the light from the iodine stabilized laser. The photograph in Figure C.3a shows a ring around the fiber's core where material is chipped. It is assumed that this occurred due to the high power that this fiber carries. The light power at the fiber input is about 1 W, with about 700 to 800 mW exiting from the end shown in the figure.

As was expected, cleaning this fiber end did not remove this circle around the core, which hardened the suspicion that material really had chipped off here due to the high power and the resulting thermal stress at and around the core. Comparing Figure C.3a to that found in [79], one can find striking similarities. The picture in [79] shows a fiber that was carrying high laser power and whose end face was contaminated. Therefore it can be concluded that a piece of dust must have been on the fiber end facet while high optical power was delivered, which led to the damage at the surface.

This illustrates the importance of proper fiber cleaning. The increased absorption from a contamination at the fiber end leads to high temperatures and results in damage of the fiber surface. This can even lead to a kind of chain reaction, because the damaged surface also has a higher absorption than an undamaged fiber end, leading to further damage, a phenomenon known as the fiber fuse effect [80, 81]. The threshold power density for this effect is approximately  $2 \text{ MW} / \text{cm}^2$ , so we were very lucky that this did not happen here and damage the fiber, as power density with approximately 1 W transmitted by the fiber and a core diameter of  $6 \mu\text{m}$  is about  $7 \text{ MW} / \text{cm}^2$ .

As cleaning was not effective, a different approach had to be taken to refurbish the surface. Polishing sheets and a special mount, which holds the fiber under an eight degree angle during polishing were used to re-polish this surface. Figures C.3b through C.3d show the fiber end after the application of  $3 \mu\text{m}$ ,  $1 \mu\text{m}$  and  $0.3 \mu\text{m}$  polishing, respectively. It can clearly be seen that the surface gets smoother in every step, yet even after the final step it is not as smooth as the end facet of a newly purchased fiber. This could be attributed to the limited experience the author had with polishing fibers or the inferior quality of the polishing sheets that came in a set for connectorizing optical fibers.

The results achieved using the polishing sheets are still satisfactory, especially when taking into account that without this method a costly repair at the fiber manufacturer's premises would have been the only option. The fiber is still in use in experiments and no further deterioration of the end facette has been observed so far.

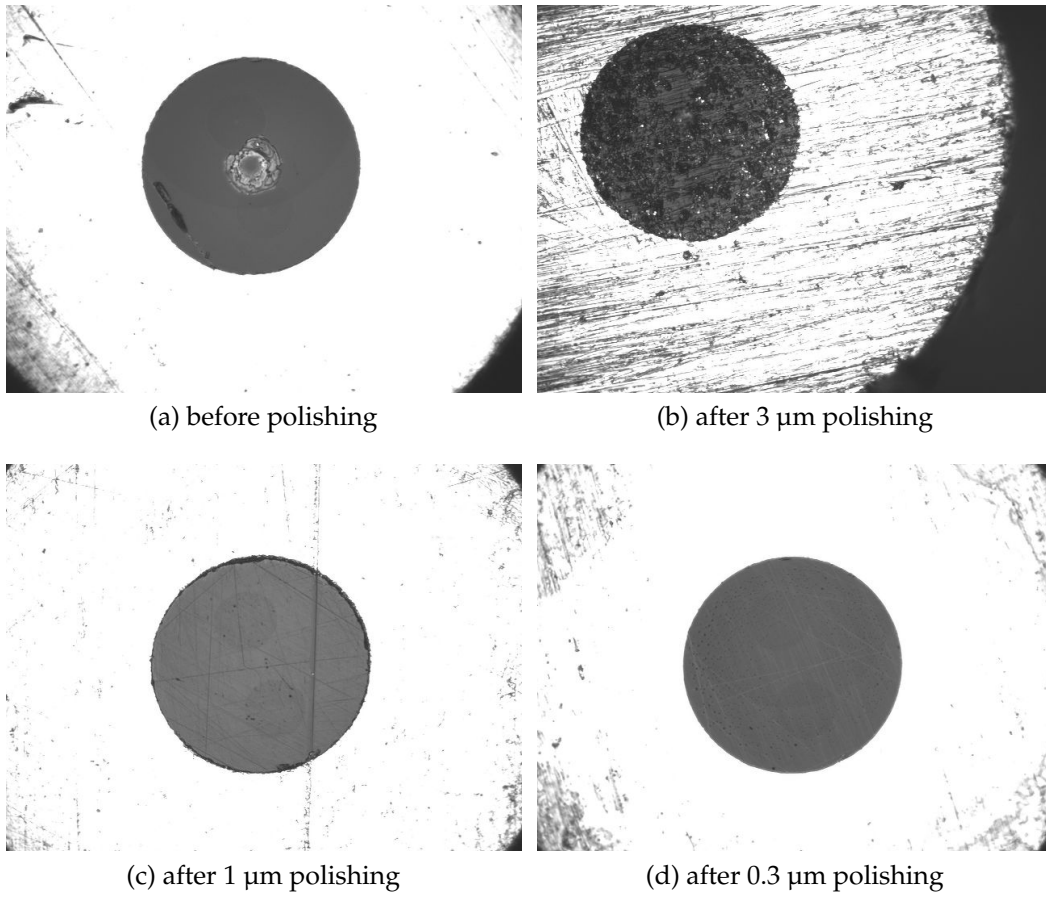


Figure C.3.: Magnified view of a damaged fiber interface.



---

## Bibliography

---

- [1] E.P. Hubble. *The nature of science, and other lectures*. Huntington Library publications. Huntington Library, 1954.
- [2] W. Heisenberg. *Der Teil und das Ganze*. Harper torchbooks. The Academy library. Harper & Row, 1971.
- [3] Zdeněk Knittl. The Principle of Reversibility and Thin Film Optics. *Optica Acta: International Journal of Optics*, 9(1):33–45, January 1962.
- [4] O. Jennrich. LISA technology and instrumentation. *Classical and Quantum Gravity*, 26:153001, 2009.
- [5] Oliver Jennrich, Pierre Binetruy, Monica Colpi, Karsten Danzmann, Phillippe Jetzer, Alberto Lobo, Gijs Nelemans, Bernard Schutz, Robin Stebbins, Tim Sumner, Stefano Vitale, and Henry Ward. *NGO Yellow Book*. 2011.
- [6] Steven P Hughes. Preliminary Optimal Orbit Design for the Laser Interferometer Space Antenna (LISA). In Robert D Culp and Steven D Jolly, editors, *Advances in Astronautical Sciences*, volume 111, page 61, 2005.
- [7] Li Guangyu, Yi Zhaohua, Gerhard Heinzl, Albrecht Rüdiger, Oliver Jennrich, Wang Li, Yan Xia, Zeng Fei, and Zhao Haibin. Methods for orbit optimization for the LISA gravitational wave observatory. *International Journal of Modern Physics D*, 17(7):1021–1042, 2008.
- [8] B Culshaw. The optical fibre Sagnac interferometer: an overview of its principles and applications. *Measurement Science and Technology*, 17(1):R1–R16, January 2006.
- [9] W K Burns, R P Moeller, C a Villarruel, and M Abebe. All-fiber gyroscope with polarization-holding fiber. *Optics letters*, 9(12):570–2, December 1984.

- [10] K Böhm, P Russer, E Weidel, and R Ulrich. Low-noise fiber-optic rotation sensing. *Optics letters*, 6(2):64–6, February 1981.
- [11] Georges Sagnac. Sur la preuve de la réalité de l'éther lumineux par l'expérience de l'interférographe tournant. *Comptes Rendus*, 157:1410–1413, 1913.
- [12] Georges Sagnac. L'éther lumineux démontré par l'effet du vent relatif d'éther dans un interféromètre en rotation uniforme. *Comptes Rendus*, 157:708–710, 1913.
- [13] R. Anderson, H.R. Bilger, and G.E. Stedman. "Sagnac" Effect: A century of Earth-rotated interferometers. *American Journal of Physics*, 62(11):975–985, 1994.
- [14] Michelle B. Larson. Constructing a portable sundial. *The Physics Teacher*, 37(2):113, 1999.
- [15] K. U. Schreiber, T. Klügel, a. Velikoseltsev, W. Schlüter, G. E. Stedman, and J.-P. R. Wells. The Large Ring Laser G for Continuous Earth Rotation Monitoring. *Pure and Applied Geophysics*, 166(8-9):1485–1498, May 2009.
- [16] R H Stolen and E H Turner. Faraday rotation in highly birefringent optical fibers. *Appl. Opt.*, 19(6):842–845, 1980.
- [17] K Bohnert, P Gabus, J Kostovic, and H Bri£;ndle. Optical fiber sensors for the electric power industry. *Optics and Lasers in Engineering*, 43(3-5):511–526, 2005.
- [18] R H West. Dispersion of Verdet constant in stress-birefringent silica fibre. *Electronics Letters*, 20(22):20–22, 1984.
- [19] P. N. Schatz and a. J. McCaffery. *The Faraday effect*, volume 23. 1969.
- [20] Asahi Kasei Corp. Asahi Kasei AK8973 data sheet. <http://pdf1.alldatasheet.com/datasheet-pdf/view/219477/AKM/AK8973.html>.
- [21] V. Courtillot and J.L. Le Mouel. Time variations of the earth's magnetic field-From daily to secular. *Annual Review of Earth and Planetary Sciences*, 16:389–476, 1988.
- [22] G W Day, M N Deeter, A H Rose, and K B Rochford. Faraday Effect Sensors for Magnetic Field and Electric Current. *SPIE Proceedings*, 2292:42–47, 1994.
- [23] J.W. W Fleming. Material dispersion in lightguide glasses. *Electronics Letters*, 14(11):326, 1978.
- [24] Dennis Weise. Technical Note 6 - OB Requirements Specification and Justification. Technical Report LOB-ASD-TN-006-02, Astrium GmbH, 2010.
- [25] H J Arditty and H. C. Leëfovre. Sagnac effect in fiber gyroscopes. *Optics Letters*, 6(8):401, August 1981.

- [26] H J Arditty and H C Lefèvre. Theoretical Basis of Sagnac Effect in Fiber-Optic Gyroscopes. In S Ezekiel and H J Arditty, editors, *Fiber-Optic Rotation Sensors and related Technologies*, pages 44–51. Springer Verlag New York, 1982.
- [27] Roland Fleddermann. Komponentencharakterisierung für LISA Rauscharme Spannungsreferenzen und Reziprozität einer Glasfaser. Diplomarbeit, Leibniz Universität Hannover, 2006.
- [28] Antonio F García Marín, G Heinzl, and K Danzmann. Interferometry for LISA and LISA Pathfinder. *Journal of Physics: Conference Series*, 66(Ere 2006):012052, May 2007.
- [29] P McNamara, S Vitale, K Danzmann, and on behalf of the LISA Pathfinder Science Working Team. LISA Pathfinder. *Classical and Quantum Gravity*, 25(11):114034, 2008.
- [30] Parameswaran Hariharan. *Optical Interferometry*. Academic Pr Inc, 2 edition, 2003.
- [31] G Heinzl, V Wand, O Jennrich, C Braxmaier, D Robertson, K Middleton, D Hoyland, R Schilling, U Johann, K Danzmann, A García, and A Rüdiger. The LTP interferometer and phasemeter. *Classical and Quantum Gravity*, 21(5):581–587, March 2004.
- [32] Vinzenz Wand, Felipe Guzmán, Gerhard Heinzl, and Karsten Danzmann. LISA Phasemeter development. *AIP Conf. Proc.*, 873(1):689–696, November 2006.
- [33] Iouri Bykov, Juan José Esteban Delgado, Antonio Francisco García Marín, Gerhard Heinzl, and Karsten Danzmann. LISA phasemeter development: Advanced prototyping. *Journal of Physics: Conference Series*, 154:012017, March 2009.
- [34] Frank Steier. *Interferometry techniques for spaceborne gravitational wave detectors*. Phd thesis, Gottfried Wilhelm Leibniz Universität Hannover, 2008.
- [35] F. Nix and D. MacNair. The Thermal Expansion of Pure Metals: Copper, Gold, Aluminum, Nickel, and Iron. *Physical Review*, 60(8):597–605, October 1941.
- [36] Sascha Skorupka. *Rauschuntersuchungen an hochstabilen Lasersystemen für die wissenschaftliche Weltraummission LISA*. Phd thesis, Gottfried Wilhelm Leibniz Universität Hannover, 2007.
- [37] M Tröbs, P Weiß els, C Fallnich, M Bode, I Freitag, S Skorupka, G Heinzl, and K Danzmann. Laser development for LISA. *Classical and Quantum Gravity*, 23(8):S151–S158, April 2006.

- [38] E J Elliffe, J Bogenstahl, A Deshpande, J Hough, C Killow, S Reid, D Robertson, S Rowan, H Ward, and G Cagnoli. Hydroxide-catalysis bonding for stable optical systems for space. *Classical and Quantum Gravity*, 22(10):S257–S267, May 2005.
- [39] M. Tröbs, J. Bogenstahl, M. Dehne, C. Diekmann, E. Granova, A. Shoda, G. Wanner, and G. Heinzel. Test of interferometry concept. Technical Report LOB-AEI-TN-005.1, April 2011.
- [40] J N Reddy. *Theory and analysis of elastic plates*. Series in Systems and Control Series. Taylor & Francis, 1999.
- [41] Zerodur data sheet. [http://www.schott.com/advanced\\_optics/english/download/schott\\_zerodur\\_zero\\_expansion\\_glass\\_ceramic\\_may\\_2011\\_en.pdf](http://www.schott.com/advanced_optics/english/download/schott_zerodur_zero_expansion_glass_ceramic_may_2011_en.pdf).
- [42] J Bogenstahl, L Cunningham, E D Fitzsimons, J Hough, C J Killow, M Perreur-Lloyd, D Robertson, S Rowan, and H Ward. LTP fibre injector qualification and status. *Journal of Physics: Conference Series*, 154:012011, March 2009.
- [43] Gerhard Heinzel. Ifocad: A framework of c subroutines to plan and optimize the geometry of laser interferometers. [http://gw.icrr.u-tokyo.ac.jp/gwadw2010/program/2010\\_GWADW\\_Heinzel.pdf](http://gw.icrr.u-tokyo.ac.jp/gwadw2010/program/2010_GWADW_Heinzel.pdf).
- [44] Roland Schilling. Optocad, a fortran 95 module for tracing gaussian beams through an optical set-up. <http://home.rzg.mpg.de/~ros/optocad.html>.
- [45] David K. Buck and Aaron A. Collins. POV-ray - the persistence of vision raytracer.
- [46] F Steier, R Fleddermann, J Bogenstahl, C Diekmann, G Heinzel, and K Danzmann. Construction of the LISA back-side fibre link interferometer prototype. *Classical and Quantum Gravity*, 26(17):175016, September 2009.
- [47] Felipe Guzmán Cervantes. *Gravitational Wave Observation from Space: optical measurement techniques for LISA and LISA Pathfinder*. PhD thesis, Leibniz Universität Hannover, 2009.
- [48] N F Ness. Observed Properties of the Interplanetary Plasma. *Annual Review of Astronomy and Astrophysics*, 6(1):79–114, September 1968.
- [49] V Wand, J Bogenstahl, C Braxmaier, K Danzmann, a García, F Guzmán, G Heinzel, J Hough, O Jennrich, C Killow, D Robertson, Z Sodnik, F Steier, and H Ward. Noise sources in the LTP heterodyne interferometer. *Classical and Quantum Gravity*, 23(8):S159, April 2006.



- [50] Y. Sasaki, T. Hosaka, K. Takada, and J. Noda. 8 km-long polarisation-maintaining fibre with highly stable polarisation state. *Electronics Letters*, 19(19):792, 1983.
- [51] Panda fiber data sheet. [http://www.fujikura.co.jp/eng/products/tele/o\\_device/data/16pnb04.pdf](http://www.fujikura.co.jp/eng/products/tele/o_device/data/16pnb04.pdf).
- [52] C C Cutler, S a Newton, and H J Shaw. Limitation of rotation sensing by scattering. *Optics letters*, 5(11):488–90, November 1980.
- [53] Yves Painchaud, Michel Poulin, Michel Morin, and Michel Têtu. Performance of balanced detection in a coherent receiver. *Optics express*, 17(5):3659–72, March 2009.
- [54] G. Heinzl. LISO: Linear Simulation and optimisation of analog circuits. see Appendix C of [82].
- [55] Euan Morrison, Brian J Meers, David I Robertson, and Henry Ward. Experimental demonstration of an automatic alignment system for optical interferometers. *Appl. Opt.*, 33(22):5037–5040, August 1994.
- [56] OWIS. OWIS Website. <http://www.owis-staufen.de/php/web8/animation/26.204.2502.zip>.
- [57] Jan Rybizki. Lisa back-link fibre: back reflection of a polarization maintaining single-mode optical fibre. Diplomarbeit, Leibniz Universität Hannover, 2011.
- [58] T. Miya, Y. Terunuma, T. Hosaka, and T. Miyashita. Ultimate low-loss single-mode fibre at 1.55  $\mu\text{m}$ . *Electronics Letters*, 15(4):106, 1979.
- [59] Daniel a Shaddock. Digitally enhanced heterodyne interferometry. *Optics letters*, 32(22):3355–7, November 2007.
- [60] Glenn de Vine, David S Rabeling, Bram J J Slagmolen, Timothy T-Y Lam, Sheon Chua, Danielle M Wuchenich, David E McClelland, and Daniel a Shaddock. Picometer level displacement metrology with digitally enhanced heterodyne interferometry. *Optics express*, 17(2):828–37, January 2009.
- [61] Massimo Tinto, Michele Vallisneri, and J. Armstrong. Time-delay interferometric ranging for space-borne gravitational-wave detectors. *Physical Review D*, 71(4):1–5, February 2005.
- [62] G Heinzl, C Braxmaier, K Danzmann, P Gath, J Hough, O Jennrich, U Johann, A Rüdiger, M Sallusti, and H Schulte. LISA interferometry: recent developments. *Class. Quantum Grav.*, 23(8):119–124, 2006.

- [63] Juan José Esteban, Iouri Bykov, Antonio Francisco García Marín, Gerhard Heinzl, and Karsten Danzmann. Optical ranging and data transfer development for LISA. *Journal of Physics: Conference Series*, 154:012025, March 2009.
- [64] S. Barke, M. Tröbs, B. Sheard, G. Heinzl, and K. Danzmann. EOM sideband phase characteristics for the spaceborne gravitational wave detector LISA. *Applied Physics B*, 98(1):33–39, August 2009.
- [65] Simon Barke, Michael Tröbs, Benjamin Sheard, Gerhard Heinzl, and Karsten Danzmann. Phase noise contribution of EOMs and HF cables. *Journal of Physics: Conference Series*, 154:012006, March 2009.
- [66] Danielle M R Wuchenich, Timothy T-Y Lam, Jong H Chow, David E McClelland, and Daniel a Shaddock. Laser frequency noise immunity in multiplexed displacement sensing. *Optics letters*, 36(5):672–4, March 2011.
- [67] Gerhard Heinzl, V. Wand, Antonio Garcia, Felipe Guzman, Frank Steier, Christian J. Killow, D. Robertson, H. Ward, and C. Braxmaier. Investigation of noise sources in the LTP interferometer. <http://edoc.mpg.de/display.ep1?mode=doc&id=395069>.
- [68] Christian Diekmann, Frank Steier, Benjamin Sheard, Gerhard Heinzl, and Karsten Danzmann. Analog phase lock between two lasers at LISA power levels. *Journal of Physics: Conference Series*, 154:012020, March 2009.
- [69] Yufeng Li. Cladding-mode assisted fiber-to-fiber and fiber-to-free-space coupling. *Optics Communications*, 183(5-6):377–388, September 2000.
- [70] O V Ivanov, S A Nikitov, and Yu V Gulyaev. Cladding modes of optical fibers : properties and applications. *Physics-Uspekhi*, 49(2):167–191, 2006.
- [71] Guangyu Li, Zhaohua Yi, Gerhard Heinzl, Albrecht Rüdiger, Oliver Jennrich, Li Wang, Yan Xia, Fei Zeng, and Haibin Zhao. Methods for Orbit Optimization for the LISA gravitational wave observatory. *International Journal of Modern Physics D*, 17(7):1021, 2008.
- [72] Maren Böse and Thomas H. Heaton. Probabilistic prediction of rupture length, slip and seismic ground motions for an ongoing rupture: implications for early warning for large earthquakes. *Geophysical Journal International*, 183(2):1014–1030, November 2010.
- [73] Gérardine Meishan Goh. Pella vilya: Near earth objects -Planetary defence through the regulation of resource utilisation. *Acta Astronautica*, 67(1-2):230–240, July 2010.

- [74] Walter Peeters. Forecasting the consequences of the “Crash of 2008” on space activities. In Kai-Uwe Schrogl, Wolfgang Rathgeber, Blandina Baranes, and Christophe Venet, editors, *Yearbook on Space Policy 2008/2009*, Yearbook on Space Policy, pages 164–178. Springer Vienna, 2010.
- [75] Robert Smith. Faux review. A report on the zombie outbreak of 2009: how mathematics can save us (no, really). *Canadian Medical Association journal*, 181(12):E297–300, December 2009.
- [76] Jean Michel Tchenche and C Chiyaka, editors. *Infectious Disease Modelling Research Progress*. Public Health in the 21st Century. Nova Science Publishers, Inc., 2010.
- [77] Eric Udd. Sensing and instrumentation applications of the Sagnac fiber optic interferometer. *Proceedings of SPIE*, 2341(Xc):52–59, 1994.
- [78] Brian Culshaw and IP Giles. Frequency modulated heterodyne optical fiber Sagnac interferometer. *IEEE Journal of Quantum Electronics*, 18(4):690–693, 1982.
- [79] Koji Seo, Naoya Nishimura, Masato Shiino, R. Yuguchi, and H. Sasaki. Evaluation of high-power endurance in optical fiber links. *Furukawa Review*, 24(24):18–22, 2003.
- [80] T J Driscoll, J M Calo, and N M Lawandy. Explaining the optical fuse. *Optics letters*, 16(13):1046–8, July 1991.
- [81] R M Atkins, P G Simpkins, and a D Yablon. Track of a fiber fuse: a Rayleigh instability in optical waveguides. *Optics letters*, 28(12):974–6, June 2003.
- [82] G. Heinzl. *Advanced optical techniques for laser-interferometric gravitational-wave detectors*. PhD thesis, University of Hannover, 1999.



---

## Acknowledgments

---

First and foremost I would like to thank Prof. Karsten Danzmann for giving me the opportunity to work in such a pleasant environment with excellent technical infrastructure and surrounded by competent and friendly co-workers.

Many of the things I learned during my work at AEI I learned from Gerhard Heinzl, who was always there to help with discussions and useful hints when things did not go as expected or to suggest new methods of dealing with problems encountered in the experiment. Thank you very much for this Gerhard!

I also want to thank all people of the LISA group. Thanks especially go to Christian Diekmann, Jan Rybizki, Frank Steier, and Michael Tröbs who worked on the experiments with me. The discussions, especially with Michael Tröbs and Frank Steier on the experiment but also on other work related issues taught me a lot and were also very enjoyable. Thanks also to all other LISA group members and colleagues at the AEI for the wonderful time we had together.

Special thanks go to Danielle Wuchenich, who made it possible to use Digitally enhanced Interferometry in the experiments by providing her measurement equipment as well as her expert knowledge.

Gerhard, Aiko, Christian, Michael, Paul and Marina proof-read this thesis. They all spent a lot of time and effort on this, and I am sure it improved the quality of this thesis a lot. Thank you for your valuable annotations and for providing them on such short notice!

Thank you to my family, who has always supported and loved me. And finally, I thank my wonderful wife Kerstin for giving me support and encouragement when I needed it and for her love.



## Personal details

Roland Fleddermann  
Stockmannstr. 14  
30451 Hannover  
  
Tel.: (0511) 2 61 53 65  
email: Roland.Fleddermann@gmx.de  
  
Date of Birth: March 17, 1981  
married, no children

## Education

06/87–06/91      Primary school Varl  
06/91–06/00      Söderblom Gymnasium Espelkamp  
specialised courses: maths and physics  
degree: Abitur

## University Education

10/01–11/06      Physics at University of Hannover  
12/06              Diplom degree in Physics  
11/05–10/06      Diploma Thesis: "Komponentencharakterisierung für LISA –  
Rauscharme Spannungsreferenzen und Reziprozität einer Glas-  
faser" (english translation: "Component characterization for  
LISA – Low noise voltage references and reciprocity of an  
optical fiber").  
01/07–now        PhD Student at AEI Hanover, main work: reciprocity of optical  
fibers, picometre sensitive interferometry

**Languages**      German, English





- [1] Gerhard Heinzl, Frank Steier, Roland Fleddermann, Benjamin Sheard and Karsten Danzmann. Components for the LISA local interferometry. *American Inst. of Physics*, 2006.
- [2] Roland Fleddermann, Frank Steier, Michael Tröbs, Gerhard Heinzl and Karsten Danzmann. Intrinsic noise and temperature coefficients of selected voltage references. *IEEE Trans. Instrum. Meas.*, 57, Dec 2008.
- [3] Roland Fleddermann, Frank Steier, Michael Tröbs, Johanna Bogenstahl, Christian Killow, Gerhard Heinzl and Karsten Danzmann. Measurement of the non-reciprocal phase noise of a polarization maintaining single-mode optical fiber. *Journal of Physics: Conference Series*, 154:012022 (6pp), 2009.
- [4] F Steier, R Fleddermann, J Bogenstahl, C Diekmann, G Heinzl and K Danzmann. Construction of the LISA back-side fibre link interferometer prototype. *Classical and Quantum Gravity*, 26(17):175016 (7pp), 2009.
- [5] Roland Fleddermann, Christian Diekmann, Frank Steier, Michael Tröbs, Gerhard Heinzl and Karsten Danzmann. Successful demonstration of stray light subtraction in data post-processing for the LISA backlink fiber non-reciprocity experiment. Submitted for publication in *Journal of Physics: Conference Series*, Expected online publication: Fourth quarter 2011.



---

## Selbstständigkeitserklärung

---

Ich versichere, dass diese Arbeit ausschließlich unter der Zuhilfenahme der angegebenen Quellen und Hilfsmittel angefertigt wurde und dass sie nicht schon als Masterarbeit, Diplomarbeit oder ähnliche Prüfungsarbeit verwendet worden ist.

(Roland Fleddermann) Hannover, den 2. Dezember 2011.